Investigation of structural and magnetic properties of first and second row transition metals with N,N',N and S,N,S pincer-type ligands

Sarah Ouanounou

Thesis submitted to the Faculty of Graduate and Postdoctoral Studies
In partial fulfillment of the requirements for the
M.Sc. degree in Chemistry

Supervisor: Professor Darrin S. Richeson

Abstract

This work began with the ambition of probing the application of pincer ligands to control the geometry and bonding environments of metal centers by employing the bis(imino) pyridine ligand scaffold and an assortment of transition metals, particularly silver and a variety of paramagnetic centers. The work was further extended to the investigation of the SNS tridentate thiolate ligand backbone, specifically the bis(methylthiomethyl) pyridine and bis(ethylthiomethyl) pyridine ligand frameworks with a similary array of transition metal centres. Along with the reports of novel coordination compounds and analysis of trends in bonding, computational chemistry was utilized to correlate the data obtained experimentally with computed models. Synthesis, characterization and computational studies are presented herein.

Chapter 1 presents a brief history of the bis(imino) pyridine ligand as well as its synthesis and characterization.

Chapter 2 presents a brief history of the S,N,S ligand as well as its synthesis and characterization.

Chapter 3 presents the synthesis of a series of first row transition metal bromide-bis(imino) pyridine complexes along with their characterizations and an analysis of bonding trends.

Chapter 4 presents the synthesis of a series of first row transition metal bromide-S,N,S ligand complexes along with their characterizations and an analysis of bonding trends.

Chapter 5 presents a general conclusion to the work.

Table of Contents

List of Figures

List of Tables

List of structures

Structure number	**Identification**
1	2,6-dibenzoylpyridine
1A	2,6-Bis{1-[(2,5-ditertbutylphenyl)imino]-benzyl}pyridine
1B	2,6-Bis{1-[(2,6-diisopropylphenyl)imino]-benzyl}pyridine
2A	$MnBr_2$-2,6-Bis{1-[(2,5-ditertbutylphenyl)imino]-benzyl}pyridine
2B	$FeBr_2$-2,6-Bis{1-[(2,5-ditertbutylphenyl)imino]-benzyl}pyridine
2C	$CoBr_2$-2,6-Bis{1-[(2,5-ditertbutylphenyl)imino]-benzyl}pyridine
2D	$NiBr_2$-2,6-Bis{1-[(2,5-ditertbutylphenyl)imino]-benzyl}pyridine
2E	$CuBr_2$-2,6-Bis{1-[(2,5-ditertbutylphenyl)imino]-benzyl}pyridine
2F	$ZnBr_2$-2,6-Bis{1-[(2,5-ditertbutylphenyl)imino]-benzyl}pyridine
3A/SNS1	2,6-bis(methylthiomethyl)pyridine
2B/SNS2	2,6-bis(ethylthiomethyl)pyridine
4a	$MnBr_2$- 2,6-bis(methylthiomethyl) pyridine
4A	$FeBr_2$- 2,6-bis(methylthiomethyl)pyridine
4b	$NiBr_{2-}$ 2,6-bis(methylthiomethyl)pyridine
4B	$CoBr_2$- 2,6-bis(methylthiomethyl)pyridine
4C	$CuBr_2$ – 2,6-bis(methylthiomethyl)pyridine
4D	ZnBr2 – 2,6-bis(methylthiomethyl)pyridine
4E	CoBr2- 2,6-bis(ethylthiomethyl)pyridine
4F	$CuBr_2$ – 2,6-bis(ethylthiomethyl)pyridine

Acknowledgements

First and foremost, I would like to thank my parents for affording me the opportunity to pursue my education and for their constant support as well as my family and sister Miriam for always being there for me. Also, I would like to thank Professor Darrin Richeson for allowing me the opportunity to work in his lab as well as for his guidance and support. Furthermore, I could not have completed any of this work without the help of the other members of the Richeson group– Titel Jurca, Sheila Michel, Nastaran Ghorbanian, and Ahmed Farghal. Lastly, thank you to the chemistry department at the University of Ottawa, Professor Serge Gorelsky for his help with the computations and Dr. Ilia Korobkov for his work with the SC-XRD.

Chapter 1: The N,N'N ligand: 2,6-bis{1-(2,5-ditertbutylphenyl)imino-benzyl}pyridine

[1.1] Introduction

A ligand can be either a neutral atom or an ion that bonds to a metal atom or ion. These ligands can be anions, cations or neutral and act as either Lewis acids, which accept electrons, or Lewis bases, which donate electrons.[1] Ligands must have at least one atom with a pair of donor electrons. These electrons are used to form covalent bonds with the metal. Classically, the metal center is considered the Lewis acid which forms an adduct with the lone pairs on the Lewis basic ligand. In the adduct formation, a pair of electrons are donated to the metal for each ligand donor atom.

There exist various specialized types of ligands, including chiral ligands, hemilabile ligands, etc. One of these specialized types of ligands are non-innocent ligands. These ligands are particular in that when coordinated to a metal, there is charge transfer to the point that the oxidation state on the metal is no longer clear.[2] For instance, a typically non-innocent ligand is NO. When coordinated to Fe, it is unclear whether the oxidation state of the Fe is unclear due to the non-innocence of the ligand.[3]

In inorganic chemistry, the ligand can be carefully designed and tuned in order to easily predict the various properties of the metal, ranging from physical to electrochemical or magnetic properties. By studying the coordination of a specific ligand with various transition metals, one can begin to predict the behavior of complexes containing these ligands and various transition metals. This allows one to design specific complexes with the desired properties.

---

[1] R.H. Crabtree, *The Organometallic Chemistry of the Transition Metals*, Fourth Edition, Wiley-Interscience, A John Wiley & Sons in. Publication, USA, **2005**, 2.

[2] G.L. Miessler, P.J. Fischer, D.A. Tarr, *Inorganic Chemistry*, Fifth Edition, Prentice Hall, USA, **2013**, 696.

[3] W. Kaim, B. Schwederski, *Coor. Chem. Rev.*, **2010**, *254* (14), 1580-1588.

In relation to the work discussed herein, the goal is to investigate whether the specific N,N',N and S,N,S ligand scaffolds employed could support novel electronic and/or magnetic properties with first-row transition metals; specifically transition metal bromides, with the goal of elucidating some trends in the structure, bonding, magnetic and electronic properties of the ligands and correlating these properties with computational models. The N,N,N ligand is discussed in the following sections while the S,N,S ligand is outlined in Chapter 3.

[1.2] The ligand: 2,6-bis{1-(2,5-ditertbutylphenyl)imino-benzyl}pyridine:

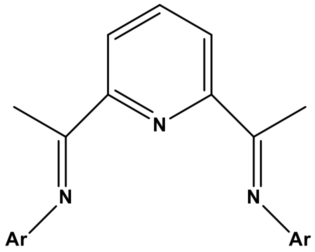

Figure 1.1: The general structure of the Diiminepyridine ligand system (DIMPY)

The diiminopyridine ligand system is depicted in Figure 1.1 and is commonly referred to as DIMPY. In the simplest and most common form, the imino carbon center bears a methyl group. The aryl group can vary. These are the two positions within the scaffold through which one can affect sterics and electronics. When coordinated to the metal center, the ligand represents a π-conjugated planar Lewis basic pincer ligand that is able to donate six electrons through the lone pairs on the nitrogen atoms.

The DIMPY ligand system was popularized by Brookhart[4] and Gibson[5] in the mid 1990's as it was found to support late transition metals, Fe and Co, as Ziegler-Natta polymerization catalysts, as exhibited in Figure 1.2.

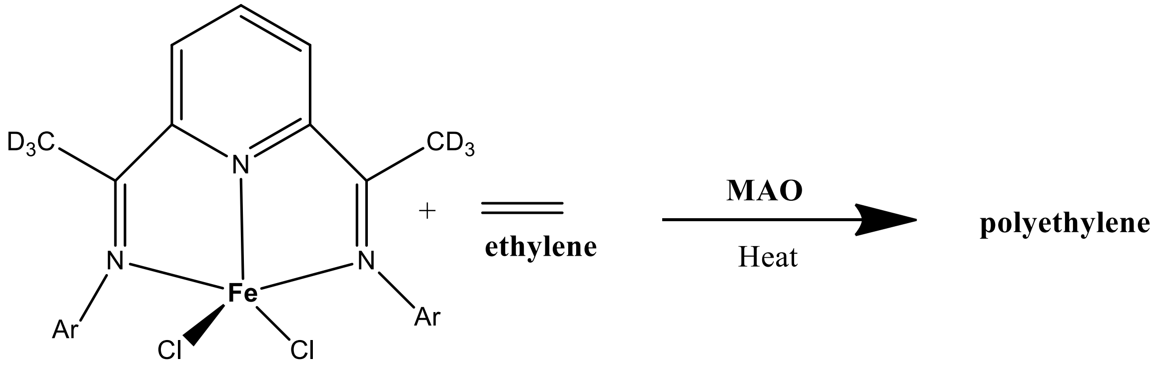

Figure 1.2: Brookhart's polymerization of ethylene using a DIMPY-Fe complex.[6]

[1.3] Ligand non-innocence

To date, the majority of research involving this particular ligand system has focused on coordination of transition metals. Although there are 3 donor sites at the nitrogen atoms in the ligand scaffold, the scope of the coordination is significantly more complex. One of the most unique features of this ligand scaffold is its ability to both accept and donate negative charge. The non-innocent nature of this ligand is also evidenced by the fact that the methyl groups on the imino carbons can be rather easily deprotonated. This is attributed to the extended π-system going from imine to imine via the pyridine ring. As a result, the ligand scaffold is considered non-innocent and is capable of participating in reactions. This feature has been reported by

---

[4] B.L. Small, M. Brookhart, A.M.A. Bennett, *J. Am. Chem. Soc.*, **1998**, 120, 4049.

[5] G.J.P. Britovsek, V.C. Gibson, B.S. Kimberley, P.J. Maddox, S.J. McTavish, G.A. Solan, A.J.P. White, D.J. Williams, *Chem. Commun*., **1998**, 849.

[6] B.L. Small, M. Brookhart, *J. Am. Chem. Soc*. **1998**, 120, 4049.

Gambarotta and Gibson with metals Li, Mg and Zn.[7,8] Figure 1.3 exhibits two reaction schemes from this research in which the olefin scaffold adopts different electronic distribution, thus showing its ability to accept varying amounts of electron density from its donors.

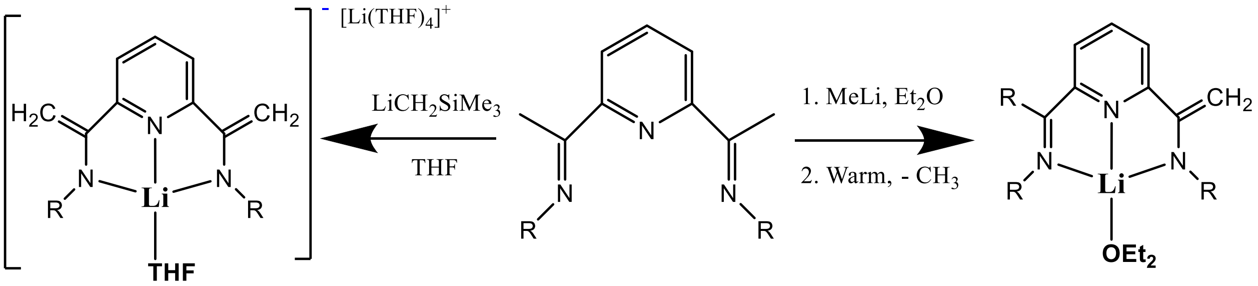

Figure 1.3: Reactions exhibiting the ligand's ability to accept and donate electron density and undergo proton transfer.

Furthermore, much like the non-innocent ligand NO seen earlier, the DIMPY ligand can act as both a σ-donor and a π-acceptor. Conversely, the DIMPY ligands exhibit single electron transfer from metal to ligand. This unique feature allows the ligand to stabilize metals in a large range of oxidation states.[9]

With all of these features in mind, we chose to explore the ligand framework exhibited in Figure 1.4. These particular ligand scaffolds were chosen in order to avoid the proton transfer pathway seen earlier by replacing the methyl substituents with the phenyl moieties. In addition, a bulky aryl group was employed in order to increase the steric congestion around the metal center and encourage low coordination numbers. The implementation of this steric bulk provides

---

[7] J. Scott, S. Gambarotta, I. Korobkov, Q. Knijnenburg, B. De Bruin, P.H.M. Budzelaar, *J. Am. Chem. Soc.*, 2005, 127, 17204.

[8] Q. Knijnenburg, S. Gambarotta, P.H.M. Budzelaar, *Dalton Trans*. **2006**, 5442.

[9] T. Jurca, K. Dawson, I. Mallov, T. Burchell, G.P.A. Yap, D.S. Richeson, *Dalton Trans*., **2010**, 39, 1266.

kinetic stabilization that could allow for the potential isolation of reaction transition metal centers.

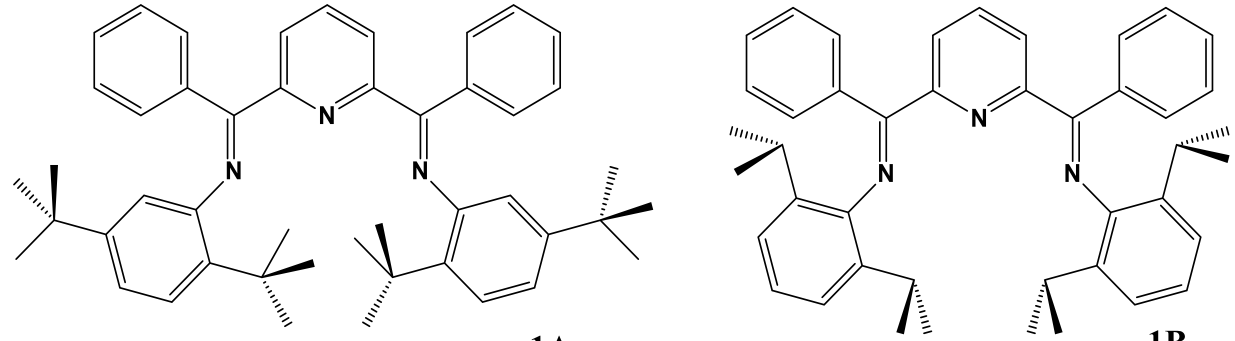

1A

1B

Figure 1.4: General structures of the two DIMPY ligands, **1A** and **1B**.

[1.4] Ligand synthesis and properties

As mentioned earlier, in order to avoid the decomposition pathway, the imine backbone was functionalized with phenyl groups. As outlined in the reported procedure and exhibited in Figure 1.5, the 2,6-dibenzoylpyridine precursor is generated using a Friedel-Crafts acylation of 2,6-dicarbonylpyridinedichloride.[10] Following this, there are two pathways to generate DIMPY ligands with phenyl backbones; however, we chose to avoid one of them in order to eliminate side products, namely trace $NiCl_2$. Our pathways was based on that reported by Kleigrewe et al.[11] in which analine is refluxed with a p-toluenesulfonic acid catalyst in toluene at 160°C for 48 hours. A Dean-Stark trap was used to remove H_2O and push the reaction towards completion. This lengthy process allows for high yield and purity.

---

[10] M.A. Esteruelas, A.M. Lopez, L. Mendez, M. Olivan, E. Onate, *Organometallics*, **2003**, 22, 395.

[11] N. Kleigrewe, W. Steffen, T. Blomker, G. Kehr, R. Frohlich, B. Wibbeling, G. Erker, J.C. Wasilke, G. Wu, G.C. Bazan, *J. Am. Chem. Soc.* **2005**, 127, 40, 13955.

Using this methodology, the two different DIMPY ligand precursors were synthesized. Following this procedure, a mixture of 2,6-dibenzoylpyridine, at least 2.1 equivalents of aniline and catalytic *p*-toluenesulfonic acid was refluxed in toluene at 160^{o}C for 48 hours under a light flow of N_2 to prevent evaporation and a Dean-Stark trap. After this, the solution was concentrated under vacuum to yield a thick brown paste which was then re-dissolved in cold methanol and held in the fridge overnight to form bright yellow precipitate. The resulting precipitate was washed with cold methanol to remove excess aniline and dried to yield pure ligand.

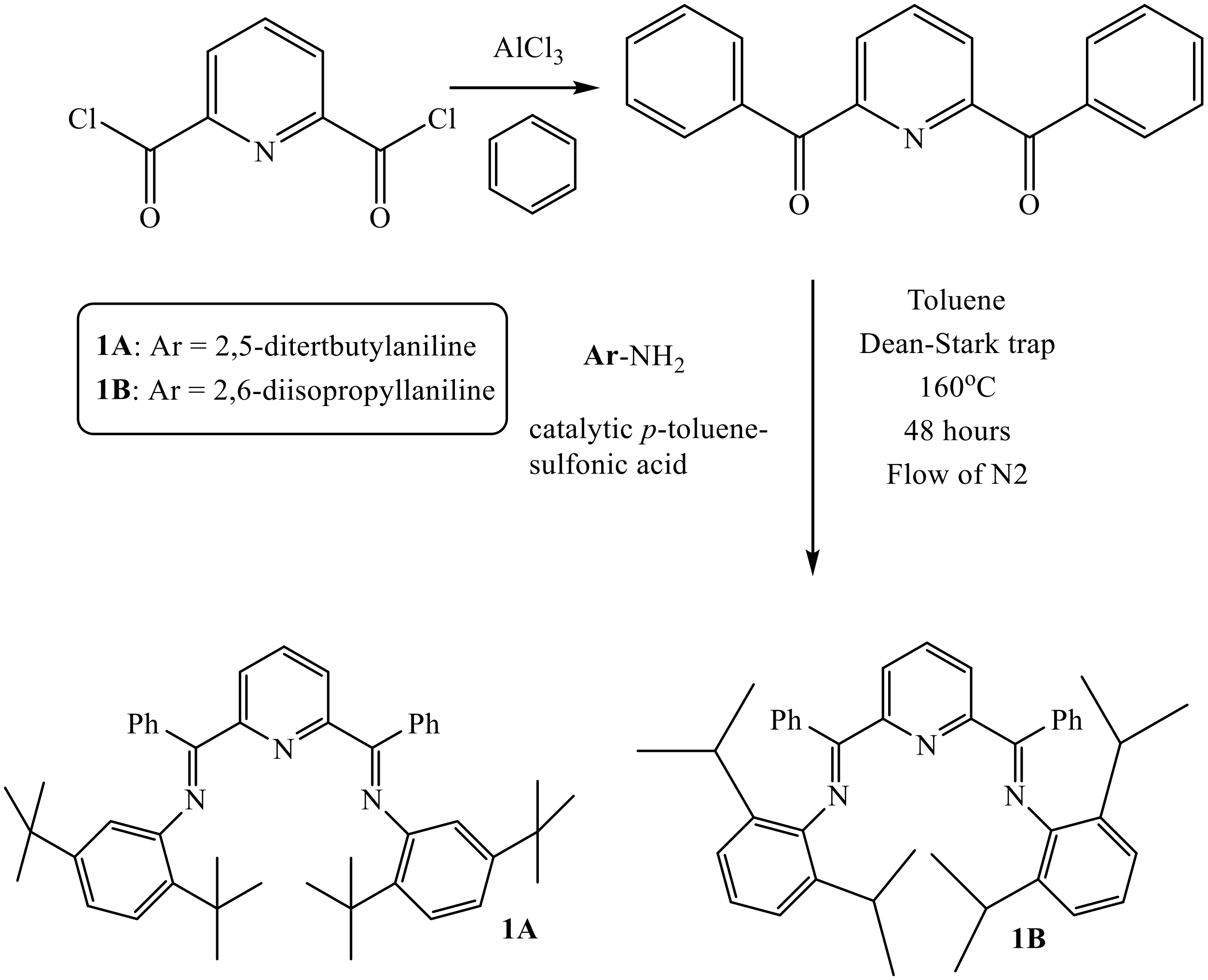

Figure 1.5: Synthesis of DIMPY ligands **1A** and **1B**.

The anilines employed in the reaction were 2,5-ditertbutylaniline and 2,6-diisopropylaniline. As can be seen, the 2,5-ditertbutylaniline substituted ligand scaffold has a higher degree of steric bulk, whereas the 2,6-diisopropylaniline-substituted backbone is less congested.

Characterization of the two ligand variants was performed with ^{1}H and ^{13}C NMR and confirmed by elemental analysis. However, at room temperature, several rotational isomers are observed due to rotation from the pyridine-2,6-carbon to imine-carbon bond as well as the imine-nitrogen to 2-aryl-carbon bond. This causes the NMR spectra to be extensively confusing when one takes into account the array of potential conformers. Although the NMR spectra for the free ligand are confusing, once coordinated to a metal center, the N,N,N' plane of the ligand adopts a nearly planar conformation. This results in a vastly more simplified spectrum.

[1.5] DIMPY ligand field strength

The spectrochemical series dictates whether a ligand will produce large or small field splitting resulting in either high spin or low spin metal complexes. The series, shown in Figure 1.6, orders ligands on the basis of their field strength or ability to split d-orbital energy levels.[12] The ligands at the beginning of the series, such as I, produce weak splitting and are thus weak field ligands. The ligands towards the end of the series such as CN^{-} will produce strong splitting and are thus strong field ligands. Strong field splitting results in a large energy gap and low spin

---

[12] S.S. Zumdahl, *Chemical Principles*, Fifth Edition, Houghton Miflin Company, USA, **2005**, 550-551.

metal complexes, while weak field splitting results in a smaller energy gap and, consequently, high spin metal complexes.

$$\mathbf{I^- < Br^- < S^{2-} < SCN^- < Cl^- < NO_3^- < N_3^- < F^- < OH^- < C_2O_4^{2-} \approx H_2O <}$$

$$\mathbf{NCS^- < CH_3CN < py < NH_3 < en < bipy < phen < NO_2^- < PPh_3 < CN^- \approx}$$

Figure 1.6: The spectrochemical series

One could expect to find the DIMPY ligand at the end of the spectrum somewhere between en and phen. Consequently, one would expect the ligand scaffold to yield strong field splitting and yield low spin complexes; however, structural distortions induced by the scaffold have been shown experimentally in previous work by the Richeson group to yield small energy gaps.[13] This leads to complexes of DIMPY with transition metals to adopt high spin conformations.

[1.6] Magnetism

The investigation of the magnetic properties of these complexes if of particular interest due to the fact that, over the last few decades, the extensive commercial viability of magnetic materials have driven research in this area. Traditional magnetic materials are composed of arrays of inorganic atoms composed of transition metals or lanthanides that are produced at very high temperatures using metallurgy. Molecular magnets, on the other hand, are organic or inorganic/organic hybrids that are composed of either a spin-containing metal or a spin-

---

[13] T. Jurca, A. Farghal, P-H. Lin, I. Korobkov, M. Murugesu, D.S. Richeson, *J. Am. Chem. Soc*. **2011**, *133* (40), 15814-15817.

containing organic radical.[14] These systems have proven to have advantageous properties. For instance, their magnetic properties can be combined with mechanical and/or electric properties to yield novel electronic materials. Examples include current research into the use of single molecule magnets, a class of metalorganic compounds, in quantum computing. This type of research involves the design of materials with interesting bulk magnetic properties; however, in order to predict these properties, many general principles of magnetic behavior must be established; therefore, the investigation of these more simple complexes could be an interesting starting point for further work. The following sections will review the basics of the magnetic properties that will be analyzed in further chapters.

[1.6.1] Magnetic susceptibility[15]

When a molecular material is placed in an applied field, *H*, it acquires a magnetization, *M*. The relationship between these two parameters is defined as the magnetic susceptibility, χ, which is commonly in units of cm^3/mol. It refers to the degree of magnetization of the material in response to the applied magnetic field. The relationship is defined as,

$$\chi = \frac{\delta M}{\delta H}$$

The magnetic susceptibility of the material is related to temperature in an inversely proportional manner through a constant known as the Curie Constant, *C*.

$$\chi = \frac{C}{T}$$

---

[14] D. Gatteschi, R. Sessoli, J. Villain, *Molecular Magnets*, Oxford University Press, Inc., USA, **2006**, 12.

[15] R. Vincent, S. Klyatskaya, M. Ruben, W. Werndorfer; F. Balestro, *Nature*, **2012**, 488, 357-360

In order to obtain information regarding the type of magnetic interaction within a system, one frequently looks at the product of the magnetic susceptibility and temperature, χ T because the result is a constant.

[1.6.2] Diamagnetism and Paramagnetism[16]

On an atomic level, there exist two fundamental types of magnetism. These are diamagnetism and paramagnetism. With the exception of the hydrogen radical, all molecular materials exhibit diamagnetic behavior as they have more than one electron. Diamagnetic materials possess paired electrons. Diamagnetism arises from the interaction of paired electrons with an applied magnetic field. When these materials interact with a magnetic field, an opposing field is generated. This behavior is independent of temperature and its strength is roughly proportionate to the molecular weight of the material and the diamagnetic susceptibility χ^D, is essentially additive using the contribution from various atoms, ions and functional groups. These are called group contributions and are defined as Pascal's constants.

Paramagnetism, on the other hand, is characterized by the attraction of a substance to an applied magnetic field. This behavior arises from the interaction between unpaired electrons in atomic or molecular orbitals of a material and the applied field. Thus, these materials often contain one or more unpaired electrons. The overall magnetic susceptibility of a given material must take into account both the diamagnetic susceptibily, χ^D, and the paramagnetic susceptibility, χ^P.

$$\chi = \chi D + \chi P$$

---

[16] U. Mitzuni, *Introduction to the Electron Theory of Metals*, Cambridge University Press, UK, **2001**, 49.

The diamagnetic susceptibilities for various atoms, ions and functional groups have been calculated and documented; however for more current calculations, it is always assumed that experimentally determined susceptibilities are corrected for diamagnetic contributions.[17] This is largely due to the fact that the paramagnetic susceptibility is significantly greater than that of the diamagnetic susceptibility.

[1.6.3] The Curie Law[18]

The Curie law was developed in the early 1900s and describes the temperature dependence of an ideal paramagnet. It involves the molar susceptibility, χ_m, the magnitude of the magnetic spin, *S*, Avogadro’s Number, *N*, the spectroscopic splitting factor, *g*, the Bohr magneton, μ_B, and the Boltzman constant, *k*.

$$\chi m = \frac{Ng^2 \mu B^2}{3KT} S(S+1)$$

All of the values other than the temperature and the susceptibility are constants; therefore, the equation is usually reduced to include the Curie constant, *C*.

$$\chi m = \frac{C}{T}$$

When the Curie law is obeyed, the product of the molar susceptibility and temperature is a constant. Using these values, one can then calculate the effective magnetic moment, *Ueff*, which is a magnitude of the paramagnetism. It is defined as:

---

[17] G.A. Baine, J.F. Berry, *J. Chem. Ed*, **2008**, 85, 4.

[18] I. Morgenstern-Badarau, D. Cocco, A. Desideri, G. Rotilio, J. Jordanov, N. Dupre*, J. Am. Chem. Soc.*, **1998**, 108, 300.

$$Ueff = C\sqrt{T}\chi m$$

In this equation, when g is equal to 2, C has SI units $m^3mol^{-1}K$ and the equation can be rewritten as:

$$Ueff = 797.8\sqrt{T}\chi m$$

The quantity is effectively dimensionless but is often written in units of Bohr magneton.

The effective magnetic moment is related to another key value in magnetic materials, which is the number of unpaired electrons, *n*.

$$Ueff = \sqrt{n}(n + 2)$$

Experimentally, there exist ways in which one can measure one or more of these parameters, which can then be compared to the theoretical values. Therefore, in the synthesis of magnetic materials, these equations offer a means through which one can ensure that the synthesized complex has the desired magnetic properties. One way in which this can be done is through the use of NMR and Evan’s Method, which will be discussed and employed in Chapter 2.

Chapter 2: Complexes of 1st row transition metals bromides with the DIMPY ligand

[2.1] Introduction

DIMPY ligands have been shown to generate interesting chemistry when bound to a wide variety of metal ions. For instance, the discovery by Gibson, Brookart and Dupont that sterically bulky DIMPY complexes of Fe and CO exhibit high ethylene polymerization activity in the early 1990s. [19] Today, DIMPY chemistry has grown to cover a large portion of the periodic table with applications including but not limited to catalysis, optoelectronic devices and single molecule magnets.[20] Previous work by the Richeson group in collaboration with the Murugesu group involving this ligand scaffold has yielded very compelling results in terms of the synthesis of a mononuclear Co^{2+} based single molecule magnet supported by the DIMPY scaffold.[21]

Furthermore, these types of ligands have been shown to promote novel reactivity in first row transition metals. For instance, the iminopyridine scaffold has been shown to support spin-crossover with Fe(II). [22] First row transition metals are particularly interesting due to their predictable magnetic and electronic properties as well as their commercial and synthetic accessibility. As a result, it was of particular interest to investigate whether this ligand scaffold could support novel electronic and/or magnetic properties with first-row transition metals;

---

[19] (a)B.L. Small, M. Brookhart, *J. Am. Chem. Soc*., **1998**, 120, 7143. (b)B.L. Small, M. Brookhart, A.M.A. Bennett, *J. Am. Chem. Soc.,* **1998**, 120, 4049. (c)G.J.P. Britovsek, V.C. Gibson, B.S. Kimberley, P.J. Maddox, S.J. McTavish, G.A. Solan, A.J.P. White, D.J. Williams, *Chem. Commun*., **1998**, 849.

[20] (a)V.C. Gibson, C. Redshaw, G.A. Solan, *Chem. Rev*., **2007**, 107, 1745. (b) R. Fan, Y.Yang, Y. Yin, W. Hasi, Y. Mu, *Inorg. Chem*., **2009**, 48, 6034.

[21] T. Jurca, A. Farghal, P.H. Lin, I. Korobkov, M. Murugesu, D.S. Richeson, *J. Am. Chem. Soc*., **2011**, 133, 40, 15814.

[22] (a)M.A. Hoselton, L.J. Wilson, R.S. Drago, *J. Am. Chem. Soc.,* **1975**, 97, 1822-1729. (b) M. Seredyuk, A.B. Gaspar, V. Ksenofontov, Y. Galyametdinov, J. Kusz, P. Gutlich, *Adv. Funct. Mater*., **2008**, 18, 2089-2102. (c) A.C. Bowman, C. Milsmann, E. Bill, Z.R. Turner, E. Lublovsky, S. DeBeer, K. Wieghardt, P.J. Chirik, *J. Am. Chem. Soc.,* **2011**, 133, 17353-17369.

specifically transition metal bromides, with the goal of elucidating some trends in the structure, bonding, magnetic and electronic properties of the DIMPY ligand, as outlined in Chapter 1.

The specific first row transition metal bromides that were employed are outlined in the synthetic strategy in Figure 2.1. The DIMPY ligand was synthesized using the procedure outlined in section 2.5.

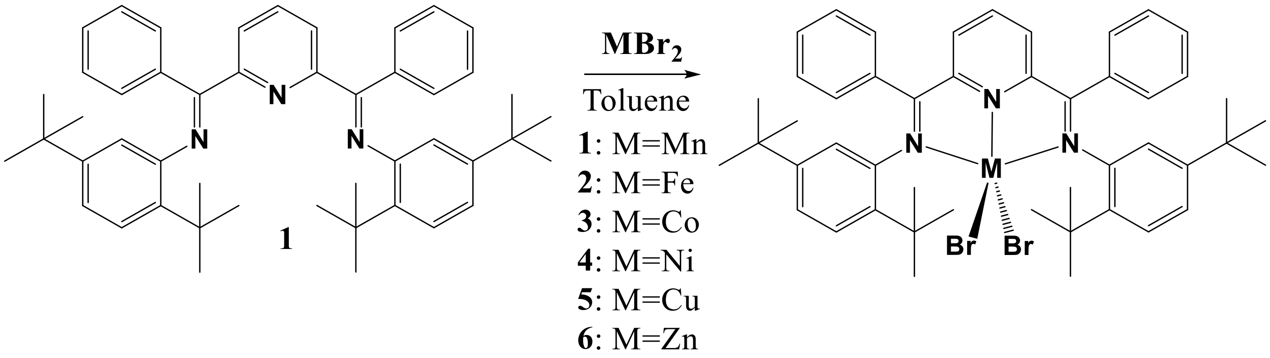

Figure 2.1: Schematic representation of reaction scheme.

Comprehensive trends in bonding for transition metal bromides with the DIMPY ligand scaffold have not been previously investigated; however, analogous work has been undertaken by the Shores group from Colorado State University utilizing the tripodal iminopyridine ligand framework.[23] Their results yielded information regarding structural and electronic comparison of 1st row transition metal complexes of a tripodal iminopyridine ligand. They were able to elucidate some trends; for instance, they determined that the complexes adopted a wide variety of geometries, from regular octahedral to trigonal antiprismatic; however, despite these variations in geometry, the complexes exhibited very similar absorption spectra. The properties

---

[23] A.M. McDaniel, A.K. Rappe, M.P. Shores, *Inorg. Chem.*, **2012**, 51 (22), 12493-12502.

of five coordinate first row transition metal centers with the imino pyridine-based ligand scaffolds, however, remain hitherto unexplored.

[2.1.2] Coordination number 5 and Valance Shell Electron Pair Repulsion (VSEPR) Theory[24]

VSEPR theory hypothesizes that the geometric arrangement of groups of atoms around a central atom is determined solely by the repulsions between the electron pairs which are located in the valence shell of the central atom. In other words, this is an electrostatic approach that causes the electron pairs around the central atom to arrange themselves in a way that minimizes repulsions. The geometry of a molecule depends on the number of pairs of electrons, which can be seen as bonding groups, and the number of nonbonding electrons on the atom. These bonding groups would ideally all be equally as far apart from each other as possible. Consequently, the ideal distribution of electron pairs would arrange themselves in the form of a polyhedron with all angles equivalent and all of the sides of the polygon as equal triangles. This arrangement of groups around a central atom can be adopted by all coordination numbers except 5. Hence, complexes with coordination number 5 are less prevalent. These complexes often lose a ligand to adopt a four coordinate geometry; however, 5 coordinate complexes do exist. In general, five coordinate complexes can adopt either trigonal bipyramidal, *tbp*, or square pyramidal, *sp*, geometries. The two geometries are outlined in Figure 2.2.

---

[24] (a) W.L. Jolly, *Modern Inorganic Chemistry*, First Edition, McGraw-Hill College Publications, USA, **1984**, 543. (b) R.J. Gillespie, J. Chem. Educ., 1970, 47, 18. (c) R.J. Gillespie, R.S. Nyholm, *Quart. Rev., **1957***, 11, 339.

Trigonal bipyramidal, *tbp* Square pyramidal, *sp*

Figure 2.2: Common geometries for complexes with coordination number 5. (Bas = basal, ax = axial, eq = equatorial)

In *tbp* complexes, there are two positions for the ligands, two axial, *ax*, and two equatorial, *eq*. These are shown in Figure 2.2. The positions of the ligands can change, i.e. the axial ligands can become equatorial ligands and vice versa; this is referred to a pseudorotation or Berry rotation.[25] Similarly, *sp* structures also have two distinct coordination sites, one axial, *ax*, and four basal, *bas*. The central atom can be either on the basal plane or slightly above it. The two geometries are only slightly different in energy and can easily interconvert; this is called fluxionality. [26]

In order to determine whether a complex with coordination number five's geometry is more like *tbp* or *sp*, a simple calculation can be employed. This calculation was developed in the early 1980s and allows one to approximate a five coordinate complex's geometry[27]; however, it is likely that there will be distortions from the ideal geometry. The calculation involved is that of a parameter called the τ parameter, τ, which employs the use of the largest ligand-metal ligand angle, α, and the smallest, β, of the complex:

Eq. 2.1

$$\tau = \frac{\alpha - \beta}{60}$$

---

[25] P. Russegger, J. Brickmann, *Chem. Phys. Lett.,* **1975**, 15(2), 276-278.
[26] T. Oka, E.T. White, *Science*, **1999**, 286, 1051.
[27] A. W. Addison, T. N. Rao, J. Reedijk, J. van Rijn, G. C. Verschoor, *J. Chem. Soc. Dalton Trans.,* **1984**, 1349.

An ideal *sp* would be associated with the angles α and β being equal, i.e. 180^o. This would yield a τ value of 0. On the other hand, for *tbp* complexes, α becomes 120^o and the largest angle, β, will be 180^o, thereby resulting in a τ value of 1.

[2.2] Results and discussion: Ligation of DIMPY to first row transition metal bromides

The synthesis of the transition metal bromide- DIMPY complexes proved to be fairly straight forward. The transition metal bromides were added to solutions of ligand in toluene and stirred overnight to provide optimal yields (an average of 87% yield) during which significant color changes were observed. The solutions were then held at -20^oC overnight to facilitate precipitation of the product. The solutions were then filtered and washed with hexanes to remove any impurities. The crystal structures obtained are outlined in Figure 2.3. The crystal data, bond lengths and bond angles are summarized in Tables 2.6 through 2.8.

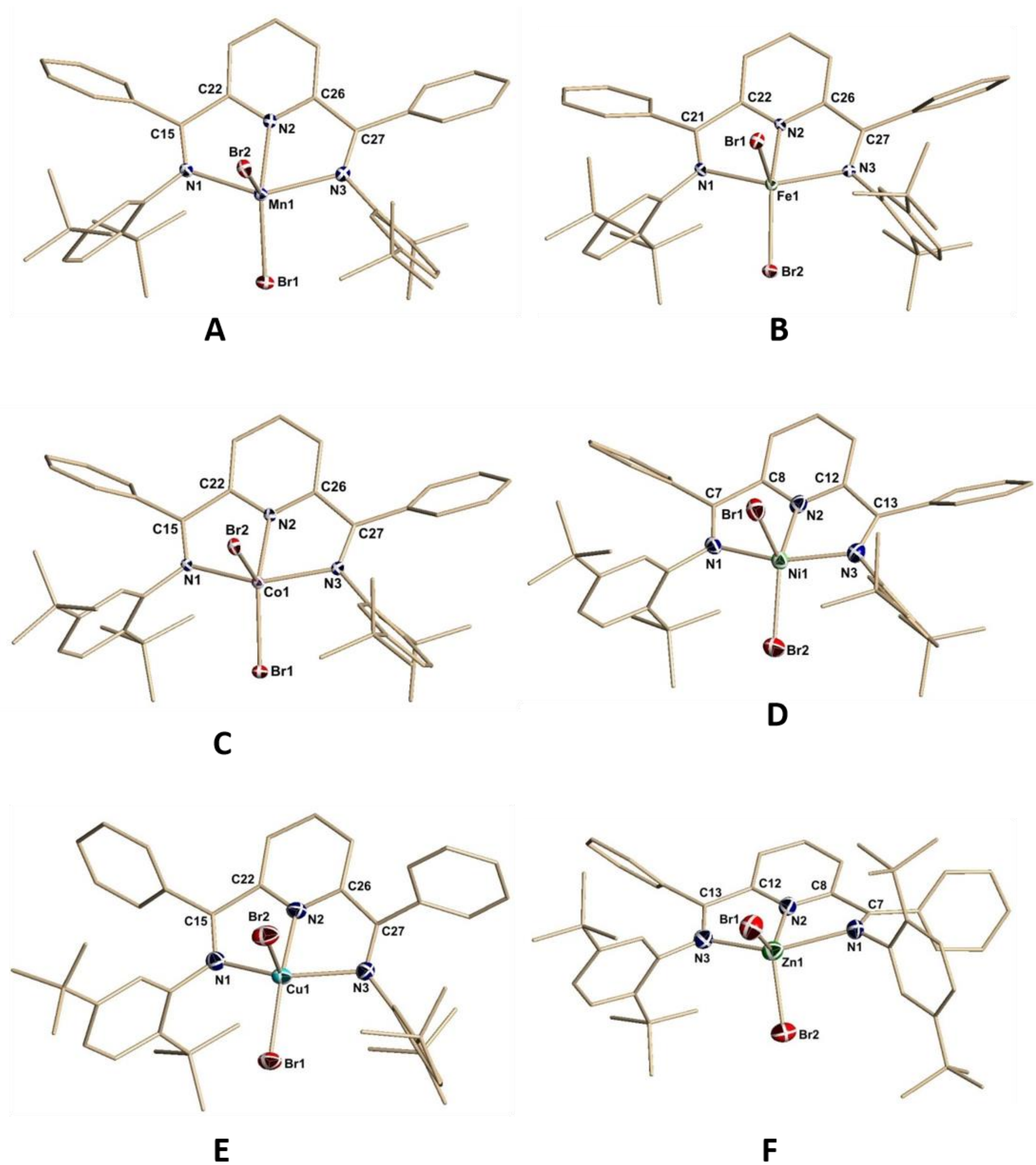

Figure 2.3: X-ray crystallographic structures of first row transition metal bromides with the DIMPY ligand scaffold. Hydrogen atoms and solvent atoms omitted for clarity.

[2.2.2] Analysis of structure geometries and distortions

The X-ray structures determined for the compounds reported in Figure 2.3 reveal neutral mononuclear complexes in which the central metal retains an oxidation state of +2. All of the DIMPY nitrogen atoms are bound to the metal ion and in all cases, both of the bromides remain bound, resulting in complexes with a coordination number of 5. Using the calculations for the τ parameter outlined in equation 2.1, it was determined that all of the complexes exhibited in Figure 2.3 adopted distorted trigonal bipyramidal geometries. The basal plane is formed by the three nitrogen donors of the DIMPY ligand and one of the bromides. The central atom lies slightly above the basal plane in all of the structures. The calculated τ parameters are summarized in Table 2.1.

Table 2.1: Calculated τ parameters for X-ray structures **2A-F**.

	2A	**2B**	**2C**	**2D**	**2E**	**2F**
α	141.18	146.95	148.29	145.07	147.27	146.09
β	70.47	73.48	74.26	77.6	76.25	71.54
τ	**1.18**	**1.22**	**1.23**	**1.13**	**1.18**	**1.24**

The X-ray crystal structures that are the most distorted from *sp* contain Fe (**2B**), Co (**2C**) and Zn (**2F**) ions.

[2.2.3] Analysis of important bond lengths trends within the 1st row

For this family of complexes, the metal-nitrogen bonds follow a pattern where the M-N_{imine} bonds are longer than the M-$N_{pyridine}$ bonds. The difference in the two metal-nitrogen bonds increases as one moves across the row of transition metals. The metal-bromide bond lengths remain relatively constant. This data is shown in Table 2.2 and Figure 2.4. This can be explained by taking a closer look at the metal to ligand bonding. One can think of the imine and pyridine nitrogens as trigonal; thus the ideal bond angles would be 120°. This is, nevertheless, not the case with DIMPY ligands as the substituents on the nitrogen atoms are non-equivalent; however, following this analogy, it is assumed that the pyridine lone pair should be directed directly towards the metal center, whereas the imine nitrogen lone pairs are not directly oriented towards the metal center. Consequently, the lone pair oriented directly towards the metal center will provide more overlap with the metal, thereby resulting in a stronger and shorter bond. A schematic using average bond angles from structures **2A-2F** is shown in Figure 2.4.

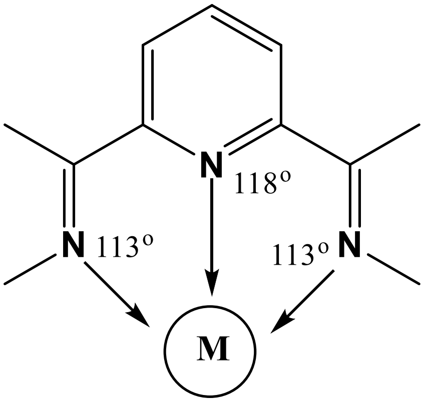

Figure 2.4: Schematic of nitrogen-metal bonding from DIMPY ligand to metal center, *M*, in structures **2A-2F** including average bond angles.

Table 2.2: Experimental bond lengths for X-ray structures **2A-2F**.

	2A	**2B**	**2C**	**2D**	**2E**	**2F**
M-N$_{py}$	**2.216(3)**	**2.0690(19)**	**2.054(2)**	**1.982(5)**	**1.935(4)**	**2.071(4)**
M-N$_{imine(1)}$	2.254(3)	2.170(2)	2.160(2)	2.134(5)	2.228(4)	2.273(4)
M-N$_{imine(2)}$	2.268(3)	2.163(2)	2.160(2)	2.132(5)	2.120(4)	2.446(4)
M-N$_{imine(AVG)}$	**2.261**	**2.1665**	**2.16**	**2.133**	**2.174**	**2.3595**
M-Br$_1$	2.5083(7)	2.4670(4)	2.4517(5)	2.4493(10)	2.5702(10)	2.3643(8)
M-Br$_2$	2.4647(7)	2.3946(4)	2.3867(5)	2.3708(11)	2.3212(9)	2.3590(9)
M-Br$_{(AVG)}$	**2.4865**	**2.4308**	**2.4192**	**2.41005**	**2.4457**	**2.36165**

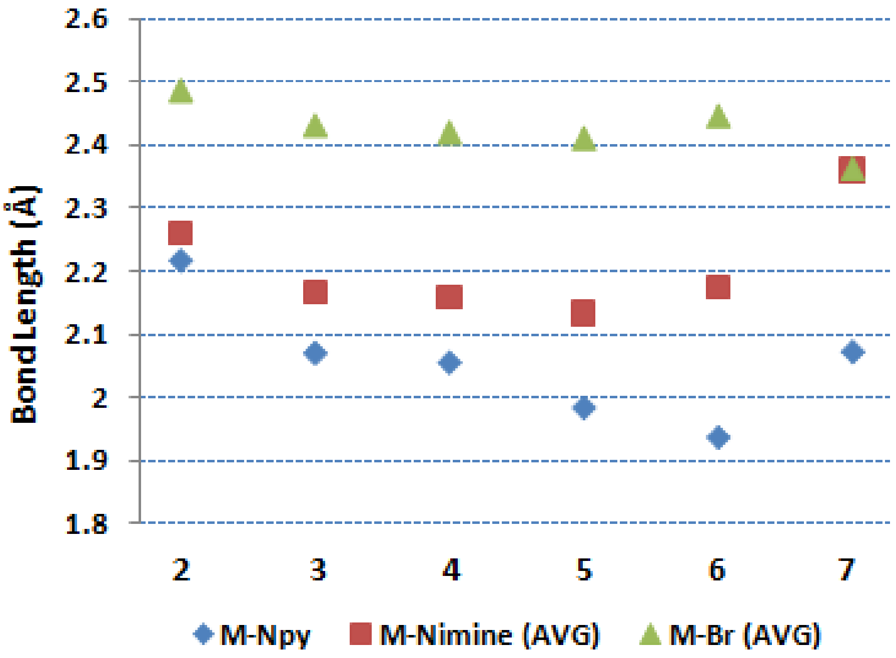

Figure 2.5: Graphic representation of metal-nitrogen, Nimine and Npy, and metal-bromide bonds in X-ray structures **2A-2F** (2-7).

Another important trend that can be seen in this data is that there appears to be a trend in the metal-nitrogen bonds across the row in that they seem to decrease for structure **2A** through **2D** and then increase again through **2F**. This is likely owing to the fact that as one moves across the row, there is a marked decrease in covalent radius. Thus, the atom size will decrease across the row, yielding harder species with increased charge density. This would cause the bond lengths to decrease as the covalent radius decreases. However, another important factor to consider is the number of d electrons. It can be seen that at Cu and Zn, bonds start to get longer again and the difference is much more pronounced between N_{py} and N_{imine}. This is due to the fact that as one moves across the row, the d orbital occupancy increases from 5 to 10 resulting in increased repulsion and longer bonds. Consequently, in structures **2E** and **2F**, the d orbital shell is essentially full and there are not as many appropriate acceptor orbitals for the ligand to donate into; thus, the bond lengths becomes longer.

Furthermore, one can see that there is a larger discrepancy in the bond lengths of the N_{py} bonds compared to the N_{imine} bonds moving across the row. This is likely due to the fact that there is poor overlap between the N_{imine} and the metal, resulting in little π-acceptor interaction and increasingly longer bonds. The N_{py} on the other hand, although generally known as a poor π-acceptor, does have the appropriate geometry to accept some electron density back from the metal thus, accounting for the stronger/shorter bonds and increased discrepancy in bond lengths.

[2.2.4] Analysis of magnetic properties

As mentioned in Chapter 1, complexes containing transition metals with the DIMPY ligand tend to adopt high spin configurations. This was also qualified through computational analysis. It can thus be assumed that complexes **2A** through **2F** would be high spin complexes. This assumption can be further cemented through analysis of the magnetic properties of the complexes, i.e. determination of their magnetic moment, μeff, and the number of unpaired electrons, n.

In order to calculate the magnetic moment of the transition metal bromide- DIMPY complexes, the Evans method was used.[28] The Evans technique is applicable to solutions and is based on the frequency shift induced in an NMR signal of co-dissolved compound, tetramethylsilane or TMS, by the additional magnetic field caused by the paramagnetic species.

Typically, the experiments are run using an NMR tube filled with the paramagnetic species in solvent with the TMS along with a capillary tube with TMS alone. The relative frequency shift produced by the presence of the paramagnetic species in relation to the TMS alone is used in order to calculate the magnetic moment. The equation requires the use of the difference between the frequency shifts for the TMS and that of the paramagnetic species with the TMS, Δf, the spectrometer frequency, f, the mass of the complex, m, the density of the solvent, do, the density of the solution, ds, the mass susceptibility of the solvent, X_o and the mass susceptibility of the solute, Xg:

$$Xg = -\frac{3\Delta f}{4pfm} + Xo + \frac{Xo(do - ds)}{m}$$

Once the mass susceptibility of the solute is found, this can be used to calculate the effective magnetic moment, μeff, using the temperature, T:

$$\mu eff = 797.8(TXg)^{1/2}$$

The theoretical and experimental values for the effective magnetic moment, μeff are shown in Table 2.3 for the various paramagnetic transition metal bromides-DIMPY complexes.

---

[28] (a) D.F. Evans, *J. Chem. Soc*., **1959**, 2003. (b) D.H. Lives, S.I. Chan*, Anal. Chem*., **1970**, 42, 971.

The theoretical values (*μeff, theor*) were calculated using the spin-only formula and the theoretical number of unpaired electrons for the high spin paramagnetic species as well as their respective geometries. The experimental values (*μeff, exp*) were calculated using Evan's method. Included in the table are the commonly experimentally observed (*μeff, obs*) values for the metal ions contained throughout the literature. [29]

Table 2.3: Theoretical and experimental effective magnetic moment, μ*eff*, values for paramagnetic structures.

Compound	**μ_{eff}, theor**	**μeff, obs**	**μeff, exp**
$MnBr_2$-DIMPY	5.92	5.7-6.0	5.88
$FeBr_2$-DIMPY	4.90	5.0-5.6	5.15
$CoBr_2$-DIMPY	3.87	4.3-5.2	4.34
$NiBr_2$-DIMPY	2.83	2.9-3.9	2.97
$CuBr_2$-DIMPY	1.73	1.9-2.1	2.14

As can be seen in Table 2.3, most of the experimentally calculated values are quite close to those predicted theoretically. The small deviations in most of the values are likely due to the presence of diminutive amount of impurities; however, they all correlate with the observed values noted in literature. Small amounts of impurities are expected and common in a laboratory setting.

---

[29] G.L. Miessler, P.J. Fischer, D.A. Tarr, *Inorganic Chemistry*, Fifth Edition, Prentice Hall, USA, **2013**, 476.

[2.3] Computational analysis: Bond Lengths, Bond Angles and Electronic Absorption

Computational analysis was completed in collaboration with Dr. Serge Gorelsky in order to extensively probe the electronic features of the structures in Figure 2.3. This was obtained through DFT computational study using the B3LYP functional and mixed DZVP/TZVP basis set. The DIMPY compounds that were studied have the general formulae $C_{47}H_{55}N_3MBr_2$ or more specifically 2,6-bis{1-[(2,5-ditertbutylphenyl)imino]-benzyl}pyridineMBr$_2$.

[2.3.1] Bond lengths and Bond Angles

A comparison of selected experimental and computed bond distances and angles for each compound are shown in Table 2.4.

Table 2.4: Summary of computation results of compounds **2A-2F.**

Bond	Bond length	Computed bond lengths	Bond	Bond length	Computed bond lengths
Mn(1)-N(1)	2.254(3)	2.426	Fe(1)-N(1)	2.163(2)	2.378
Mn(1)-N(3)	2.268(3)	2.426	Fe(1)-N(3)	2.170(2)	2.378
Mn(1)-N(2)	2.216(3)	2.213	Fe(1)-N(2)	2.0690(19)	2.121
Mn(1)-Br(1)	2.4647(7)	2.532	Fe(1)-Br(1)	2.4670(4)	2.510
Mn(1)-Br(2)	2.5083(7)	2.509	Fe(1)-Br(2)	2.3946(4)	2.443
Bond	**Bond angles**	**Computed bond angles**	**Bond**	**Bond angles**	**Computed bond angles**
Mn(1)-N(1)-C(15)	118.7(2)	112.8	Fe(1)-N(1)-C(21)	118.85(16)	111.2
Mn(1)-N(3)-C(27)	120.4(3)	112.8	Fe(1)-N(3)-C(27)	116.91(17)	111.2
Mn(1)-N(2)-C(22)	117.9(2)	119.9	Fe(1)-N(2)-C(22)	119.94(15)	119.7
Mn(1)-N(2)-C(26)	119.0(2)	119.9	Fe(1)-N(2)-C(26)	118.68(16)	119.7
N(1)-Mn(1)-N(2)	71.36(11)	71.0	N(1)-Fe(1)-N(2)	73.48(7)	73.3
N(3)-Mn(1)-N(2)	70.47(11)	71.0	N(3)-Fe(1)-N(2)	74.40(7)	73.3
N(1)-Mn(1)-N(3)	141.18(11)	141.9	N(1)-Fe(1)-N(3)	146.95(7)	146.6
N(1)-Mn(1)-Br(1)	102.27(8)	98.6	N(1)-Fe(1)-Br(1)	96.77(5)	95.5
N(3)-Mn(1)-Br(1)	100.16(8)	98.6	N(3)-Fe(1)-Br(1)	95.13(5)	95.5
N(1)-Mn(1)-Br(2)	96.57(8)	98.7	N(1)-Fe(1)-Br(2)	99.44(5)	98.6
N(3)-Mn(1)-Br(2)	97.57(7)	98.7	N(3)-Fe(1)-Br(2)	100.61(5)	98.6
N(2)-Mn(1)-Br(1)	136.08(8)	120.7	N(2)-Fe(1)-Br(1)	97.94(5)	109.8
N(2)-Mn(1)-Br(2)	101.46(8)	114.2	N(2)-Fe(1)-Br(2)	141.17(5)	121.4

Br(1)-Mn(1)-Br(2)	122.45(3)	125.1	Br(1)-Fe(1)-Br(2)	120.880(16)	128.9

Table 2.4 continued

Bond	Bond lengths	Computed Bond lengths	Bond	Bond lengths	Computed bond lengths
Co(1)-N(1)	2.160(2)	2.351	Ni(1)-N(1)	2.134(5)	2.246
Co(1)-N(3)	2.054(2)	2.352	Ni(1)-N(3)	2.132(5)	2.246
Co(1)-N(2)	2.054(2)	2.056	Ni(1)-N(2)	1.982(5)	1.991
Co(1)-Br(1)	2.4517(5)	2.429	Ni(1)-Br(1)	2.4493(10)	2.473
Co(1)-Br(2)	2.3867(5)	2.451	Ni(1)-Br(2)	2.3708(11)	2.444
Bond	**Bond angles**	**Computed bond angles**	**Bond**	**Bond angles**	**Computed bond angles**
Co(1)-N(1)-C(15)	116.49(18)	110.0	Ni(1)-N(1)-C(7)	114.5(4)	110.5
Co(1)-N(3)-C(27)	117.96(18)	110.0	Ni(1)-N(3)-C(13)	116.7(4)	110.5
Co(1)-N(2)-C(22)	118.33(18)	119.6	Ni(1)-N(2)-C(8)	117.9(4)	119.2
Co(1)-N(2)-C(26)	119.66(17)	119.6	Ni(1)-N(2)-C(12)	119.1(4)	119.2
N(1)-Co(1)-N(2)	75.26(8)	74.8	N(1)-Ni(1)-N(2)	77.6(2)	76.8
N(3)-Co(1)-N(2)	74.26(8)	74.8	N(3)-Ni(1)-N(2)	76.8(2)	76.8
N(1)-Co(1)-N(3)	148.29(8)	149.5	N(1)-Ni(1)-N(3)	153.95(19)	153.5
N(1)-Co(1)-Br(1)	95.25(6)	96.3	N(1)-Ni(1)-Br(1)	92.85(13)	94.2
N(3)-Co(1)-Br(1)	96.85(6)	96.4	N(3)-Ni(1)-Br(1)	94.39(13)	94.2
N(1)-Co(1)-Br(2)	100.08(6)	97.2	N(1)-Ni(1)-Br(2)	99.46(14)	94.7
N(3)-Co(1)-Br(2)	99.01(6)	97.2	N(3)-Ni(1)-Br(2)	98.58(14)	94.7
N(2)-Co(1)-Br(1)	96.84(6)	114.3	N(2)-Ni(1)-Br(1)	95.26(14)	106.5
N(2)-Co(1)-Br(2)	143.23(6)	119.1	N(2)-Ni(1)-Br(2)	145.07(14)	113.4
Br(1)-Co(1)-Br(2)	119.927(18)	126.6	Br(1)-Ni(1)-Br(2)	119.66(4)	140.1

Table 2.4 continued

Bond	Bond lengths	Computed bond lengths	Bond	Bond lengths	Computed bond lengths
Cu(1)-N(1)	2.120(4)	2.176	Zn(1)-N(1)	2.273(4)	2.405
Cu(1)-N(3)	2.228(4)	2.176	Zn(1)-N(3)	2.446(4)	2.406
Cu(1)-N(2)	1.935(4)	2.029	Zn(1)-N(2)	2.071(4)	2.114
Cu(1)-Br(1)	2.3212(9)	2.448	Zn(1)-Br(1)	2.3643(8)	2.438
Cu(1)-Br(2)	2.5702(10)	2.561	Zn(1)-Br(2)	2.3590(9)	2.413

Bond	**Bond angles**	**Computed bond angles**	**Bond**	**Bond angles**	**Computed bond angles**
Cu(1)-N(1)-C(15)	112.8(3)	112.7	Zn(1)-N(1)-C(7)	113.5(3)	110.6
Cu(1)-N(3)-C(27)	108.0(3)	112.7	Zn(1)-N(3)-C(13)	110.5(3)	110.6
Cu(1)-N(2)-C(22)	119.2(3)	118.8	Zn(1)-N(2)-C(8)	118.5(3)	119.8
Cu(1)-N(2)-C(26)	119.4(3)	118.8	Zn(1)-N(2)-C(12)	122.2(3)	119.8
N(1)-Cu(1)-N(2)	78.22(15)	76.5	N(1)-Zn(1)-N(2)	74.72(16)	73.1
N(3)-Cu(1)-N(2)	76.25(15)	76.5	N(3)-Zn(1)-N(2)	71.54(16)	73.1
N(1)-Cu(1)-N(3)	147.27(14)	152.8	N(1)-Zn(1)-N(3)	146.09(16)	146.2
N(1)-Cu(1)-Br(1)	100.28(10)	97.3	N(1)-Zn(1)-Br(1)	102.93(11)	97.8
N(3)-Cu(1)-Br(1)	100.66(10)	97.3	N(3)-Zn(1)-Br(1)	96.93(10)	97.8
N(1)-Cu(1)-Br(2)	104.68(11)	95.4	N(1)-Zn(1)-Br(2)	99.63(11)	97.3
N(3)-Cu(1)-Br(2)	95.24(11)	95.4	N(3)-Zn(1)-Br(2)	97.18(11)	97.3
N(2)-Cu(1)-Br(1)	168.51(12)	130.6	N(2)-Zn(1)-Br(1)	120.58(11)	114.3
N(2)-Cu(1)-Br(2)	89.42(12)	105.3	N(2)-Zn(1)-Br(2)	125.53(11)	119.4
Br(1)-Cu(1)-Br(2)	101.94(3)	124.1	Br(1)-Zn(1)-Br(2)	113.54(3)	126.3

The bond lengths and angles are in good agreement both in magnitude as well as in trend. The most obvious thing to note is that the computed structures are higher in symmetry, which is not a surprise as this is most often the case.This is due to the computation models being run under ideal conditions; versus the crystal structures containing diminuitive amounts of impurites, which is common and expected in a laboratory setting.

Additionally, further computations were undertaken in order to determine the Mayer bond order by means of B3LYP with TZVP using PCM model (CH_2Cl_2). The Mayer bond order is a specific method of computing bond order in inorganic compounds. The bond order is an indication of covalency – the higher the bond order, the higher the covalency. [30]

---

[30] A.J. Bridgeman, G. Cavigliasso, L.R.Ireland, J. Rothery, *Dalton Trans.*, **2001,** 35.

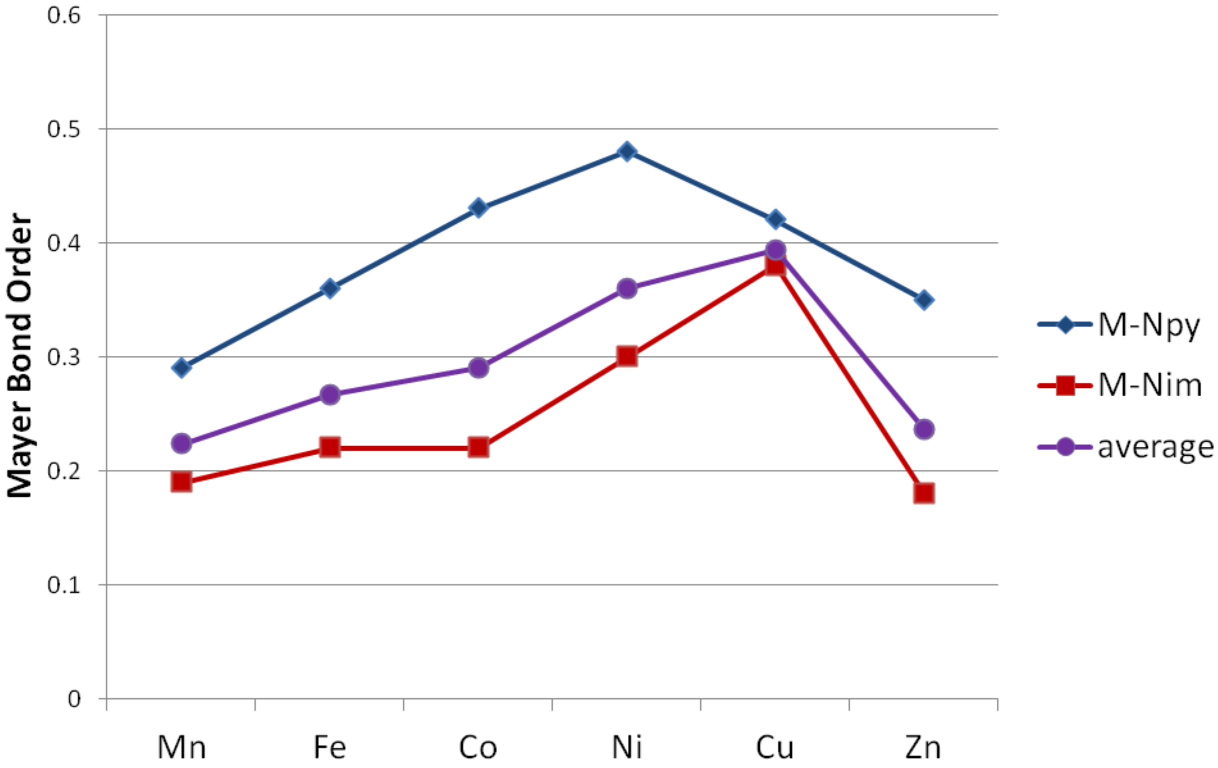

Figure 2.6: Computed Mayer bond order for metal-nitrogen bonds exhibiting trend in covalency.

Figure 2.6 shows that as one moves across the periodic table within the transition metal centers studied, there is an increase in covalency from manganese until between nickel and copper after which one sees a decrease between copper and zinc. Interestly, this would correlate to longer bond lengths in complexes where there is a smaller bond order and vice versa. Interesingly, if one were to map the trend in bond length according to this data, it would look like the inverse of that in Figure 2.6 which is analogous to that seen in the experimental bond lengths in Figure 2.5 which provides further reasoning behind the trend seen.

Furthermore, it can be determined from this figure that the covalency is quite weak. A covalent bond would correspond to a bond order of one. The higher the bond order, the more stable the bond. In this case, all of the bond orders are less than 0.5. These low bond orders indicate that the bonding is likely electrostatic in nature; thereby, the bond is weak.

[2.3.2] Electronic Absorption

Similarly, the electronic absorption data was computed in order to verify that the computed values correlate with those determined experimentally. The experimental electronic absorption data is shown in Figure 2.6 for structures **2A** through **2F**. The data was collected using dichloromethane as a solvent.

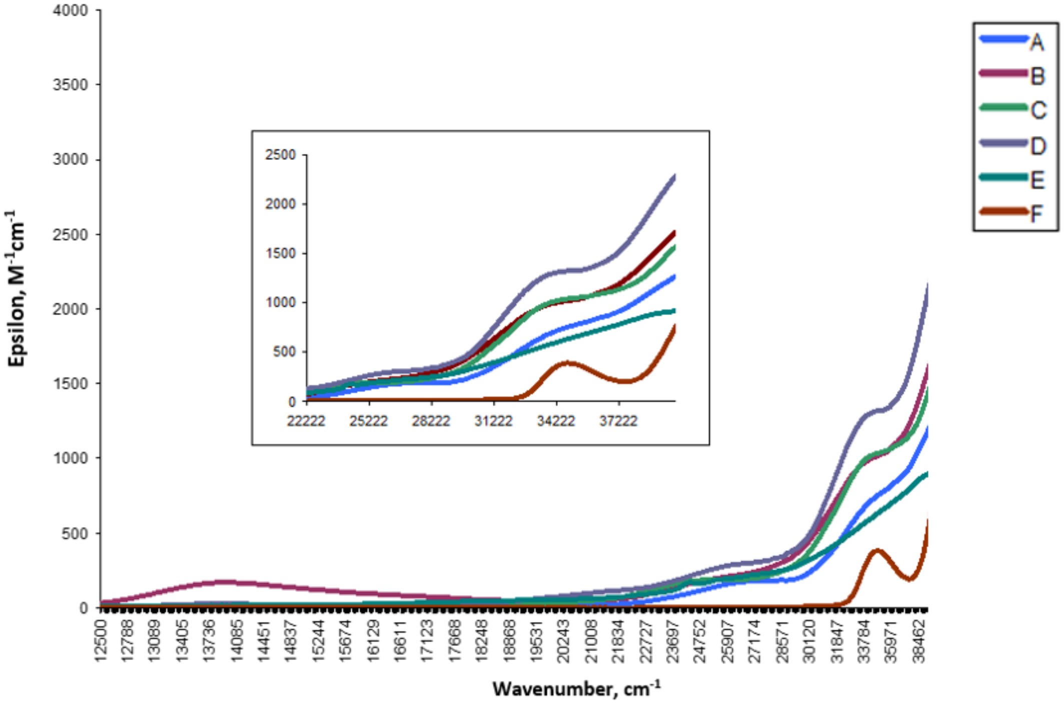

Figure 2.7: Eperimental electronic absorption data for structures **2A** through **2F**.

Table 2.5: Peaks in wavenumbers, cm^{-1}, of experimental electronic absorption data for structures **2A** through **2F**.

2A	2B	2C	2D	2E	2F
33,898.31	33,333.33	33,898.31	33,898.51	24,330.90	*34,722.22
26,737.97	*14,005.60	25,252.53	21,276.60	--	--
--	--	--	*13,908.21	--	--

*denotes peak with well-defined maximum, the majority of assigned peaks are an average of a prominent shoulder

Table 2.5 shows the wavenumber values corresponding to the peaks in the experimental electronic absorptions. All of the spectra appear somewhat similar with prominent peaks between 24,000 and 35,000 cm^{-1}. These are likely the peaks corresponding to the DIMPY scaffold. This is further qualified through analysis of the electronic absorption data for the DIMPY ligand alone, which has been published previously in numerous publications.[31] The remaining peaks are expectedly due to the different metal centers. Beginning with complex **2A** which contains a Mn metal center that is yellow, one sees three peaks as noted. In addition, moving across the table, **2B** is a blue complex containing a Fe center. One notices a red shift to a longer wavelength and thus lower wavenumber. Similarly to **2A**, complex **2C** containing a Co metal center, is also yellow and has very similar absorption maxima. **2D**, however, which contains a Ni center, is brown and contains two maxima, one of which is significantly red-shifted when compared to **2A**. Complex **2E** which contains a Cu center, is red and one of the maxima is blue-shifted in comparison to **2A**. Lastly, the absorption maxima for **2F,** which is a pale yellow complex containing a Zn center are quite similar to **2A** although somewhat blue-shifted.

---

[31] (a)P.M. Castro, P. Lahtinen, K. Axenov, J. Viidanoja, T. Kotiaho, M. Leskela, T. Repo, *Organometallics*, **2005**, 24(15). (b) V.C. Gibson, C. Redshaw, G.A. Solan, *Chem. Rev.*, **2007**, 107(5). (c) J. Scott, S. Gambarotta, I. Korobkov, Q. Knijnenburg, D. de Bruin, P.H.M. Budzelaar, *J. Am. Chem. Soc.,* **2005**, 127(49).

Figures 2.8 through 2.13 contain graphics that superimpose the experimental and computed electronic absorption data.

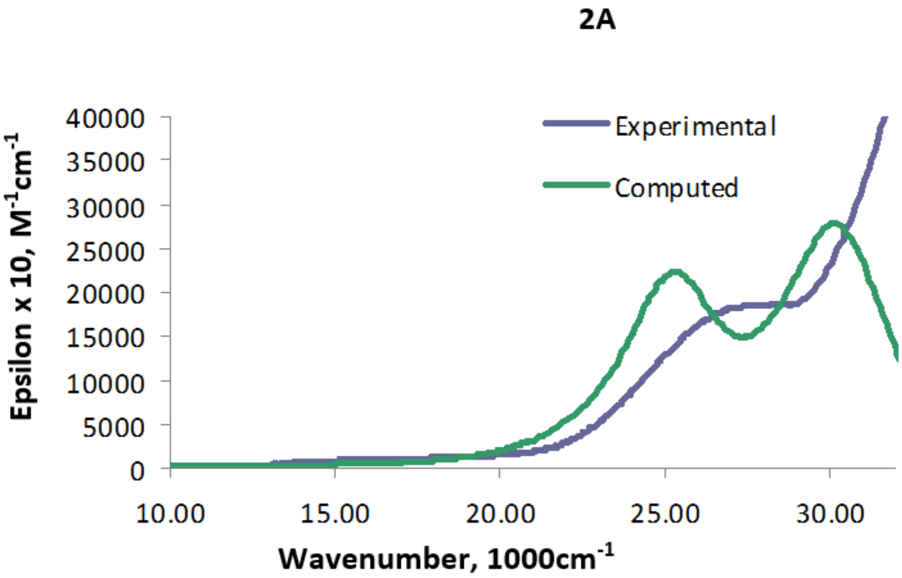

Figure 2.8: Comparison of computed and experimental electronic absorption data for structure **2A**.

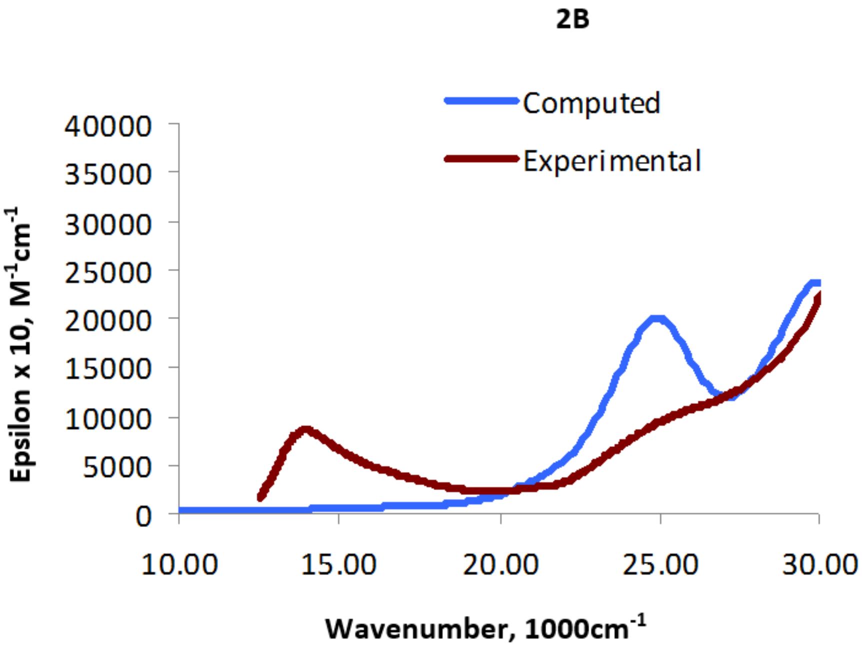

Figure 2.9: Comparison of computed and experimental electronic absorption data for structure **2B**.

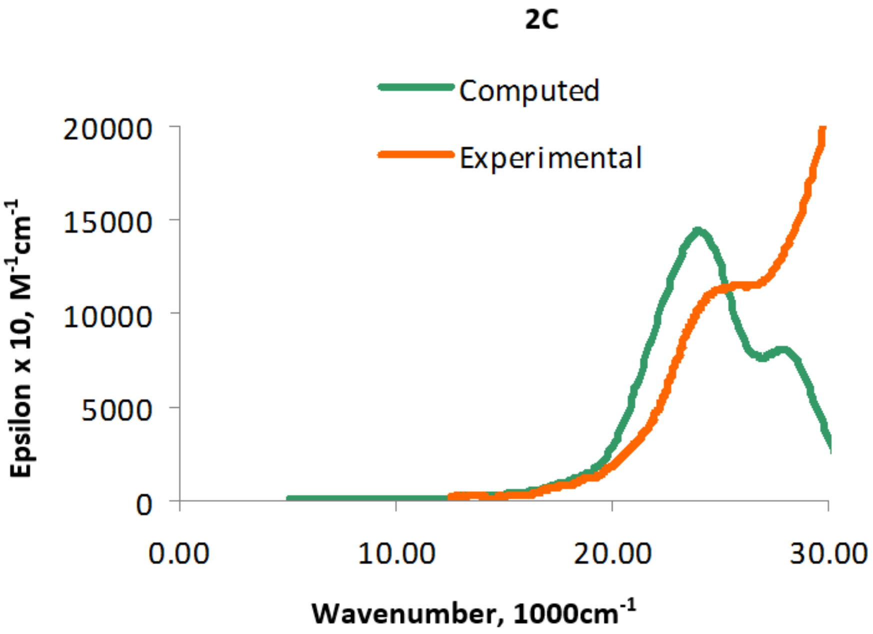

Figure 2.10: Comparison of computed and experimental electronic absorption data for structure **2C**.

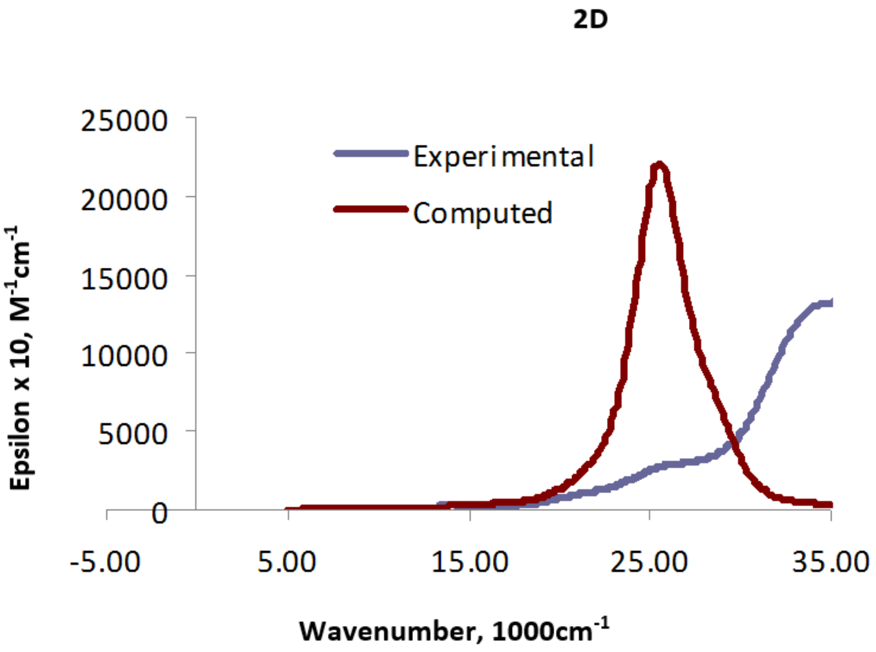

Figure 2.11: Comparison of computed and experimental electronic absorption data for structure **2D**.

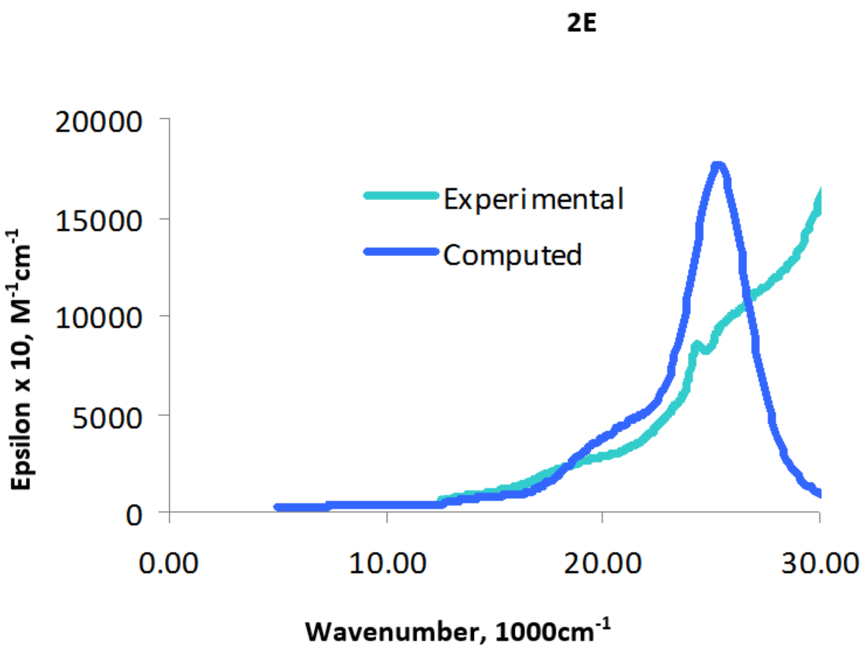

Figure 2.12: Comparison of computed and experimental electronic absorption data for structure **2E**.

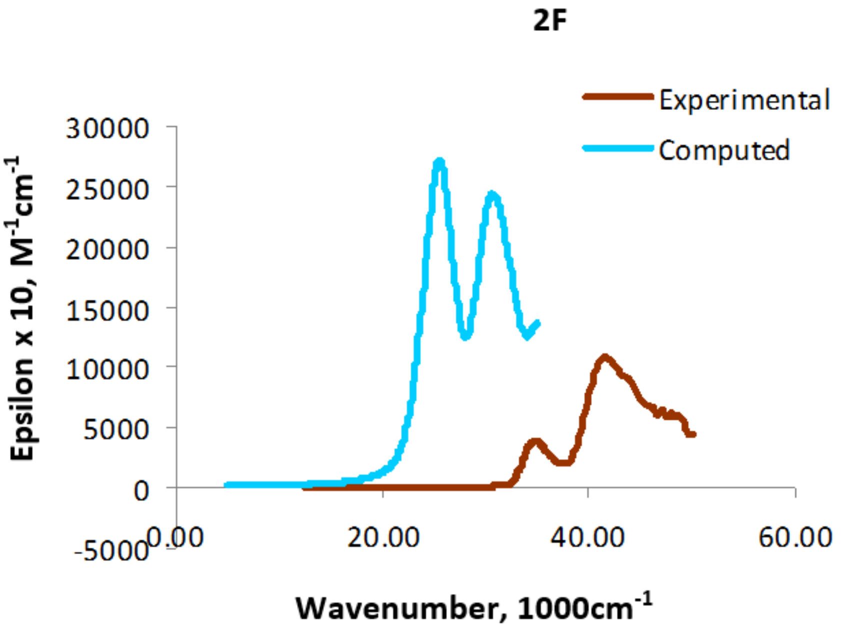

Figure 2.13: Comparison of computed and experimental electronic absorption data for structure **2F**.

All of the above electronic absorption spectra show correlation between the experimental and computed data. It is expected that they will not be identical; however, the peaks correlate. To explain further, it is expected that the computed and experimental data are not identical. In fact, it would be nearly impossible for them to be so. There does not exist a quantitative means to compare the data. This is because, in the case of the experimental spectrum, the researcher is looking at a spectrum that is effected by solvent/solvation and any molecular variations that are happening during the measurement. The computations, on the other hand, begin with a gas phase isolated molecule and give only values of the electronic transitions, i.e. a line spectrum with no width to the peaks. The next phase is to add solvent which is added as an electric field that surrounds the molecule. Finally, some ‘width’ is added to each of the electronic transition lines. This can be varied to make a better match. In the end, as long as there is a correlation and no unexpected peaks, it is considered a good match. Indeed, this is the case with the spectra above.

[2.4] Conclusion

Overall, we were successful in reporting distinctive complexes of first row transition metal bromides supported by the DIMPY scaffold. The DIMPY scaffold readily reacted with the transition metal bromides to allow the preparations, isolation and analysis of a unique set of compounds. The resulting complexes were able to be fully characterized using ^{1}H and ^{13}C NMR, elemental analysis, mass spectrometry, UV-Vis absorption as well as IR absorption.

Furthermore, these coordination complexes were extensively analyzed in order to yield important information regarding bonding of these complexes. This includes their geometries, structural distortions, bond lengths and bond angles. From this data, important trends in coordination of these transition metal bromides to the DIMPY scaffold were able to be mapped, i.e. trends in bond lengths between the ligand and the metal. Additionally, the magnetic moment of these complexes was calculated experimentally, providing information regarding the magnetic properties.

Lastly, computations were run in order to correlate the experimental bond lengths, bond angles and electronic absorption with the computed data. Fortunately, all of the experimental data correlated with the computational data within acceptable limits. The computed data also correlated with bonding trends drawn from experimental data and expanded on reasoning as to why these trends are seen, i.e, the Mayer Bond Order as reasoning behind the trends in metal-ligand bond length.

[2.5] Experimental: Complexes of 1st row transition metal bromides with the DIMPY ligand

General Methods. Reactions were performed in a glovebox with a nitrogen atmosphere, with the exception of ligand synthesis, which was performed using standard Schlenk technique under a flow of N_2. All solvents were parged with nitrogen and then dried by passage through a column of activated alumina using an apparatus purchased from Anhydrous Engineering. Deuterated chloroform was dried using activated molecular sieves. Metal halides were purchased from Strem Chemicals and used as received. All other chemicals were purchased from Aldrich and used without further purification. NMR spectra were acquired on a Bruker Avance 300 MHz spectrometer with CD_2Cl_2, and $CDCl_3$ as solvents and internal standards. Elemental analyses for **1, 1A, 1B,** and **2A-2F** were performed by Midwest Microlab LLC, Indianapolis IN. Mass spectrometry (MS) was completed by the Holmes group at the University of Ottawa using TOF MS ES on a Micromass-Q TOF II. Values are reported in g/mol and are ranked in order of decreasing intensity. The rank is provided in brackets.

(1) 2,6-dibenzoylpyridine:

The synthetic procedure was adapted from a literature preparation described by Esteruelas et al[32]. In the glovebox, a 250mL round bottom flask was charged with a mixture of 2,6-dicarbonyl pyridine dichloride (10.0g, 49mmol) and $AlCl_3$ (16.3g, 122.5mmol) This flask was removed from the dry box and dried benzene was added quickly (~100mL) while maintaining a nitrogen atmosphere, using a Schlenk line. The reaction mixture was heated to reflux for 6 hours and a dark orange/brown solution formed. The mixture was then cooled to room temperature and stirred for 14 hours. It was then heated to reflux for an additional 6 hours and cooled to room temperature. The following work up was performed under lab atmosphere. The $AlCl_3$ was quenched using cold distilled water and an ice water bath. The organic layer was then collect, and the remaining aqueous layer was extracted with diethyl ether (3x ~30mL). Organic layers were combined and dried over $MgSO_4$. Solvents were removed via rotary evaporation leaving a red-white powder. Crude powder was washed with cold diethyl ether resulting in a fine light pink powder.

Yield: 7.194g (51%)

^{1}H NMR ($CDCl_3$, 300 MHz): δ 8.28-8.25 (d, 2H, CH_{Ar}), δ 8.17-8.13 (d, 4H, CH_{Ar}), δ 8.12-8.06 (m, 1H, CH_{Ar}), δ 7.58-7.52 (t, 2H, CH_{Ar}), δ 7.43-7.29 (t, 4H, CH_{Ar}).

---

[32] M.A. Esteruelas, A.M. Lopez, L. Mendez, M. Olivan, E. Onate, *Organometallics*, **2003**, 22, 395.

^{13}C NMR ($CDCl_3$, 300 MHz): δ 192.92 (C=O), δ 154.18 (C_{Ar}), δ 138.76 (C_{Ar}), δ 136.35 (C_{Ar}), δ 133.40 (C_{Ar}), δ 131.52 (C_{Ar}), δ 128.45 (C_{Ar}), δ 127.33 (C_{Ar}).

(1A) 2,6-Bis{1-[(2,5-ditertbutylphenyl)imino]-benzyl}pyridine:

This procedure was adapted from a literature preparation described by Kleigrewe at al[33] as reported by Titel Jurca[34]. A 250mL round bottom flask was charged with 2,6-dibenzoylpyridine (1) (5.4g, 18.8mmol), 2.5-ditertbutylaniline (7.4g, 41.4mmol), p-toluenesulfonic acid (0.1g, catalytic) in toluene (~150mL). A Dean Stark trap was attached to the flask and the reaction mixture was placed under vacuum and reduced to a thick brown paste. The brown paste was dissolved in cold methanol and ice cubes were added to precipitate a solid yellow product. The product was collected by filtration and washed with a minimal amount of cold 9:1 hexanes:ether solution to remove aniline impurities. The filtrate was reduced again to a thick paste and the above procedure was repeated several times to yield a yellow powder.

Yield: 8.377g (67%)

^{1}H NMR ($CDCl_3$, 300 MHz): δ 8.54-8.50 (d, 1H, CH_{Ar}), δ 8.27-8.23 (d, 1.5H, CH_{Ar}), δ 7.93-7.89 (d, 3H, CH_{Ar}), δ 7.74-7.67 (t, 1.5H, CH_{Ar}), δ 7.60-7.36 (m, 10H, CH_{Ar}), δ 7.32-7.26 (m, 5H, CH_{Ar}), δ 7.20-7.14 (m, 9H, CH_{Ar}), δ 7.09-7.00 (m, 10H, CH_{Ar}), δ 6.96-6.91 (dd, 5H, CH_{Ar}), δ 6.23-6.13 (m, 6H, CH_{Ar}), δ 3.54-3.45 (q, 2H, $CH_{2\ ether}$), δ 2.38 (s, 1H, $CH_{3\ toluene}$), δ 1.55 (s, 10H, CH_3), δ 1.51 (s, 14H, CH_3), δ 1.45 (s, 18H, CH_3), δ 1.39 (s, 11H, CH_3), δ 1.30 (s, 1H, CH_3), δ 1.26-1.20 (t, 3H, $CH_{3\ ether}$), δ 1.06 (s, 10H, CH_3), δ 0.97 (s, 15H, CH_3), δ 0.95 (s, 16H, CH_3), δ 0.92 (s, 9H, CH_3).

---

[33] N. Kleigrewe, W. Steffan, T. Blomker, G. Kehr, R. Frlich, B. Wibbeling, G. Erker, J.C. Wasilke, G. Wu, G.C. Bazan, *J. Am. Chem. Soc.*, **2005**, 127, 40, 13955.

[34] T. Jurca, K. Dawson, I. Mallov, T. Burchell, G.P.A. Yap, D.S. Richeson, *Dalton Trans*., **2010**, 39, 1266.

^{13}C NMR ($CDCl_3$, 300 MHz): δ 164.29 (C=N), δ 162.45 (C=N), δ 161.98 (C=N), δ 157.79 (C=N), d δ 156.57 (C(2) $_{\text{pyridine}}$), δ 155.96 (C(2) $_{\text{pyridine}}$), δ 155.17 (C(2) $_{\text{pyridine}}$), δ 148.99 (C(5) $_{\text{ditertbutyl aniline substituent}}$), δ 148.89 (C(5) $_{\text{ditertbutyl aniline substituent}}$), δ 148.54 (C(5) $_{\text{ditertbutyl aniline substituent}}$), d 148.38 (C(5) $_{\text{ditertbutyl aniline substituent}}$), δ 148.13 (C(1) $_{\text{ditertbutyl aniline substituent}}$), δ 140.00-118.50 (35 unique peaks, C_{Ar}), δ 35.66 (C), d 35.51 (C), δ 34.44 (C), δ 34.29 (C), δ 34.23 (C), δ 31.63 (CH_3), δ 31.56 (CH_3), δ 31.32 (CH_3), δ 30.81 (CH_3), δ 30.65 (CH_3), δ 30.46 (CH_3).

(1B) 2,6-Bis{1-[(2,6-diisopropylphenyl)imino]-benzyl}pyridine:

Following a procedure similar to that described for **(2)**, a mixture of 2,6-dibenzoylpyridine (5.0 g, 17.4 mmol), 2,6-diisopropylaniline (7.5 g, 38.3 mmol), and p-toluenesulfonic acid (0.2 mg) in toluene (50 mL) were placed in a round bottom flask equipped with a Dean–Stark trap. Under a nitrogen atmosphere, the reaction mixture was heated to reflux in an oil bath at 140°C for 48 hours then cooled to room temperature and the solvent was removed under vacuum to give a dark yellow oil. Hexanes were added and a small quantity of a white solid was removed by filtration. The filtrate was removed under vacuum yielding a dark yellow oil. Methanol (~400 mL) was added to this oil and the mixture was stirred for several minutes, causing the product to precipitate as a yellow solid which was filtered off and rinsed with methanol. The filtrate was reduced to about half the initial volume under vacuum, and then placed in a refrigerator, causing additional product to precipitate, which was filtered off and rinsed with methanol. The product was obtained as a yellow powder.

Yield: 7.2 g (68%).

^{1}H NMR(T = 115◦C, *d6*-dimethyl sulfoxide, 300 MHz) δ 7.82 (br t, 1 H, py, *p*-CH), δ 7.55–7.20 (br m, 12 H, H_{Ar}), δ 6.94 (br s, 6H, H_{Ar}), δ 2.90 (m, 4H, *i*Pr), δ 1.00 (d, 24H, *i*Pr).

^{13}C NMR (T = 115°C, *d6*-dimethyl sulfoxide, 75 MHz) δ 164.6 (C=N imine), δ 155.2 (py, *o*-C=N), δ 146.2 (CH_{Ar}), δ 136.8 (Ar-*i*-C), δ 135.5 (CH_{Ar}), δ 130.1 (CH_{Ar}), δ 128.9 (CH_{Ar}), δ 128.1 (CH_{Ar}), δ 123.7 (CH_{Ar}), δ 123.2 (CH_{Ar}), δ 122.7 (CH_{Ar}), δ 28.2 (Ar-*i*Pr, CH-$(CH_3)_2$), δ 22.9 (*i*Pr_{Ar},CH_3), δ 22.3 (*i*Pr_{Ar}, CH_3)

(2A) $MnBr_2$-2,6-Bis{1-[(2,5-ditertbutylphenyl)imino]-benzyl}pyridine: $MnBr_2$ powder (32 mg, 0.149 mmol) was added to a clear yellow solution of **DIMPY** (100 mg, 0.151 mmol) in 8 mL of toluene. The reaction mixture was allowed to stir for 14 hours, gradually becoming opaque beige/yellow. Solution was then held at -20^{o}C overnight, over which time a pale yellow-ochre precipitate formed. Solution was filtered, washed with 5 x 2 mL hexanes, and allowed to dry under vacuum. A pale yellow-ochre powder was isolated in 94% yield. Large yellow cubic crystals suitable for X-ray analysis were grown by diffusion of saturated $CDCl_3$ solution in hexanes, and storing at -20^{o}C for several days. Sample for elemental analysis was obtained by recrystallization in toluene, resulting in a 1:1 toluene adduct. Calculated (%) for [$C_{47}H_{55}Br_2MnN_3$][]: C 64.39, H 6.32, N 4.79, found C 64.92, H 5.97, N 3.90. MS: 880.21(6), 879.21(5), 878.21(2), 877.21(3), 876.21(1), 875.21(5), 874.21(4).

(2B) $FeBr_2$-2,6-Bis{1-[(2,5-ditertbutylphenyl)imino]-benzyl}pyridine: $FeBr_2$ powder (30 mg, 0.139 mmol) was added to a clear yellow solution of **DIMPY** (100 mg, 0.151 mmol) in 8 mL of toluene. The reaction mixture was allowed to stir for 14 hours, gradually becoming opaque dark green. Solution was then held at -20^{o}C overnight, over which time a dark green precipitate formed. Solution was filtered, washed with 5 x 2 mL hexanes, and allowed to dry under vacuum. A dark green powder was isolated in 96% yield. Blue prism-like crystals suitable for X-ray analysis were grown by diffusion of saturated $CDCl_3$ solution in hexanes, and storing at -20^{o}C for several days.

Elemental analysis calculated (%) for [$C_{47}H_{55}Br_2FeN_3$]: C 64.32, H 6.32, N 4.79, found C 64.05, H 6.26, N 4.62. MS: 881.21(7), 880.21(6), 879.21(2), 879.22(4), 877.21(1), 876.94(5), 875.21(3).

(2C) CoBr$_2$-2,6-Bis{1-[(2,5-ditertbutylphenyl)imino]-benzyl}pyridine: $CoBr_2$ powder (15 mg, 0.069 mmol) was added to a clear yellow solution of **DIMPY** (55 mg, 0.083 mmol) in 8 mL of toluene. The reaction mixture was allowed to stir for 14 hours, gradually becoming opaque beige/orange. Solution was then held at -20°C overnight, over which time a dark ochre precipitate formed. Solution was filtered, washed with 5 x 2 mL hexanes, and allowed to dry under vacuum. A dark ochre powder was isolated in 99% yield. Large yellow cubic crystals suitable for X-ray analysis were grown by diffusion of saturated CH_2Cl_2 solution in hexanes, and storing at -20°C for several days. Sample for elemental analysis was obtained by recrystalization in CH_2Cl_2, resulting in a 3:1 DCM adduct of **2C** calculated (%) for [$C_{47}H_{55}Br_2CoN_3$]$_3$[CH_2Cl_2]: C 62.54, H 6.17, N 4.62, found C 62.72, H 6.17, N 4.17. MS: 884.21(7), 883.21(5), 882.21(2), 881.21(3), 880.21(1), 879.21(6), 878.21(4).

(2D) NiBr$_2$-2,6-Bis{1-[(2,5-ditertbutylphenyl)imino]-benzyl}pyridine: $NiBr_2$ powder (30 mg, 0.137 mmol) was added to a clear yellow solution of **DIMPY** (110 mg, 0.166 mmol) in 8 mL of toluene in a Teflon sealed reaction flask. The reaction mixture was allowed to stir for 24 hours at 150°C, The solution gradually turned opaque brown. Solution was then held at -20°C overnight, over which time an ochre precipitate formed. Solution was filtered, washed with 5 x 2 mL hexanes, and allowed to dry under vacuum. Due to poor solubility of $NiBr_2$ starting material, obtaining high yield and high purity presents difficulties, purity is enhanced at the cost of yield by a series of recrystalizations in CH_2Cl_2. An ochre powder was ultimately isolated in 51% yield.. Dark brown block like crystals suitable for X-ray analysis were grown by diffusion of saturated CH_2Cl_2 solution in hexanes, and storing at -20°C for several days. ^1H NMR ($CDCl_3$, 300 MHz): δ 7.89(br t, 1 H, py, *p*-CH), 7.60(br d , 2 H, py, *m*-CH), 7.40-7.10(br m, 12 H, aromatic), 6.96(br d, 1H, aromatic), 6.93(br d, 1 H, aromatic), 6.53(br d, 2 H, aromatic), 1.49(br s, 18H, ^{t}Bu), 0.96(br s, 18H, ^{t}Bu). ^{13}C NMR ($CDCl_3$, 75 MHz). δ 165.6(C=N imine), 152.7(py, *o*-C=N), 149.9(Ar-CH), 148.3 (Ar-CH), 138.9(Ar, *i*-C), 138.1(Ar-CH), 134.3(Ar, *i*-C), 129.8(Ar-CH), 129.3(Ar-CH), 128.3(Ar-CH), 126.1(Ar-CH), 125.0 (Ar-CH), 121.9(Ar-^{t}Bu, C-^{t}Bu), 120.7(Ar-^{t}Bu, C-^{t}Bu), 35.5(Ar-^{t}Bu, C-$(CH_3)_3$), 34.2(Ar-^{t}Bu, C-$(CH_3)_3$), 31.2(Ar-^{t}Bu, CH_3), 30.9(Ar-^{t}Bu, CH_3). Sample for elemental analysis was obtained by recrystalization in CH_2Cl_2, resulting in a 3:1 DCM adduct of **2D** calculated (%) for $[C_{47}H_{55}Br_2NiN_3]_3[CH_2Cl_2]$: C 62.56, H 6.17, N 4.62, found C 62.32, H 6.18, N 3.70. MS: 885.20(9), 884.20(8), 883.20(6), 882.21(4), 881.21(2), 880.21(3), 879.21(1), 878.21(7), 877.21(5).

(2E) CuBr₂-2,6-Bis{1-[(2,5-ditertbutylphenyl)imino]-benzyl}pyridine: $CuBr_2$ powder (32 mg, 0.143 mmol) was added to a clear yellow solution of **DIMPY** (100 mg, 0.151 mmol) in 8 mL of toluene. The reaction mixture was allowed to stir for 14 hours, gradually becoming opaque dark brown. Solution was then held at -20°C overnight, over which time a copper colored precipitate formed. Solution was filtered, washed with 5 x 2 mL hexanes, and allowed to dry under vacuum. A dark copper powder was isolated in 92% yield. Red block like crystals suitable for X-ray analysis were grown by diffusion of saturated CH_2Cl_2 solution in hexanes, and storing at -20°C for several days.^{1}H NMR ($CDCl_3$, 300 MHz): δ 7.89(br t, 1 H, py, *p*-CH), 7.60(br d , 2 H, py, *m*-CH), 7.40-7.10(br m, 12 H, aromatic), 6.96(br d, 1H, aromatic), 6.93(br d, 1 H, aromatic), 6.53(br d, 2 H, aromatic), 1.49(br s, 18H, ^{t}Bu), 0.96(br s, 18H, ^{t}Bu). ^{13}C NMR ($CDCl_3$, 75 MHz). δ 165.6(C=N imine), 152.7(py, *o*-C=N), 149.9(Ar-CH), 148.3 (Ar-CH), 138.9(Ar, *i*-C), 138.1(Ar-CH), 134.3(Ar, *i*-C), 129.8(Ar-CH), 129.3(Ar-CH), 128.3(Ar-CH), 126.1(Ar-CH), 125.0 (Ar-CH), 121.9(Ar-^{t}Bu, C-^{t}Bu), 120.7(Ar-^{t}Bu, C-^{t}Bu), 35.5(Ar-^{t}Bu, C-$(CH_3)_3$), 34.2(Ar-^{t}Bu, C-$(CH_3)_3$), 31.2(Ar-${}^tBu$, CH_3), 30.9(Ar-${}^tBu$, CH_3). Elemental analysis calculated (%) for [$C_{47}H_{55}Br_2CuN_3$]: C 63.76, H 6.26, N 4.75, found C 64.11, H 6.08, N 4.47. MS: 889.21(8), 888.21(6), 887.21(4), 886.21(2), 885.21(3), 884.21(1), 883.21(7), 882.21(5).

(2F) ZnBr₂-2,6-Bis{1-[(2,5-ditertbutylphenyl)imino]-benzyl}pyridine: $ZnBr_2$ powder (32 mg, 0.142 mmol) was added to a clear yellow solution of **DIMPY** (100 mg, 0.151 mmol) in 8 mL of toluene. The reaction mixture was allowed to stir for 14 hours, gradually becoming opaque yellow. Solution was then held at -20°C overnight, over which time a bright yello precipitate formed. Solution was filtered, washed with 5 x 2 mL hexanes, and allowed to dry under vacuum. A pale bright yellow powder was isolated in 95% yield. Yellow plate-like crystals suitable for X-ray analysis were grown by diffusion of saturated chlorobenzene solution in hexanes, and storing at -20°C for several days. ${}^1H$ NMR ($CDCl_3$, 300 MHz): δ 7.89(br t, 1 H, py, *p*-CH), 7.60(br d , 2 H, py, *m*-CH), 7.40-7.10(br m, 12 H, aromatic), 6.96(br d, 1H, aromatic), 6.93(br d, 1 H, aromatic), 6.53(br d, 2 H, aromatic), 1.49(br s, 18H, ${}^tBu$), 0.96(br s, 18H, ${}^tBu$). ${}^{13}C$ NMR ($CDCl_3$, 75 MHz). δ 165.6(C=N imine), 152.7(py, *o*-C=N), 149.9(Ar-CH), 148.3 (Ar-CH), 138.9(Ar, *i*-C), 138.1(Ar-CH), 134.3(Ar, *i*-C), 129.8(Ar-CH), 129.3(Ar-CH), 128.3(Ar-CH), 126.1(Ar-CH), 125.0 (Ar-CH), 121.9(Ar-${}^tBu$, C-${}^tBu$), 120.7(Ar-${}^tBu$, C-${}^tBu$), 35.5(Ar-${}^tBu$, C-$(CH_3)_3$), 34.2(Ar-${}^tBu$, C-$(CH_3)_3$), 31.2(Ar-${}^tBu$, CH_3), 30.9(Ar-${}^tBu$, CH_3). Elemental analysis calculated (%) for [$C_{47}H_{55}Br_2ZnN_3$]: C 63.63, H 6.25, N 4.74, found C 63.46, H 6.37, N 4.72. MS: 889.21(10), 891.20(8), 890.21(7), 889.20(3), 888.21(4), 887.21(1), 886.21(5), 885.21(2). 884.21(9), 883.21(6).

Infrared spectra were collected from powder samples on a Cary 630 FT- IR. All experiments were conducted under laboratory atmosphere. Values are reported in cm^{-1} and are ranked in order of decreasing intensity. The rank in terms of relative intensity is provided in brackets (1 being the most intense).

2A: 3010(1), 2943(3), 1603(6), 1525(5), 1345(2), 1258(4), 1132(9), 1054(7), 743(8)

2B: 3120(3), 2879(5), 1495(6), 1386(4), 1365(2), 1345(8), 1243(1), 1122(7), 1020(10), 698(9)

2C: 2989(4), 2932(3), 1665(6), 1562(5), 1354(1), 1289(2), 1274(9), 1194(8), 732(7)

2D: 3129(2), 2912(6), 1625(3), 1454(8), 1357(1), 1284(5), 1243(4), 1184(7), 882(9)

2E: 3015(2), 2883(5), 1684(1), 1561(6), 1458(9), 1349(3), 1211(8), 1173(4), 641(7)

2F: 3134(3), 2931(8), 1647(6), 1531(4), 1354(1), 1245(2), 1098(9), 995(5), 654(7)

[2.6] X-Ray crystallographic information: 1st row transition metal bromide complexes with the DIMPY ligand

Table 2.6: Summary of data collection and crystallographic parameters for **2A-2F.**

Compound	2A	2B	2C
Empirical formula	$C_{47}H_{40}Br_2MnN_3$	$C_{47}H_{55}Br_2FeN_3$	$C_{47}H_{58}Br_2CoN_3$
Formula weight	861.58	877.61	883.71
Temperature (K)	100(2)	100(2)	100(2)
λ(Å)	0.71073	0.71073	0.71073
Crystal system	Monoclinic	Monoclinic	Monoclinic
Space group	P2(1)/n	P2(1)/n	P2(1)/n
a (Å)	10.3075(3)	10.1990(2)	10.1944(3)
b (Å)	17.9552(6)	17.8294(4)	17.8757(5)
c (Å)	23.3943(8)	23.3592(5)	23.3736(6)
α (deg)	90.00	90.00	90.00
β (deg)	96.0330(10)	96.0360(10)	95.9590(10)
γ (deg)	90.00	90.00	90.00

V (Å^3)	4305.7(2)	4224.14(15)	4236.4(2)
Z	16	4	4
ρ (calc) (Mg/m^3)	5.316	1.380	1.386
μ (mm^{-1})	8.786	2.284	2.327
Absorption correction	Semi-empirical from equivalents		
Final R indices [I>2σ(I)]			
R1[a]	0.0614	0.0509	0.0758
*w*R2[b]	0.0664	0.0549	0.0536

[a] $R1 = \Sigma \left\| F_o \right| - \left| F_c \right\| / \Sigma \left| F_o \right|$. [b] $wR2 = \left(\Sigma w \left(\left| F_o \right| - \left| F_c \right| \right)^2 / \Sigma w \left| F_o \right|^2 \right)^{1/2}$

Table 2.6 continued

Compound	**2D**	**2E**	**2F**
Empirical formula	$C_{47}H_{55}Br_2NiN_3$	$C_{48.5}H_{58}Br_2Cl_3CuN_3$	$C_{53}H_{60}Br_2ClZnN_3$
Formula weight	880.47	1012.69	999.68
Temperature (K)	200(2)	200(2)	200(2)
λ(Å)	0.71073	0.71073	0.71073
Crystal system	Monoclinic	Monoclinic	Monoclinic
Space group	P2(1)/n	P2(1)/c	P2(1)/n
a (Å)	10.2419(12)	15.461(9)	16.3022(10)
b (Å)	17.972(2)	20.210(6)	20.3682(13)
c (Å)	23.493(3)	17.440(5)	16.9832(11)
α (deg)	90.00	90.00	90.00
β (deg)	95.616(2)	115.478(15)	117.314(4)
γ (deg)	90.00	90.00	90.00
V (Å^3)	4303.5(9)	4919(3)	5010.5(5)
Z	4	4	4

ρ (calc) (Mg/m^3)	1.359	1.367	1.325
μ (mm^{-1})	2.343	2.266	2.175
Absorption correction	Semi-empirical from equivalents		
Final R indices [I>2σ(I)]			
R1[a]	0.0697	0.1363	0.0639
*w*R2[b]	0.0761	0.1059	0.0505

[a] $R1 = \sum \left\| F_o \right| - \left| F_c \right\| / \sum \left| F_o \right|.$ [b] $wR2 = \left(\sum w \left(\left| F_o \right| - \left| F_c \right| \right)^2 / \sum w \left| F_o \right|^2 \right)^{1/2}$

Table 2.7: Selected bond lengths (A) for compounds **2A-2F.**

2A		**2B**		**2C**	
Mn(1)-N(1)	2.254(3)	Fe(1)-N(1)	2.163(2)	Co(1)-N(1)	2.160(2)
Mn(1)-N(3)	2.268(3)	Fe(1)-N(3)	2.170(2)	Co(1)-N(3)	2.054(2)
Mn(1)-N(2)	2.216(3)	Fe(1)-N(2)	2.0690(19)	Co(1)-N(2)	2.054(2)
Mn(1)-Br(1)	2.4647(7)	Fe(1)-Br(1)	2.4670(4)	Co(1)-Br(1)	2.4517(5)
Mn(1)-Br(2)	2.5083(7)	Fe(1)-Br(2)	2.3946(4)	Co(1)-Br(2)	2.3867(5)
N(1)-C(15)	1.285(5)	N(1)-C(21)	1.292(3)	N(1)-C(15)	1.282(3)
N(3)-C(27)	1.284(5)	N(3)-C(27)	1.291(3)	N(3)-C(27)	1.285(3)
N(2)-C(22)	1.340(5)	N(2)-C(22)	1.341(3)	N(2)-C(22)	1.340(3)
N(2)-C(26)	1.352(5)	N(2)-C(26)	1.344(3)	N(2)-C(26)	1.341(3)
C(15)-C(22)	1.502(5)	C(21)-C(22)	1.488(3)	C(15)-C(22)	1.501(4)
C(27)-C(26)	1.504(5)	C(27)-C(26)	1.481(3)	C(27)-C(26)	1.496(4)

Table 2.7 continued

2D		**2E**		**2F**	
Ni(1)-N(1)	2.134(5)	Cu(1)-N(1)	2.120(4)	Zn(1)-N(1)	2.273(4)
Ni(1)-N(3)	2.132(5)	Cu(1)-N(3)	2.228(4)	Zn(1)-N(3)	2.446(4)
Ni(1)-N(2)	1.982(5)	Cu(1)-N(2)	1.935(4)	Zn(1)-N(2)	2.071(4)
Ni(1)-Br(1)	2.4493(10)	Cu(1)-Br(1)	2.3212(9)	Zn(1)-Br(1)	2.3643(8)
Ni(1)-Br(2)	2.3708(11)	Cu(1)-Br(2)	2.5702(10)	Zn(1)-Br(2)	2.3590(9)
N(1)-C(7)	1.282(7)	N(1)-C(15)	1.301(5)	N(1)-C(7)	1.288(6)
N(3)-C(13)	1.292(7)	N(3)-C(27)	1.295(6)	N(3)-C(13)	1.275(6)
N(2)-C(8)	1.342(8)	N(2)-C(22)	1.337(6)	N(2)-C(8)	1.344(6)
N(2)-C(12)	1.355(8)	N(2)-C(26)	1.334(6)	N(2)-C(12)	1.343(6)
C(7)-C(8)	1.500(8)	C(15)-C(22)	1.485(6)	C(7)-C(8)	1.489(7)
C(12)-C(13)	1.508(8)	C(27)-C(26)	1.498(6)	C(12)-C(13)	1.500(7)

Table 2.8: Selected bond angles for compounds **2A-2F.**

2A		**2B**		**2C**	
Mn(1)-N(1)-C(15)	118.7(2)	Fe(1)-N(1)-C(21)	118.85(16)	Co(1)-N(1)-C(15)	116.49(18)
Mn(1)-N(3)-C(27)	120.4(3)	Fe(1)-N(3)-C(27)	116.91(17)	Co(1)-N(3)-C(27)	117.96(18)
Mn(1)-N(2)-C(22)	117.9(2)	Fe(1)-N(2)-C(22)	119.94(15)	Co(1)-N(2)-C(22)	118.33(18)
Mn(1)-N(2)-C(26)	119.0(2)	Fe(1)-N(2)-C(26)	118.68(16)	Co(1)-N(2)-C(26)	119.66(17)
N(1)-C(15)-C(22)	115.2(3)	N(1)-C(21)-C(22)	113.4(2)	N(1)-C(15)-C(22)	114.5(2)
N(3)-C(27)-C(26)	114.3(3)	N(3)-C(27)-C(26)	114.6(2)	N(3)-C(27)-C(26)	113.9(2)
N(1)-Mn(1)-N(2)	71.36(11)	N(1)-Fe(1)-N(2)	73.48(7)	N(1)-Co(1)-N(2)	75.26(8)
N(3)-Mn(1)-N(2)	70.47(11)	N(3)-Fe(1)-N(2)	74.40(7)	N(3)-Co(1)-N(2)	74.26(8)
N(1)-Mn(1)-N(3)	141.18(11)	N(1)-Fe(1)-N(3)	146.95(7)	N(1)-Co(1)-N(3)	148.29(8)
N(1)-Mn(1)-Br(1)	102.27(8)	N(1)-Fe(1)-Br(1)	96.77(5)	N(1)-Co(1)-Br(1)	95.25(6)
N(3)-Mn(1)-Br(1)	100.16(8)	N(3)-Fe(1)-Br(1)	95.13(5)	N(3)-Co(1)-Br(1)	96.85(6)
N(1)-Mn(1)-Br(2)	96.57(8)	N(1)-Fe(1)-Br(2)	99.44(5)	N(1)-Co(1)-Br(2)	100.08(6)
N(3)-Mn(1)-Br(2)	97.57(7)	N(3)-Fe(1)-Br(2)	100.61(5)	N(3)-Co(1)-Br(2)	99.01(6)
N(2)-Mn(1)-Br(1)	136.08(8)	N(2)-Fe(1)-Br(1)	97.94(5)	N(2)-Co(1)-Br(1)	96.84(6)
N(2)-Mn(1)-Br(2)	101.46(8)	N(2)-Fe(1)-Br(2)	141.17(5)	N(2)-Co(1)-Br(2)	143.23(6)
Br(1)-Mn(1)-Br(2)	122.45(3)	Br(1)-Fe(1)-Br(2)	120.880(16)	Br(1)-Co(1)-Br(2)	119.927(18)
C(15)-C(22)-N(2)	114.6(3)	C(21)-C(22)-N(2)	113.3(2)	C(15)-C(22)-N(2)	113.8(2)
C(27)-C(26)-N(2)	114.0(3)	C(27)-C(26)-N(2)	114.0(2)	C(27)-C(26)-N(2)	113.1(2)

Table 2.8 continued

2D		**2E**		**2F**	
Ni(1)-N(1)-C(7)	114.5(4)	Cu(1)-N(1)-C(15)	112.8(3)	Zn(1)-N(1)-C(7)	113.5(3)
Ni(1)-N(3)-C(13)	116.7(4)	Cu(1)-N(3)-C(27)	108.0(3)	Zn(1)-N(3)-C(13)	110.5(3)
Ni(1)-N(2)-C(8)	117.9(4)	Cu(1)-N(2)-C(22)	119.2(3)	Zn(1)-N(2)-C(8)	118.5(3)
Ni(1)-N(2)-C(12)	119.1(4)	Cu(1)-N(2)-C(26)	119.4(3)	Zn(1)-N(2)-C(12)	122.2(3)
N(1)-C(7)-C(8)	114.9(5)	N(1)-C(15)-C(22)	114.7(4)	N(1)-C(7)-C(8)	115.9(5)
N(3)-C(13)-C(12)	113.4(5)	N(3)-C(27)-C(26)	113.5(4)	N(3)-C(13)-C(12)	115.4(5)
N(1)-Ni(1)-N(2)	77.6(2)	N(1)-Cu(1)-N(2)	78.22(15)	N(1)-Zn(1)-N(2)	74.72(16)
N(3)-Ni(1)-N(2)	76.8(2)	N(3)-Cu(1)-N(2)	76.25(15)	N(3)-Zn(1)-N(2)	71.54(16)
N(1)-Ni(1)-N(3)	153.95(19)	N(1)-Cu(1)-N(3)	147.27(14)	N(1)-Zn(1)-N(3)	146.09(16)
N(1)-Ni(1)-Br(1)	92.85(13)	N(1)-Cu(1)-Br(1)	100.28(10)	N(1)-Zn(1)-Br(1)	102.93(11)
N(3)-Ni(1)-Br(1)	94.39(13)	N(3)-Cu(1)-Br(1)	100.66(10)	N(3)-Zn(1)-Br(1)	96.93(10)
N(1)-Ni(1)-Br(2)	99.46(14)	N(1)-Cu(1)-Br(2)	104.68(11)	N(1)-Zn(1)-Br(2)	99.63(11)
N(3)-Ni(1)-Br(2)	98.58(14)	N(3)-Cu(1)-Br(2)	95.24(11)	N(3)-Zn(1)-Br(2)	97.18(11)
N(2)-Ni(1)-Br(1)	95.26(14)	N(2)-Cu(1)-Br(1)	168.51(12)	N(2)-Zn(1)-Br(1)	120.58(11)
N(2)-Ni(1)-Br(2)	145.07(14)	N(2)-Cu(1)-Br(2)	89.42(12)	N(2)-Zn(1)-Br(2)	125.53(11)
Br(1)-Ni(1)-Br(2)	119.66(4)	Br(1)-Cu(1)-Br(2)	101.94(3)	Br(1)-Zn(1)-Br(2)	113.54(3)
C(7)-C(8)-N(2)	113.9(5)	C(15)-C(22)-N(2)	113.2(4)	C(7)-C(8)-N(2)	115.9(5)
C(13)-C(12)-N(2)	113.2(5)	C(27)-C(26)-N(2)	113.5(4)	C(13)-C(12)-N(2)	115.9(5)

Chapter 3: The S,N,S ligands – 2,6-bis(methylthiomethyl) pyridine and 2,6-bis(ethylthiomethyl) pyridine

[3.1] Introduction

Previous work by the Richeson group has involved the study of the magnetic properties of Co(II) complexes supported by SNS and DIMPY ligands.[17] This work formed the basis of this research involving the probing of complexes of 1st row transition metal bromides with the S, N, S ligand scaffolds. The two specific SNS ligands employed in this research are shown in Figure 3.1 along with the basic S,N,S scaffold. The two specific ligands are the 2,6-bis(methylthiomethyl) ligand, **3A** or **SNS1**, and the 2,6-bis(ethylthiomethyl) ligand, **3B** or **SNS2**.

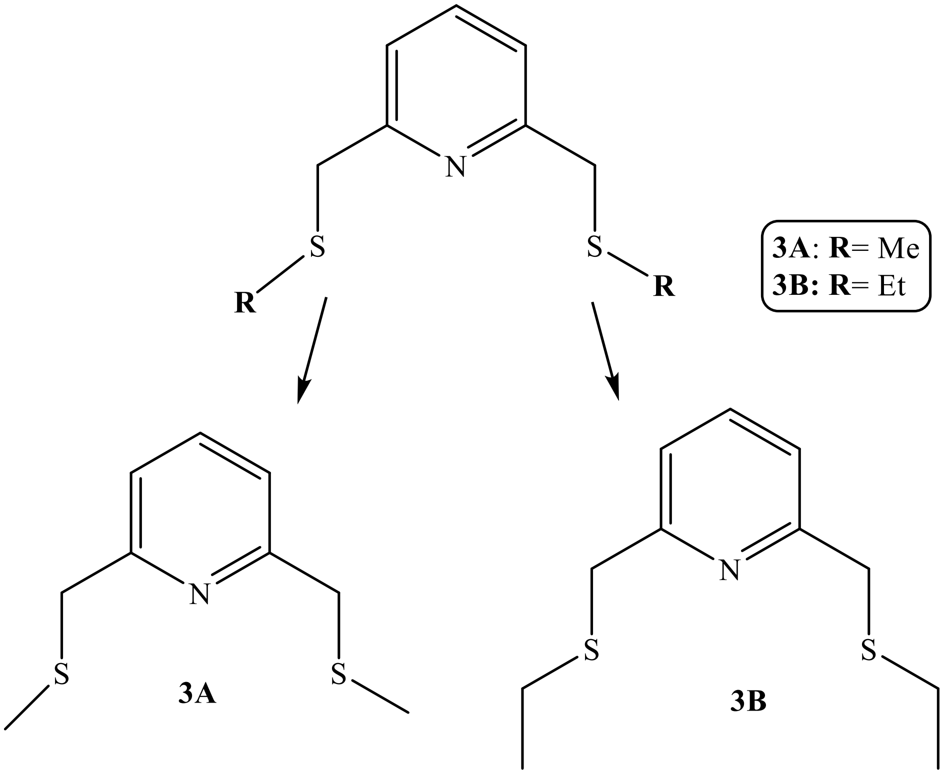

Figure 3.1: The general structure of the SNS ligand along with ligands **3A, SNS1,** and **3B, SNS2**.

[3.1.2] Uses and history of SNS ligand

The SNS ligand is a tridentate pincer ligand with two sulfur and one nitrogen donor atom. In the past, these ligands have been popularized due to their ability to act as enzyme model structures. This is due to the fact that histidine and cysteine residues in polypeptide chains contain nitrogen and sulfur donor atoms, respectively; thus, the SNS ligand effectively mimics these side chains in research when studying metalloenzymes. A specific example is the study of liver alcohol dehydrogenase (LADH), which is a zinc metalloenzyme.[35] The resting enzyme has a zinc(II) metal center which is pseudo-tetrahedrally bound to one N-histidine side chain and two S-cysteine side chain along with one labile water molecule. Due to this arrangement of donors, the SNS ligand is an ideal model structure for the reactivity of the zinc site of the metalloenzyme.

Furthermore, the use of tridentate pincer ligands provides several advantages over monodentate ligands. To begin with, tridentate pincer ligands inhibit dimerization, which has been proven to impede catalytic activity. Secondly, the structural and electronic properties of tridentate ligands can be strategically effected by the use of varying materials in synthesis.[36] Lastly, metallation of tridentate ligands is favored due to a less negative delta entropy of formation in comparison to monodentate ligands.[37] This allows for added stability of the metal complexes. All of these properties provide for stable metal complexes whose structural, electronic and catalytic properties can be extensively studied.

---

[35] A. Meibner, W. Haehnel, H. Vahnrenkamp, *Chem. Eur. J*, **1997**, 3, 261-267.

[36] M. Albrecht, G. Van Koten, *Angew. Chem. Int. Ed.,* **2001**, 40, 3750-3781.

[37] A.T. Normand, K.J. Cavell, Eur. J. Inorg. Chem., 2008, 2781-2800.

[3.2] Ligand synthesis and properties

The bis(methylthiomethyl) pyridine was synthesized in a two-step process according to published procedures. The first step involves the reaction of thionyl chloride with 2,6-pyridinemethanol at 0°C to yield the bis(chloromethyl) pyridine compound isolated by recrystallization from light petroleum ether.[38] The second step was the reaction of the bis(chloromethyl) pyridine product with sodium methanethiolate in DMF to yield a crude product which is purified by column chromatography.[39] The bis(ethylthiomethyl) pyridine ligand was synthesized similarly using ethanethiole. The synthesis is outlined in Figure 3.2. The identities of both compounds were confirmed using NMR and elemental analysis and were in agreement with published spectral data.

---

[38] W. Baker, K.M. Buggle, F.W. McOmie, D.A.M. Watkin, *J. Am. Chem. Soc*. **1958**, 0, 3594.

[39] L. Canovese, G. Chessa, G. Marangoni, B. Pitteri, P. Uguagliati, F. Visentin, *Inorg. Chim. Acta*, **1991**, 186, 79.

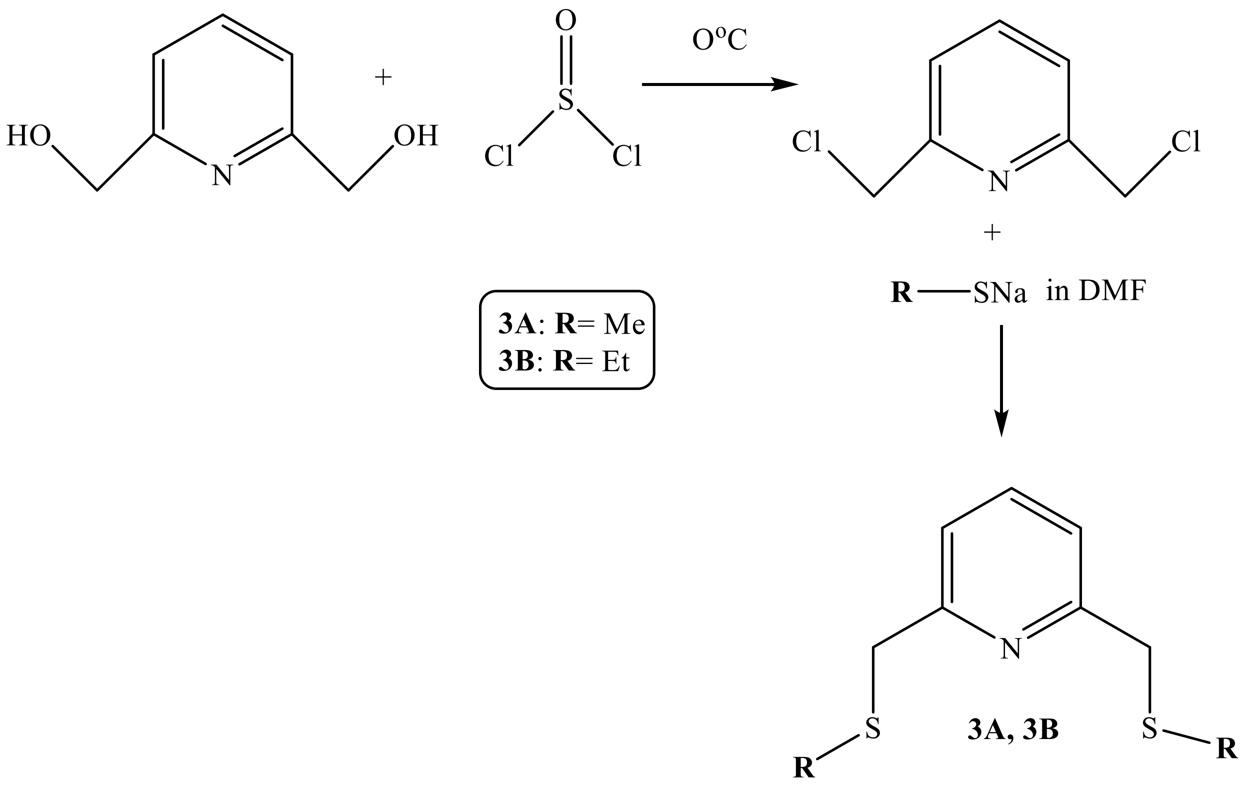

Figure 3.2: Synthesis of SNS ligands **3A** and **3B**.

[3.3] Experimental: Synthesis and characterization of SNS ligands

(3A) **SNS1** ***2,6-bis(methylthiomethyl)pyridine***: Into an ice-cooled solution of 2,6-bis(chloromethyl)pyridine (3.52g, 20 mmol) in DMF was added NaSMe(3.1g, 44mmol) and the mixture was allowed to warm to room temperature. After 24 hours of stirring, the solvent was evaporated and the resulting residue partitioned between chloroform and water. The organic phase was washed with water, dried with sodium sulfate and evaporated to dryness to give an oily product. Chromatography of this residue over silica gel eluted with chloroform yielded 3.18g (80%) as oil. ^{1}H NMR ($CDCl_3$, 300MHz): δ 7.64 (t, 1H) 7.23 (d, 2H), 3.78 (s, 4H, CH_2-py), 2.05 (s, 6H, CH_3). ^{13}C NMR ($CDCl_3$, 75 MHz). δ 158 (Ar-C), 137(Ar-CH), 122(Ar-CH), 40(Ar-CH_2-S), 15(S-CH_3). Elemental analysis calculated (%) for [$C_{11}H_{17}NS_2$]: C 58.10, H 7.54, N 6.15, found C 58.09, H 7.52, N 6.13.

(3B) **SNS2-** ***2,6-bis(ethylthiomethyl)pyridine***: NaMeO (37.7mmol) in methanol was stirred for 15 minutes with ethanethiol (37.7mmol, 2.8mL) This solution was then added to a solution of 2,60-bis(chloromethyl)pyridine (18.9mol, 5g) in 50mL methanol. After 2 hours under reflux, the solvent was extracted twice with diethyl ether (150mL) and the white solid was discarded. The extract was washed twice with an aqueous solution of Na2CO3 and then twice with water, dried and evaporated under vacuum to yield 3.24g (83%) as oil. ^{1}H NMR ($CDCl_3$, 300MHz): δ 7.66 (t, 1H) 7.02 (dd, 2H), 3.9 (s, 4H, CH_2-py), 2.40 (q, 4H, S-CH_2), 0.977(t, 6H, CH_3) . ^{13}C NMR ($CDCl_3$, 75 MHz). δ 154 (Ar-C), 133(Ar-CH), 120(Ar-CH), 40(Ar-CH_2-S), 22(S-CH_2), 14(S-CH_3). Elemental analysis calculated (%) for [$C_{13}H_{21}NS_2$]: C 61.13, H 8.29, N 5.48, found C 61.11, H 8.26, N 5.47.

Infrared spectra were collected from powder samples on a Cary 630 FT- IR. All experiments were conducted under laboratory atmosphere. Values are reported in cm^{-1} and are ranked in order of decreasing intensity. The rank in terms of relative intensity is provided in brackets (1 being the most intense).

SNS: 3021(10), 3034(4), 3012(9), 2998(5), 1621(2), 1599(1), 1483(6), 1139(14), 1048(8), 1034(11), 976(12), 876(3), 623(7)

SNS2: 3105(7), 3011(4), 2885(10), 1681(13), 1643(11), 1587(2), 1584(1), 1543(5), 1489(3), 1476(9), 1123(6), 1056(12), 1023(8), 865(14), 675(15)

Chapter 4: Complexes of 1st row transition metal bromides with S,N,S ligands

[4.1] Introduction

Similarly to DIMPY ligands, the chemistry of S,N,S-type ligands has been studied with a wide variety of metal ions.[40] For instance, work by the Berry group from Williamsburg looked at group 12 metal complexes with a tridentate S,N,S ligand identical to the SNS1 ligand, **3A,** used in this work. In addition, the Koh group from Singapore employed an S,N,S ligand in the investigation of copper complexes. Finally, most recently, the Kataoka group from Japan investigated the chemistry of Palladium complexes with an S,N,S ligand scaffold. As outlined in chapter 2, previous work by the Richeson group has revealed single molecule magnet behaviour in a complex of cobalt(II) bromide and the SNS1 ligand. This work was the basis for the further exploration of complexes of 1st row transition metal bromides with S,N,S ligands; particularly SNS1 and SNS2.

The following chapter will be analogous to Chapter 2; however, in this chapter, trends in the structure, bonding, magnetic and electronic properties of transition metal bromides with the S,N,S-type ligands outlined in Chapter 3, will be analyzed. An outline of the synthetic strategy is presented in Figure 4.1.

---

[40] (a)S.Q. Bai, L.L. Koh, T.S. Hor, *Inorg. Chem.,* **2002**, 48 (3), 1207-1213. (b)W. Lai, S.M. Berry, R.J. Butcher, *Inorg. Chem.*, **2006**, 45 (2), 571-581. (c)T.S. Hor, *Inorg. Chem*., **2009**, 3, 11. (d)Y. Kawada, Y. Kataoka, Y. Ura, *Dalton Trans.*, **2013**, DOI: 10.1039/C3DT51592C.

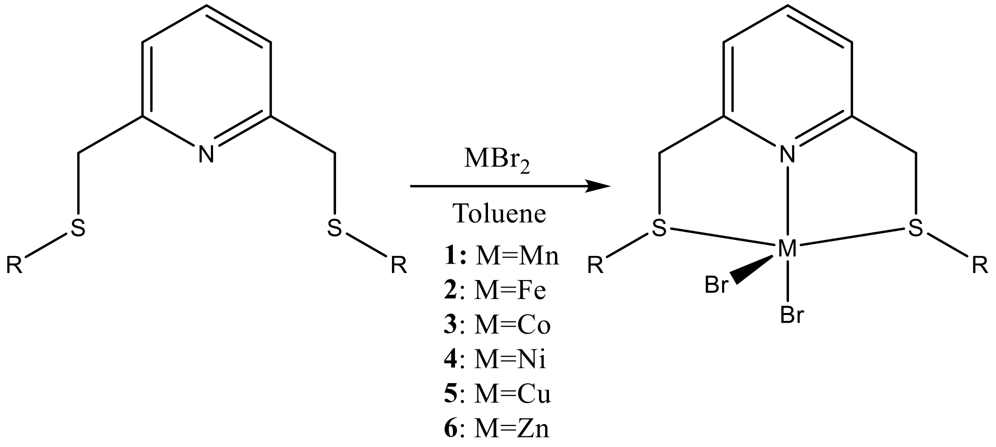

Figure 4.1: Schematic representation of reaction scheme (R= Me, Et).

[4.2] Results and discussion: Ligation of 2,6-bis(methylthiomethyl) and 2,6-bis(ethylthiomethyl) pyridine to first row transition metal bromides

The synthetic preparation of the transition metal bromide-SNS/SNS2 complexes was quite straight forward and analogous to that outlined for the transition metal bromide-DIMPY complexes. The metals were added to solutions of SNS and SNS2 ligand in toluene. The resulting solutions were stirred overnight to provide optimal yields (an average of 88% for SNS and 92% for SNS2) after which significant colour changes were observed. The solutions were held at -20^{o}C overnight to facilitate precipitation of the product. The solutions were then filtered and washed with hexanes to remove any impurities. The crystal structures obtained for the SNS1 ligand are outlined in Figure 4.2 and SNS2 in Figure 4.3. The crystal data, bond lengths and bond angles are summarized in Tables 4.8 through 4.10.

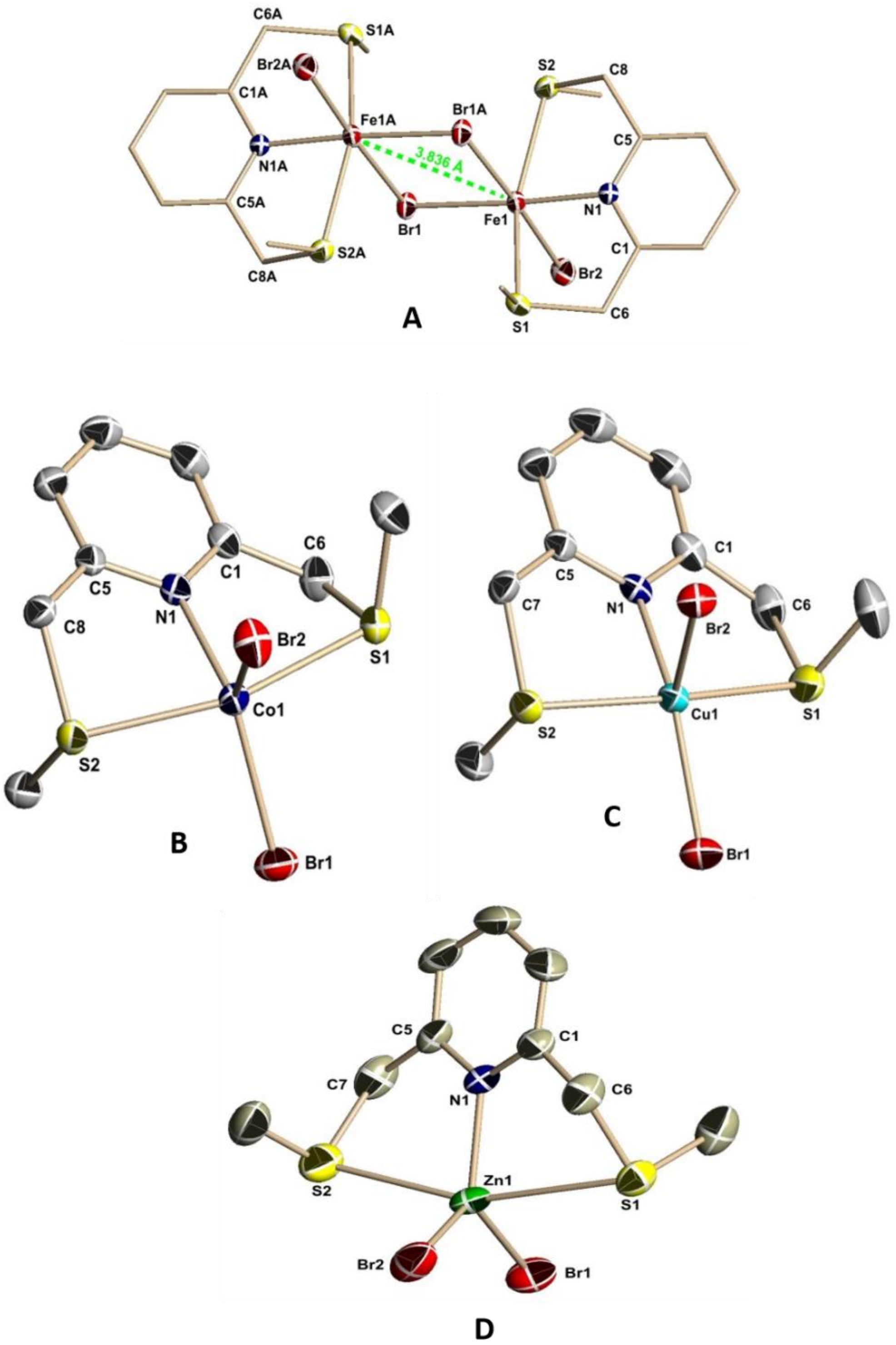

Figure 4.2: X-ray crystallographic structures of first row transition metal bromides with SNS1 ligand. Hydrogens and solvents omitted for clarity.

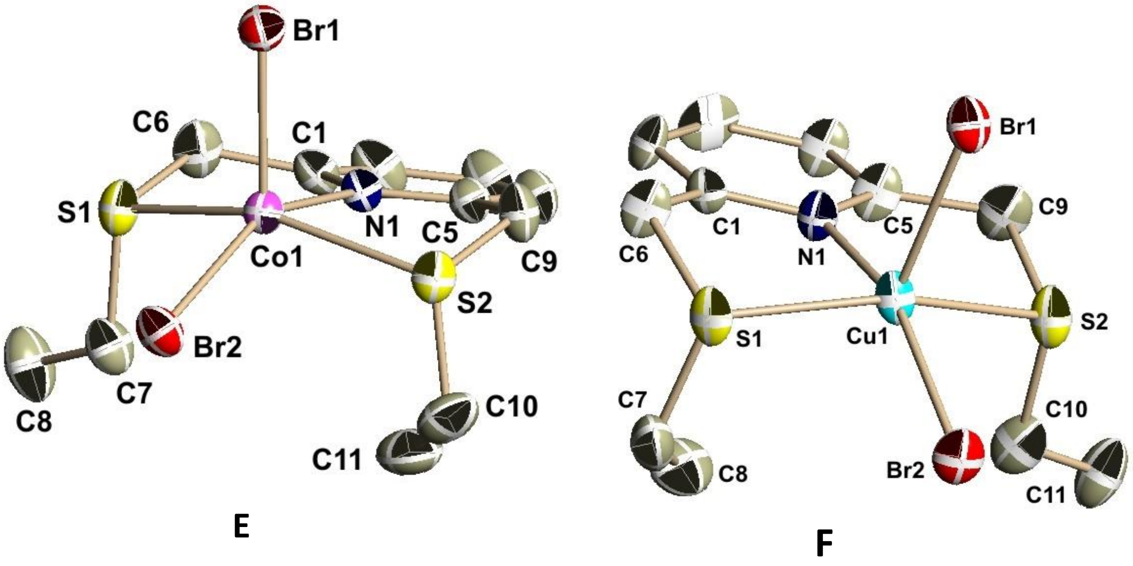

Figure 4.3: X-ray crystallographic structures of first row transition metal bromides with SNS2 ligand. Hydrogens and solvents omitted for clarity.

[4.2.2] Analysis of structure geometries and distortions

The X-ray structures determined for the compounds reported in Figure 4.2 and 4.3 reveal neutral mononuclear complexes in which the central metal retains an oxidation state of +2. The SNS nitrogen and sulfur atoms are bound to the metal ion in all cases. Structure **4A** is a dimer containing two Fe centers and two SNS ligands. Also, in all structures, the bromides remain bound, resulting in coordination number of 5.

Using the calculations for the τ parameter outlined in Chapter 2, τ parameters were calculated for complexes **4A** through **4F** and are exhibited in Table 4.1.

Table 4.1: Calculated τ parameters for X-ray structures **A-F**.

	4A	**4B**	**4C**	**4D**	**4E**	**4F**
α	176.64	133.28	159.74	122.58	149.05	157.13
β	119.60	120.66	119.51	121.6	122.03	121.8
τ	**1.00**	**0.21**	**0.67**	**0.016**	**0.45**	**0.59**

From these values, it was determined that most of the complexes exhibited in Figure 4.2 and 4.3 adopted highly distorted 5 coordinate geometries with the exception of dimer **4A** which adopted a classic *tbp* geometry with a τ parameter of 1. In addition, structures **4C**, **4E** and **4F** adopted distorted geometries between *tbp* and *sp*, i.e. a hybrid geometry of the two as their τ parameter values are close to 0.5. **4D**, on the other hand, adopted a geometry closest to *sp* geometry while **4B** adopted a distorted *sp* geometry. In the case of the *tbp* complexes, the basal plane is formed by the two sulfur and one nitrogen donors of the SNS ligand. In the case of the *sp* complexes, the basal plane is formed by the two sulfur and one nitrogen donors of the SNS ligand and one of the bromides.

[4.2.3] Analysis of important bond lengths trends within the 1st row

The general schematic of the bonding of the SNS ligand to the metal centre is depicted in Figure 4.4.

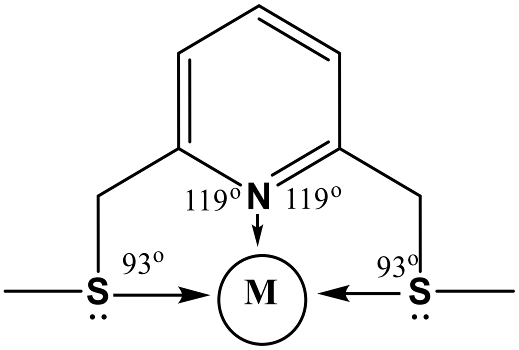

Figure 4.4: General schematic of nitrogen-metal and sulfur-metal bonding from SNS ligand to metal center in structures **4A-4F** including average bond angles.

When looking at this figure, one notices that it is quite different than that shown for the DIMPY ligand in Figure 2.4. This is due to the fact that the sulfur centre in the SNS ligand has two lone pairs and is sp^3 hybridized. Consequently, the closest lone pair available for coordination with the metal centre is located at approximately 90° from the sulfur-carbon bond. In the DIMPY, however, the N_{imine} is sp^2 hybridized, therefore, the lone pair available for coordination with the metal centre is at approximately 114° from the C=N bond.

In addition, one would expect a marked increase in size of the M-S bonds compared to the $M-N_{imine}$ bonds. This is due to the fact that the sulfur centre is markedly larger than nitrogen as well as softer and less electronegative. Consequently, it is expected that there is less overlap with the orbitals of the metal, resulting in a longer bond. Indeed, this is the case for the complexes in Table 4.2. Finally, there is no real trend seen with the M-Br bond lengths as they are quite similar and vary depending on the metal centre. This was also the case with the DIMPY complexes; thus, this can be seen as a trend in itself.

In addition, the experimental metal-ligand bond lengths across the periodic row of transition metals was analyzed in order to elucidate any trends. The experimental bond lengths are listed in Table 4.2 and depicted graphically in Figure 4.5.

Table 4.2: Experimental bond lengths for X-ray structures **4B-4F.**

	4A	**4B**	**4C**	**4D**	**4E**	**4F**
M-N$_{pv}$	**2.1811(19)**	**2.065(2)**	**2.014(2)**	**2.092(3)**	**2.1172(16)**	**2.016(9)**
M-S$_{(1)}$	2.5196(7)	2.4945(6)	2.3297(8)	2.3635(6)	2.4461(6)	2.321(3)
M-S$_{(2)}$	2.5669(4)	2.5028(6)	2.3380(9)	2.3690(6)	2.4502(6)	2.344(3)
M-S$_{(AVG)}$	**2.543**	**2.499**	**2.334**	**2.366**	**2.448**	**2.332**
M-Br$_1$	2.5720(4)	2.3987(4)	2.3832(5)	2.5573(10)	2.4212(4)	2.4053(17)
M-Br$_2$	2.7104(4)	2.4100(4)	2.6741(5)	2.7514(10)	2.4349(4)	2.5467(18)
M-Br$_{(AVG)}$	**2.614**	**2.404**	**2.529**	**2.654**	**2.428**	**2.47**

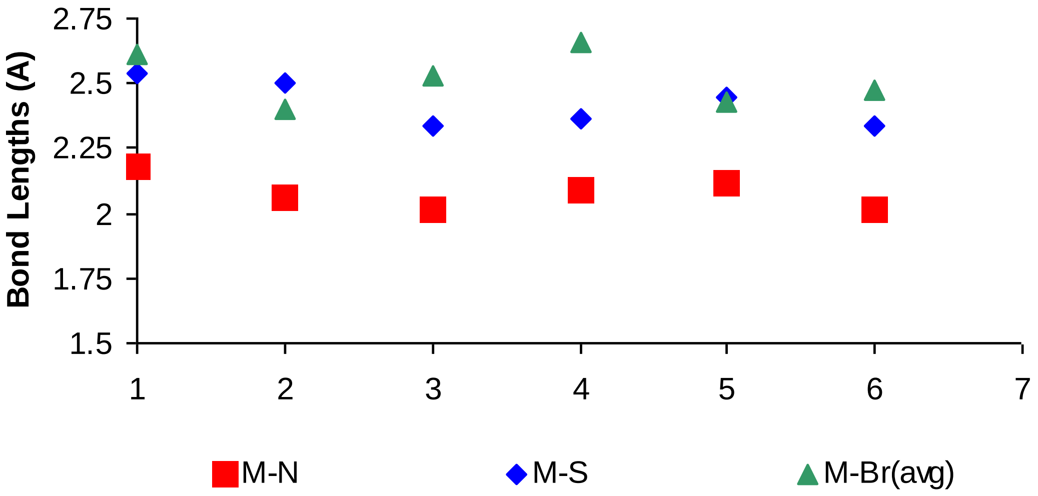

Figure 4.5: Graphic representation of metal-nitrogen, *M-N*, metal-sulfur, *M-S*, and metal-bromide (*M-Br*$_{avg}$) bond lengths in X-ray structures **4A-4F**.

Similarly to the data seen in Chapter 2, there is a general trend in M-N and M-S bond lengths as one moves across the row. In this case, there is no data for Mn or Ni; therefore the trend is not as pronounced; however, one can still see a decrease in bond lengths from structure **4A** through **4C** and then an increase in **4D**. The corresponding decrease is also seen in the SNS2 structures with a decrease in bond lengths in structure **4E** and **4F**. The reasoning behind this trend is analogous to that explained in Chapter 2 (*2.2.3*).

[4.2.4] Analysis of magnetic properties

As mentioned in Chapter 2, it is assumed using crystal field theory and the spectrochemical series that complexes of transition metal bromides with the SNS ligand will yield high spin complexes due to the fact that the two sulfur atoms of the ligand provide relatively weak field splitting. This hypothesis is further cemented from previous research by the Richeson group in which a $CoBr_2$ complex with SNS proved to be high spin.[17]

The theoretical and experimental values for the effective magnetic moment, μeff, and the number of unpaired electrons are shown in Table 4.3 for the various paramagnetic transition metal bromides-SNS complexes. The theoretical values (μeff, *theor*) were calculated using the spin-only formula, theoretical number of unpaired electrons for the high spin paramagnetic species and their respective geometries. The experimental values (μeff, *exp*) were calculated using Evan's method which was discussed in chapter 3. Included in the table are the experimentally observed (μeff, *obs*) values for the metal ions.[41]

---

[41] G.L. Miessler, P.J. Fischer, D.A. Tarr, *Inorganic Chemistry*, Fifth Edition, Prentice Hall, USA, **2013**, 476.

Table 4.3: Theoretical and experimental effective magnetic moment, μeff, values for paramagnetic species of transition metal-bromide-SNS1/SNS2 complexes.

Compound	μ_{eff}, ***theor***	μ***eff, obs***	μ***eff exp***
$MnBr_2$-SNS	5.92	5.7-6.0	5.74
$FeBr_2$-SNS	4.90	5.0-5.6	3.99
$CoBr_2$-SNS	3.87	4.3-5.2	4.68
$NiBr_2$-SNS	2.83	2.9-3.9	3.09
$CuBr_2$-SNS	1.73	1.9-2.1	2.01
$CoBr_2$-SNS2	3.87	4.3-5.2	4.53
$CuBr_2$-SNS2	1.73	1.9-2.1	1.99

As can be seen in Table 4.3, most of the experimentally calculated values are quite close to those predicted theoretically. The small deviations in values are likely due to small impurities (which are expected); however, they all correlate with the observed values noted in literature. The only significant outliers from theoretical values are those involving the $CoBr_2$ complexes. The value for the $CoBr_2$-SNS complex is in line with that calculated previously by the Richeson group using the SQUID magnetometer[42]. The SQUID measurements produced a room temperature susceptibility, X_T, of 2.63 cm^3K/mol, which corresponds to 3.7 unpaired electrons on

---

[42] T. Jurca, A. Farghal, P-H Lin, I. Korobkov, M. Murugesu, D.S. Richeson, *J. Am. Chem. Soc.,* **2011**, *133* (4), 15814-15817.

the metal center. This value is quite close to that calculated using Evans Method. The room temperature susceptibility calculated is high compared to that predicted by the spin-only formula, which would correspond to a Xt value of 1.88cm^{3}K/mol for a S=3/2 metal center; however, it lies within the range of 2.1-3.4 cm^{3}K/mol for highly anisotropic Co(II) ions. Furthermore, the experimentally high value has been shown to be indicative of a high degree of spin-orbit coupling as deviations from the spin-only formula often indicate spin-orbit coupling.[43]

In addition, another value that must be discussed is that for the Fe dimer. The experimental value was found to be smaller than that expected for isolated high-spin mononuclear Fe(II) complexes. The experimental value, however, is in accordance with that shown for Fe(II) dimers bridged by halides in previous research.[44] This is due to interactions between the two Fe centers in the dimer, which result in antiferromagnetic interactions and lowering of the μeff value.

[4.3] Computational analysis: Bond Lengths, Bond Angles and Electronic Absorption

Computational analysis was completed in collaboration with Dr. Serge Gorelsky in order to extensively probe the electronic features of the structures in Figure 4.3. This was obtained through DFT computational study using the B3LYP functional and mixed DZVP/TZVP basis set.

---

[43] (a) J.I. Hoppe, *J. Chem. Educ.*, **1972**, 49 (7), 505. (b) R. Singh, *Inorganic Chemistry*, First Edition, Rai for Mittal Publications, India, **2002**, 25-36.

[44] (a) Z. Moatazedi, M.J. Katz, D.B. Leznoff, *Dalton Trans.*, **2010**, 39, 9889-9896. (b) G. Mund, D.Vidovic, R.J. Batchelor, J.F. Britten, R.D. Sharma, C.H.W. Jones, D.B. Leznoff, *Chem. Eur. J.*, **2003**, 9, 4757.

[4.3.1] Bond lengths and bond angles

When attempting to elucidate the optimized structures for complexes **4A-4F**, it was determined that there were three isomers close in energy for the different complexes. These are shown in Figure 4.7. The only difference in the isomers is the orientation of the methyl groups on sulfur and the M-Br orientation. The key point to be taken from this figure is that crystal packing forces make one of the possible isomers appear in one case, while a different isomer appears in another. These conformers are not all the same computationally. In some cases, a particular configuration is favored over another.

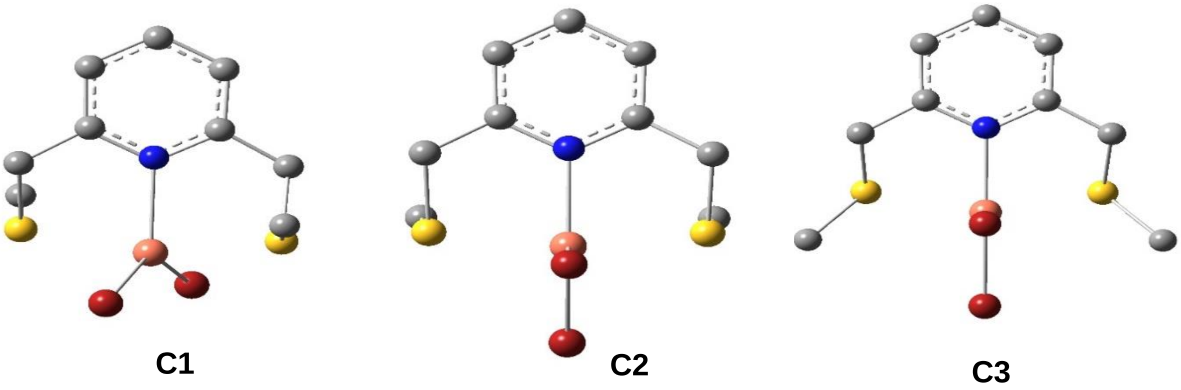

Figure 4.6: Three different isomers of the metal bromide-SNS complexes.

In addition, Table 4.4 shows the computed bond lengths for the metal-sulfur, *M-S*, metal-Npy, *M-Npy*, and metal-bromide, *M-Br*, bonds for C1 conformers. An analogous table will be shown for C2 afterwards, proving that the two conformers are quite similar computationally, but not identical. The general trends, however, remain the same.

Table 4.4: Computed metal-nitrogen, *M-N*, metal-sulfur, *M-S*, and average metal-bromide, $M\text{-}Br_{avg}$, bond lengths in complexes of transition metal bromides Mn through Zn with SNS adopting C1 configurations.

	Mn	Fe	Co	Ni	Cu	Zn
M-N	2.295	2.211	2.106	2.062	2.184	2.179

M-S	2.71	2.611	2.59	2.51	2.451	2.69
M-Br	2.517	2.491	2.448	2.474	2.481	2.430

The bond lengths correlate very well with those determined experimentally, which are shown in Table 4.2.

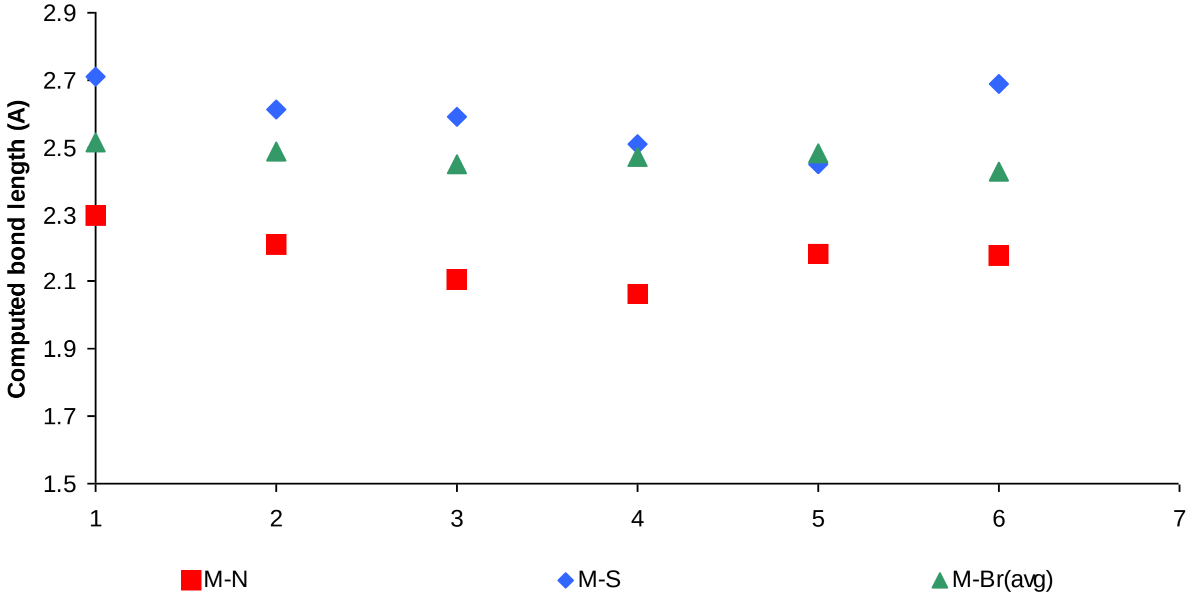

Figure 4.7: Graphic representation of computed M-N, M-S, and M-Br$_{avg}$ bond lengths in complexes of transition metal bromides Mn through Zn with SNS adopting C1 configurations.

Furthermore, it can be seen that an identical trend is seen in the bond lengths of the computed data across the row of transition metals as in the experimental data, which is shown in Figure 4.4. This corroborates that the trend does, in fact, exist and is not simply a random concurrence.

Table 4.5 shows identical data as that in Table 4.4; however, in this case, the data was computed for the coordination complexes adopting C2 configurations. Again, the data corroborates with that seen experimentally.

Table 4.5: Computed metal-nitrogen, *M-N*, metal-sulfur, *M-S*, and metal-bromide, *M-Br*, bond lengths in complexes of transition metal bromides Mn through Zn with SNS1 adopting C2 configurations (ax=axial).

	Mn	Fe	Co	Ni	Cu	Zn
M-N	2.36	2.264	2.27	2.119	2.124	2.272
M-S	2.67	2.581	2.507	2.459	2.413	2.62
M-Brax	2.511	2.446	2.470	2.478	2.582	2.431
M-Br	2.552	2.552	2.489	2.490	2.478	2.479

Furthermore, an analogous figure to that seen in Figure 4.7 is plotted in Figure 4.8.

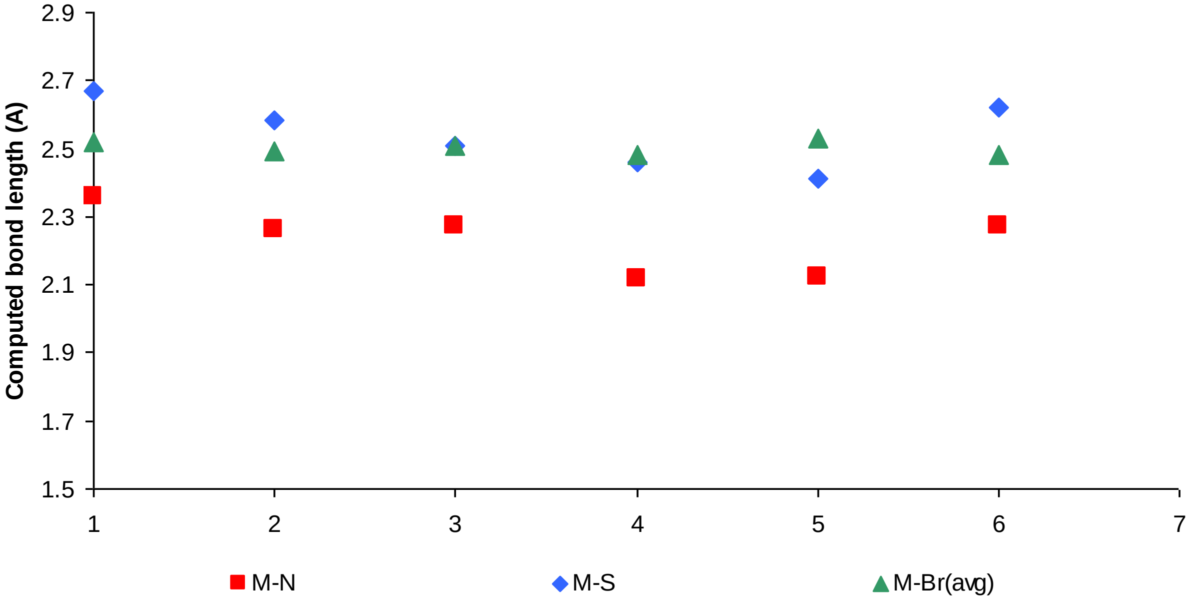

Figure 4.8: Graphic representation of computed M-N, M-S, and M-Br_{avg} bond lengths in complexes of transition metal bromides Mn through Zn with SNS adopting C2 configurations.

In this Figure, it is again evident that there is a similar trend in bond lengths to that seen earlier; further corroborating its existence in experimental conditions. Additionally, similar to that done in chapter 2, further computations were undertaken in order to determine the Mayer bond order by means of B3LYP with TZVP using PCM model (CH_2Cl_2).

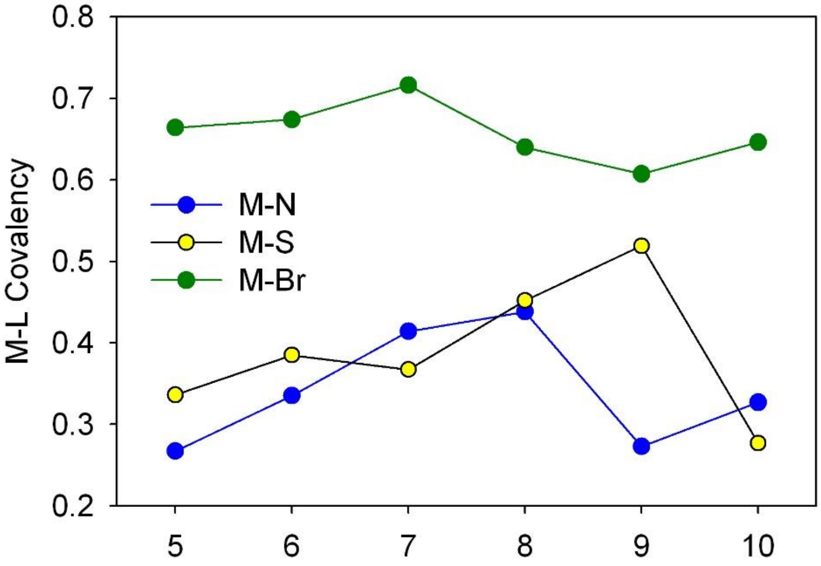

Figure 4.9: Computer Mayer Bond order for transition metal (Mn through Zn) bromide-SNS complexes.

Figure 4.9 shows that as one moves across the periodic table within the transition metal centers studied, there is an increase in covalency until between nickel and copper after which one sees a decrease between copper and zinc. Interestly, this would correlate to longer bond lengths in complexes where there is a smaller bond order and vice versa. In addition, if one were to map the trend in bond length according to this data, it would look like the inverse of that in Figure 4.9 which is analogous to that seen in the experimental bond lengths in Figure 4.4. Lastly, the covalency in the M-Br bonds is higher than that for the M-S and M-N bonds due to their ionic nature.

[4.3.3] Electronic absorption

Analogously to the computations done in Chapter 2, computations were run to elucidate the electronic spectra for the structures synthesized. Figure 4.10 shows the experimental data obtained for the different coordination complexes of transition metal bromides with SNS1 and SNS2.

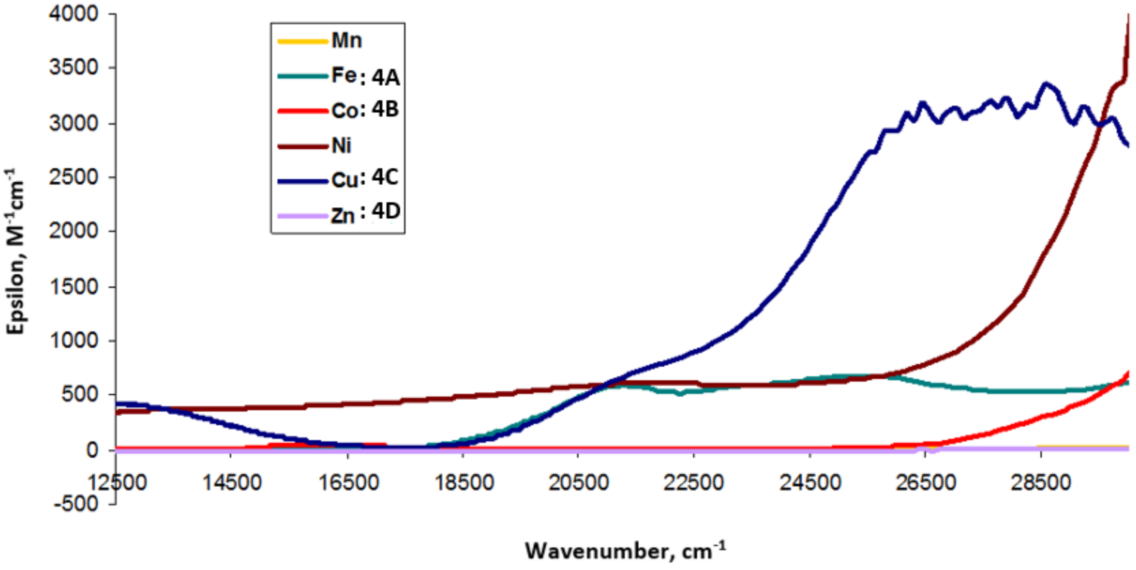

Figure 4.10: Eperimental electronic absorption data for structures **4A** through **4D** as well as the $MnBr_2$ and $NiBr_2$-SNS complexes.

Table 4.6 shows the wavenumber values corresponding to the peaks in the experimental electronic absorption maxima.

Table 4.6: Peaks in wavenumbers, cm^{-1}, of experimental electronic absorption data for structures **4A** through **4D** as well as the $MnBr_2$ and $NiBr_2$-SNS complexes.

Mn	4A	4B	Ni	4C	4D
--	--	--	28,756.40	25, 234.18	--
--	25,478.21	16,248.21	19,582.30	21,285.32	--

--	21,223.39	--	13,908.21	13,475.25	--

The spectra in Figure 4.10 vary for all of the different metal centers, which is expected. Beginning with the $MnBr_2$-SNS complex, it is not surprising that there are few to no peaks as the metal center has a d5 valence electron configuration and the complex is colorless. Moving on to **4A**, which is the peach coloured iron dimer, two peaks are observed in the 21,000cm^{-1} region and the 25,000cm^{-1} region. In the cobalt complex **4B**, which was blue colored, there is a peak in the region of 16,000cm^{-1} which is red shifted in comparison to **4A**. In addition, the $NiBr_2$-SNS complex was green and poorly soluble, leading to absorption spectra that are not consistent; however, one observes peaks that are red shifted in comparison to **4A**. Similar data is seen for the copper complex, **4C**, which was also green in color; however, the peaks are significantly larger. Lastly, complex **4D**, which is the colorless Zn complex, little to no absorption is seen. This is due to the fact that the metal center has a d^{10} valence electron configuration.

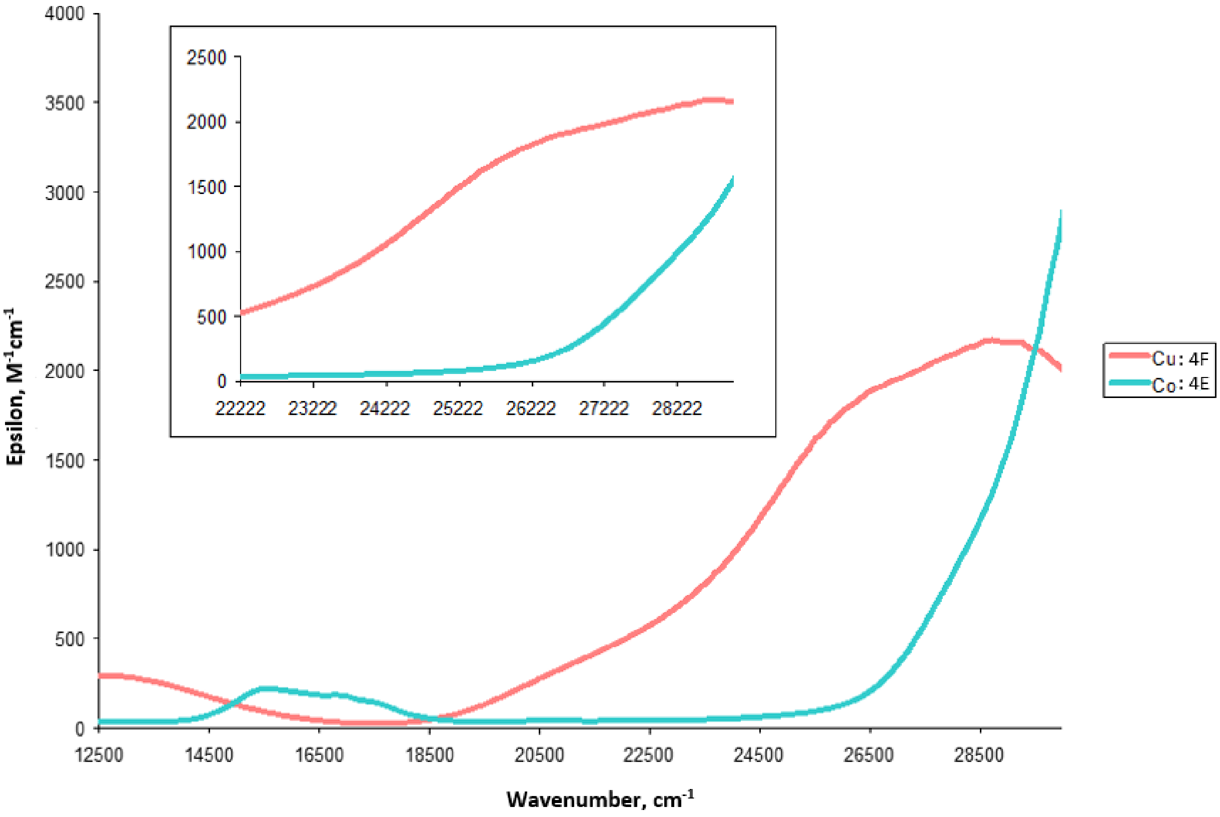

Figure 4.11: Experimental electronic absorption data for structures **4E** and **4F**.

Table 4.7 shows the wavenumber values corresponding to the peaks in the experimental electronic absorptions for complexes **4E** and **4F** which contain the SNS2 ligand scaffold.

Table 4.7: Peaks in wavenumbers, cm^{-1}, of experimental electronic absorption data for structures **4E** and **4F.**

4E	**4F**
--	27,321.45
16,521.32	13,208.45

Interestingly, the absorption maximum for complex **4E**, which is the $CoBr_2$-SNS2 complex, is almost identical to that seen for the complex with SNS. In addition, they are also identical in colour. This is expected as the ligands only slightly vary. Similarly, complex **4F** containing the copper metal center is the same color as complex **4C** and has comparable absorption maxima; however they are red shifted in comparison to **4C**.

In addition, Figure 4.12 contains graphics that superimpose the experimental and computed data. It should be noted that the absorption spectra were not computed for the $FeBr_2$-SNS complex as it was a dimer. Also, for the complexes of $CoBr_2$-SNS and $CuBr_2$-SNS, the absorption spectra were computed for the two isomeric structures of the complexes C1 and C2 as they were quite close in energy while for the other metal centers, only the C1 isomer of the complexes was considered as they was significantly higher in energy than C2.

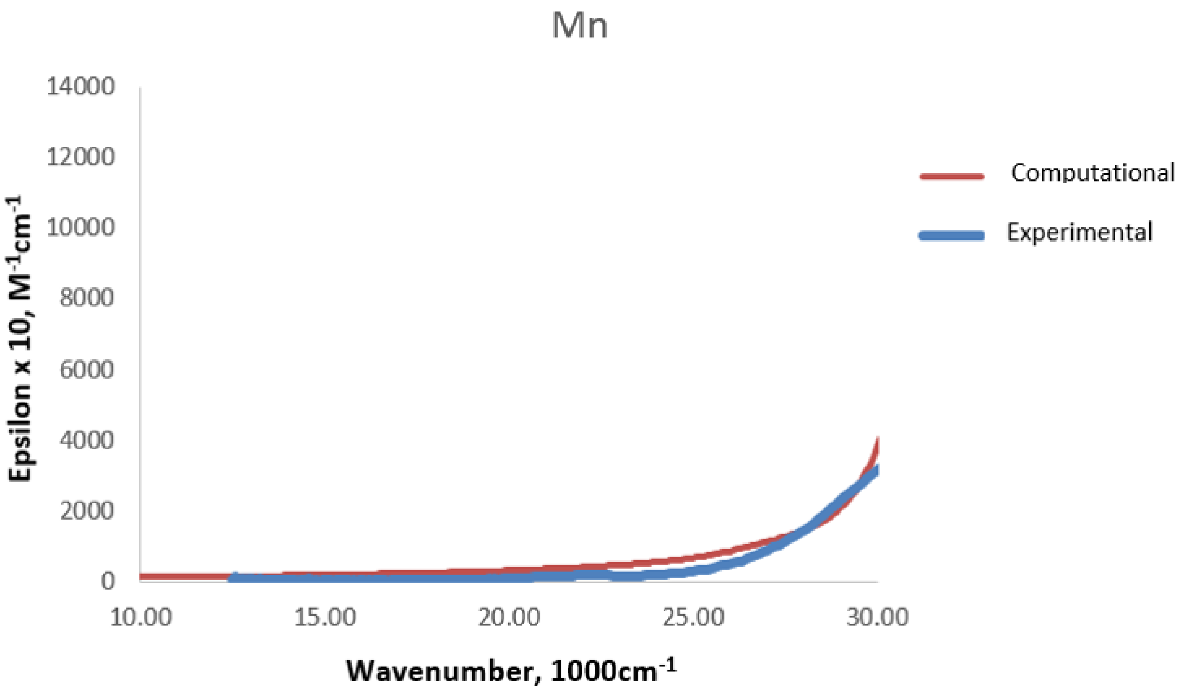

Figure 4.12: Comparison of computed and experimental electronic absorption data for monomeric structure of $MnBr_2$ with the SNS ligand.

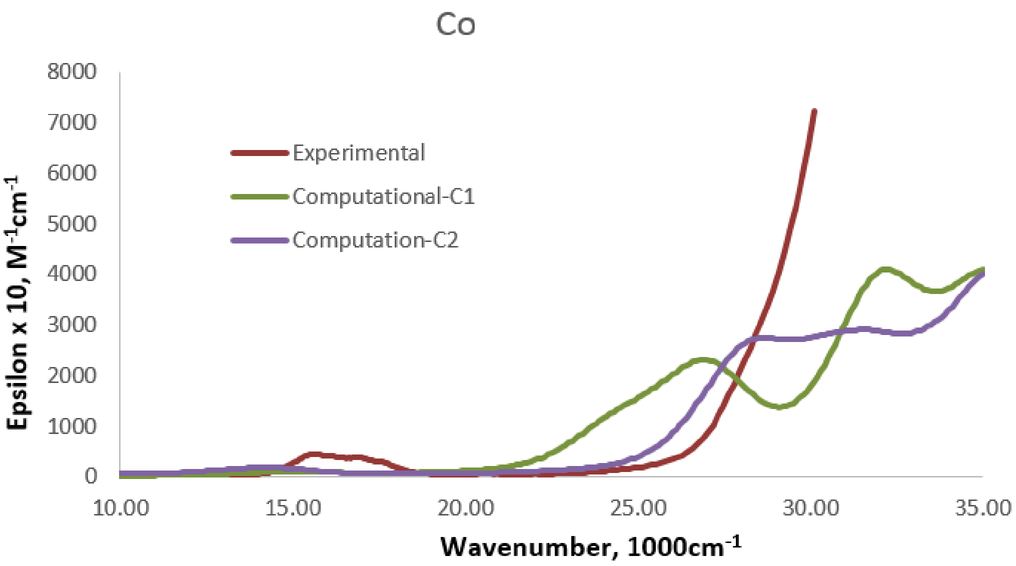

Figure 4.13: Comparison of computed and experimental electronic absorption data for monomeric structure of $CoBr_2$ with the SNS ligand.

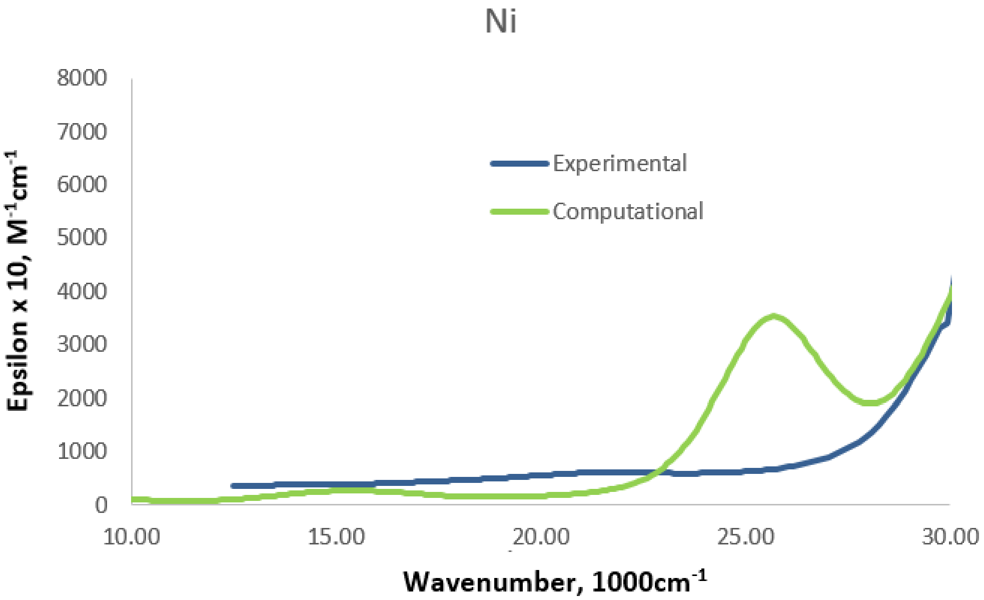

Figure 4.14: Comparison of computed and experimental electronic absorption data for monomeric structure of $NiBr_2$ with the SNS ligand.

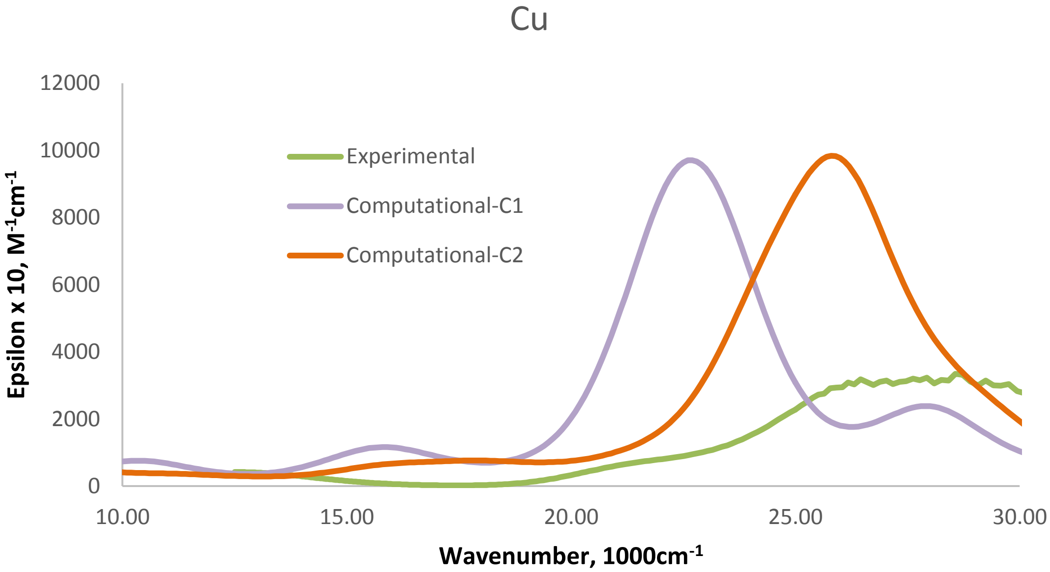

Figure 4.15: Comparison of computed and experimental electronic absorption data for monomeric structure of $CuBr_2$ with the SNS ligand.

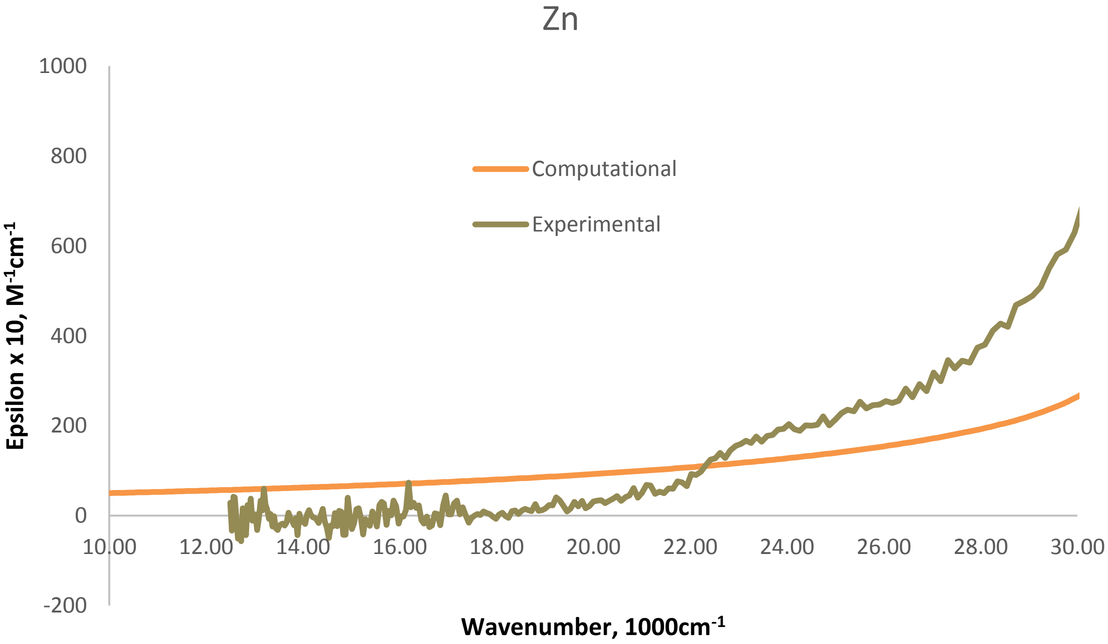

Figure 4.16: Comparison of computed and experimental electronic absorption data for monomeric structure of $ZnBr_2$ with the SNS ligand.

In reference to Figures 4.12 to 4.16, beginning with the $MnBr_2$-SNS electronic absorption spectra, the data correlates as there are no significant peaks in either the computed or the experimental figures. As mentioned earlier, no computed spectrum was elucidated for the $FeBr_2$-SNS complex as the structure experimentally determined was dimeric. In addition, the experimental data for the $CoBr_2$-SNS complex correlated with the computed data for both the C1 and C2 isomers. Conversely, the $NiBr_2$-SNS experimental data does not correlate with that computed. This is due to issues with solubility as it is known that it is difficult to obtain consistent data on solutions containing solid particles. In order to try to overcome this issue, several attempts at data collection were undertaken with a variety of solvents, but none of them proved to solubilise the complex entirely. The experimental electronic absorption data for the $CuBr_2$-SNS complex, on the other hand, correlated with the computed for both the C1 and C2 isomers. Lastly, the $ZnBr_2$-SNS data proved to correlate, although there are no significant peaks in either case as the metal centre is d^{10}.

Interestingly, it should also be noted that the electronic absorption spectra for the different conformers are quite similar. Consequently, it would be virtually impossible to differentiate between the two conformers using this method.

[4.3.2] Molecular orbital analysis

In order to further probe the bonding of the transition metal bromide-SNS coordination compounds, calculations were run in order to determine which transitions the peaks of the UV-Vis corresponded to. The Mn complex showed no transitions nor did the Zn complex and the Fe complex was a dimer; thus, only the Co and Cu complexes could be analyzed.

Firstly, computations were run for the different configurations (C1-C3) for the Co complex **4B**. For C1, the three major contributors, in order from lowest to highest, within the ligand orbitals are HOMO-9, HOMO-8 and HOMO-4 which are all predominantly ligand-based. HOMO-9 is largely S-based while HOMO-8 and HOMO-4 are largely Br-based. All three have small Co d-orbital contributions. The electrons within these MOs were found to principally donate into LUMO+4, which is largely metal-based with a small ligand contributions. Thus, these low energy bands appear to be dominated by ligand to metal charge transfer. A similar result is seen with the C2 configured complex in which HOMO-7 and HOMO-3 are the two major ligand-based donor orbitals while LUMO+3 is the major metal-based acceptor orbital. Lastly, for the C3 configured coordination complex, HOMO-5 and HOMO-3 are the major ligand-based donor orbitals while LUMO+3 is the major metal-based acceptor orbital. General molecular orbital figures for the two major HOMOs, one largely Br-based and one largely S-based, and the Co-based LUMO are shown in Figure 4.17.

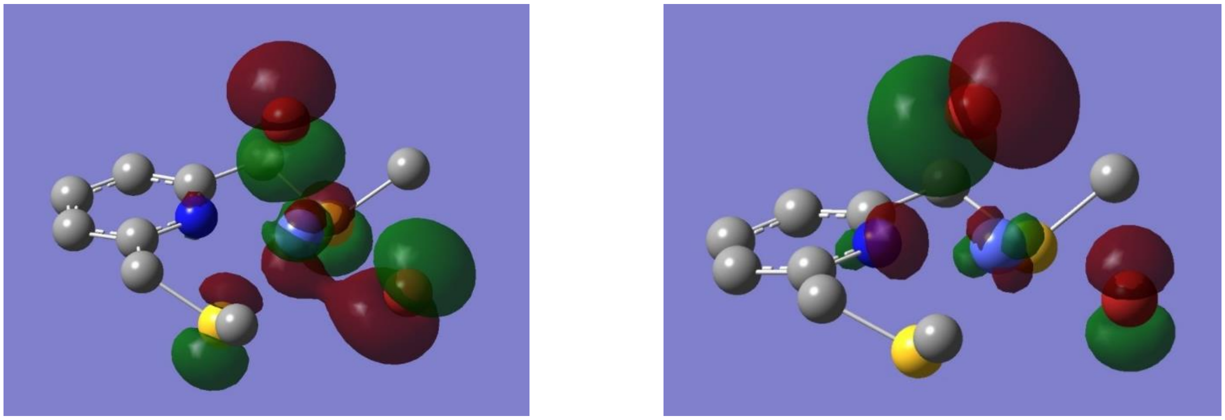

HOMO A **HOMO B**

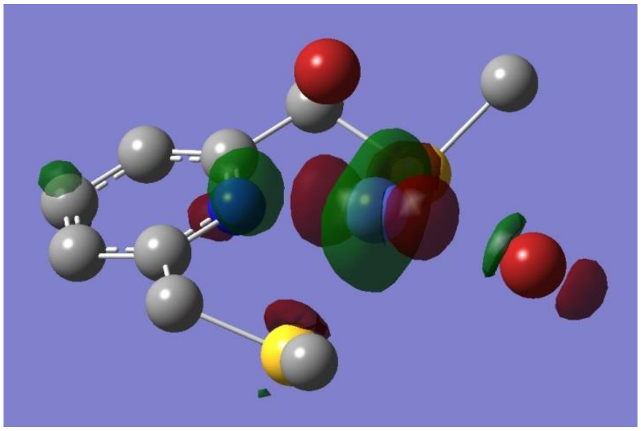

LUMO

Figure 4.17: General molecular orbital figures for HOMO A, HOMO B and LUMO for $CoBr_2$-SNS complex **4B**.

As can be seen, HOMO A is largely Br-based, while HOMO B is largely S-based. In addition, the LUMO is primarily Co d-orbital-based.

As a result, the $CoBr_2$-SNS complex can be described as a charge-transfer complex, more specifically, a ligand-to-metal charge transfer complex. Unlike covalent bonds, these are weaker electrostatic attractions in which a fraction of electronic charge is transferred from one molecular entity to another when the complex is excited by a photon; in this case, from largely ligand-based orbitals into mostly metal-based orbitals.

Secondly, computations were run for the different configurations (C1-C3) for the Cu complex **4C**. For C1, the major contributors, in order from lowest to highest, within the ligand orbitals are HOMO-5 and HOMO-1 which are all predominantly ligand-based. The electrons within these MOs were found to principally donate into LUMO+4, which is largely metal-based (51%) with ligand contributions. For the C2 conformation, the major contributors are HOMO-13, HOMO-6 and HOMO-2, all ligand-based, as well as LUMO which is 50% Cu d-orbital-based. Lastly, for the C3 conformers, the major orbital contributors are HOMO-6 and HOMO-3 which are mostly ligand based and LUMO which is 50% Cu d orbital-based.

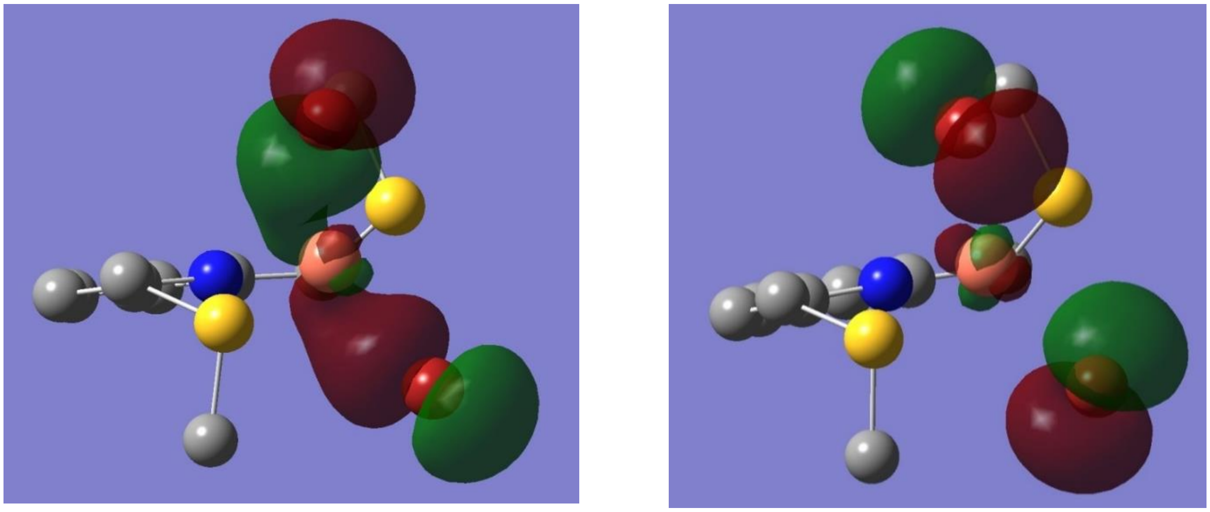

HOMO A **HOMO B**

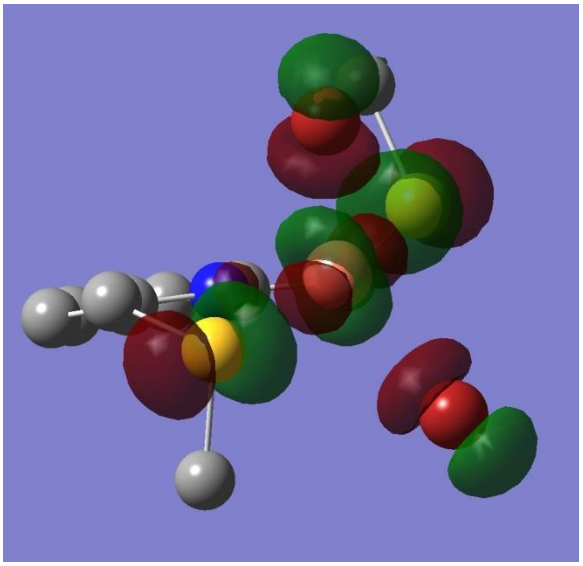

LUMO

Figure 4.17: General molecular orbital figures for HOMO A, HOMO B and LUMO for $CuBr_2$-SNS complex **5C**.

As can be seen in Figure 4.18, these MO figures differ from those seen in Figure 4.17. Here, the LUMO isn't purely d-orbital based, which correlates with higher covalence and shorter M-S and M-N bond lengths in this complex. Also, in HOMO A, one can see more of a metal contribution than in HOMO A for Figure 4.16.

[4.4] Conclusion

Overall, we were successful in reporting distinctive complexes of first row transition metal bromides supported by the SNS scaffold. The SNS scaffold readily reacted with the transition metal bromides to allow the preparation, isolation and analysis of a unique set of compounds. The resulting complexes were able to be fully characterized using ^{1}H and ^{13}C NMR, elemental analysis, mass spectrometry, UV-Vis absorption as well as IR absorption.

Furthermore, these coordination complexes were extensively analyzed in order to yield important information regarding bonding of these complexes. This includes their geometries, structural distortions, bond lengths and bond angles. From this data, important trends in coordination of these transition metal bromides to the SNS scaffold were able to be mapped; namely, trends in the metal-ligand bond lengths across the periodic row of transition metal bromides. Additionally, the magnetic moment of these complexes was calculated experimentally.

Lastly, computations were run in order to correlate the experimental bond lengths, bond angles and electronic absorption with the computed data. Fortunately, all of the experimental data correlated with the computational data within acceptable limits aside from the dimeric complex and the nickel complex which had issues with solubility. The computed data also correlated with bonding trends drawn from experimental data and expanded on reasoning as to why these trends are seen. Finally, molecular orbital assignments were completed on the $CoBr_2$ and $CuBr_2$-SNS complexes to allow for a more in-depth analysis of the bonding in these complexes. Specifically, it was determined that the $CoBr_2$-SNS complex is a charge transfer complex where electronic is transferred from a ligand-based orbital into a metal-based orbital while the $CuBr_2$-SNS complex had similar bonding but with higher covalency due to less d-orbital contribution in the LUMO and metal contribution in the HOMO.

[4.5] Experimental: Complexes of 1st row transition metal bromides with the SNS ligand

General Methods. Reactions were performed in a glovebox with a nitrogen atmosphere, with the exception of ligand synthesis, which was performed using standard Schlenk technique under a flow of N_2. All solvents were parged with nitrogen and then dried by passage through a column of activated alumina using an apparatus purchased from Anhydrous Engineering. Deuterated chloroform was dried using activated molecular sieves. Metal halides were purchased from Strem Chemicals and used as received. All other chemicals were purchased from Aldrich and used without further purification. Compound **SNS** and **SNS2** were synthesized according to literature procedure. NMR spectra were acquired on a Bruker Avance 300 MHz spectrometer with CD_2Cl_2, and $CDCl_3$ as solvents and internal standards. Elemental analyses for **4A-4F** were performed by Midwest Microlab LLC, Indianapolis IN. Mass spectrometry (MS) was completed by the Holmes group at the University of Ottawa using TOF MS ES on a Micromass-Q TOF II. Values are reported in g/mol and are ranked in order of decreasing intensity. The rank is provided in brackets.

(4a) MnBr$_2$- 2,6-bis(methylthiomethyl) pyridine: $MnBr_2$ powder (32 mg, 0.149 mmol) was added to a clear yellow solution of **SNS** (44.6 mg, 0.224 mmol) in 8 mL of toluene. The reaction mixture was allowed to stir for 14 hours, gradually becoming opaque white. Solution was then held at -20°C overnight, over which time a pale white precipitate formed. The solid was isolated by filtration, washed with 5 x 2 mL hexanes, and allowed to dry under vacuum. A white powder was isolated in 95% yield. White crystals were too small for X-ray analysis.Elemental analysis calculated (%) for [$C_9H_{13}Br_2MnNS_2$]: C 26.10, H 3.17, N 3.38, found C 26.08, H 3.12, N 3.34. ^{1}H NMR ($CDCl_3$, 300MHz): δ 7.65 (br t,1H) 7.30 (br d, 2H), 3.77 (br s, 4H, CH_2-py), 2.05 (br s, 6H, CH_3). ^{13}C NMR ($CDCl_3$, 75 MHz). δ 145 (Ar-C), 130(Ar-CH), 132(Ar-CH), 41(Ar-CH_2-S), 14(S-CH_3). MS: 417.82(7), 416.82(5), 415.82(2), 414.82(4), 413.82(1), 412.82(6), 411.82(3).

(4A) $FeBr_2$- 2,6-bis(methylthiomethyl)pyridine: $FeBr_2$ powder (30 mg, 0.139 mmol) was added to a clear yellow solution of **SNS** (41.5 mg, 0.209 mmol) in 8 mL of toluene. The reaction mixture was allowed to stir for 14 hours, gradually becoming opaque orange/ochre. Solution was then held at -20°C overnight, over which time an intense brown precipitate formed. The solid was isolated by filtration, washed with 5 x 2 mL hexanes, and allowed to dry under vacuum. A fine peach coloured powder was isolated in 96% yield. Peach crystals suitable for X-ray analysis were grown by diffusion of saturated THF solution in hexanes, and storing at -20°C for several days. Elemental analysis calculated (%) for [$C_9H_{13}Br_2FeNS_2$]: C 26.04, H 3.16, N 3.38, found C 25.93, H 3.11, N 3.08. ^{1}H NMR ($CDCl_3$, 300MHz): δ 7.73 (t,1H) 7.32 (d, 2H), 3.72 (s, 4H, CH_2-py), 2.05 (s, 6H, CH_3). ^{13}C NMR ($CDCl_3$, 75 MHz). δ 152 (Ar-C), 136(Ar-CH), 128(Ar-CH), 38(Ar-CH_2-S), 14(S-CH_3). MS: 418.81(7), 417.82(5), 416.82(2), 415.82(4), 414.82(1), 413.83(6), 412.82(3),

(4B) $CoBr_2$- 2,6-bis(methylthiomethyl)pyridine: $CoBr_2$ powder (30 mg, 0.137 mmol) was added to a clear yellow solution of **SNS** (41 mg, 0.206 mmol) in 8 mL of toluene. The reaction mixture was allowed to stir for 14 hours, gradually becoming opaque blue. Solution was then held at -20°C overnight, over which time an opaque ochre precipitate formed. The solid was isolated by filtration, washed with 5 x 2 mL hexanes, and allowed to dry under vacuum. A dark ochre powder was isolated in 97% yield. Large yellow crystals suitable for X-ray analysis were grown by diffusion of saturated CH_2Cl_2 solution in hexanes, and storing at -20°C for several days. Elemental analysis calculated (%) for [$C_9H_{13}Br_2CoNS_2$]: C 25.85, H 3.14, N 3.35, found C 25.74, H 3.11, N 3.37. ^{1}H NMR ($CDCl_3$, 300MHz): δ 7.68 (br t,1H) 7.38 (br d, 2H), 3.0 (br s, 4H, CH_2-py), 2.5 (br s, 6H, CH_3). ^{13}C NMR ($CDCl_3$, 75 MHz). δ 152 (Ar-C), 133(Ar-CH), 129(Ar-CH), 40(Ar-CH_2-S), 15(S-CH_3). MS: 421.81(7). 420.82(5). 419.81(2), 418.82(4), 417.82(1), 416.82(6), 415.82(3).

(4b) $NiBr_2$- 2,6-bis(methylthiomethyl)pyridine: $NiBr_2$ powder (30 mg, 0.137 mmol) was added to a clear yellow solution of **SNS** (41 mg, 0.206 mmol) in 8 mL of toluene. The reaction mixture was allowed to stir for 14 hour, gradually becoming opaque ochre. The solution gradually turned bright yellow. Solution was then held at -20°C overnight, over which time a yellow/green precipitate formed. Solution was filtered, washed with 5 x 2 mL hexanes, and allowed to dry under vacuum. Due to poor solubility of $NiBr_2$ starting material, obtaining high yield and high purity presents difficulties; purity is enhanced at the cost of yield by a series of recrystallizations in CH_2Cl_2. A bright green powder was ultimately isolated in 64% yield. Due to small size of crystals and lack of solubility, crystals suitable for X-ray analysis were not able to be grown. Elemental analysis calculated (%) for [$C_9H_{13}Br_2NiNS_2$]: C 25.87, H 3.14, N 3.35, found C 25.89, H 3.17, N 3.38. ^{1}H NMR ($CDCl_3$, 300MHz): δ 7.69 (t,1H) 7.25 (d, 2H), 3.78 (s, 4H, CH_2-py), 2.06 (s, 6H, CH_3). ^{13}C NMR ($CDCl_3$, 75 MHz). δ 148 (Ar-C), 137(Ar-CH), 127(Ar-CH), 42(Ar-CH_2-S), 13(S-CH_3). MS: 422.81(8), 420.81(4), 419.82(6), 418.81(2), 417.82(5), 416.82(1), 415.82(7), 414.82(3).

(4C) $CuBr_2$ – 2,6-bis(methylthiomethyl)pyridine: $CuBr_2$ powder (32 mg, 0.143 mmol) was added to a clear yellow solution of **SNS** (43 mg, 0.215 mmol) in 8 mL of toluene. The reaction mixture was allowed to stir for 14 hours, gradually becoming a green hue. Solution was then held at -20°C overnight, over which time a forest green coloured precipitate formed. Solution was filtered, washed with 5 x 2 mL hexanes, and allowed to dry under vacuum. A bright green powder was isolated in 84% yield. Crystals suitable for X-ray analysis were grown by diffusion of saturated MeCN solution in hexanes, and storing at -20^{o}C for several days. Elemental analysis calculated (%) for [$C_9H_{13}Br_2CuNS_2$]: C 25.57, H 3.10, N 3.32, found C 25.64, H 3.09, N 3.22. ^{1}H NMR ($CDCl_3$, 300MHz): δ 7.51 (br t,1H) 6.96 (br d, 2H), 3.49 (br s, 4H, CH_2-py), 2.02 (br s, 6H, CH_3). ^{13}C NMR ($CDCl_3$, 75 MHz). δ 148 (Ar-C), 136(Ar-CH), 124(Ar-CH), 42(Ar-CH_2-S), 15(S-CH_3). MS: 425.81(4), 424.82(6), 423.81(2), 422.82(5), 421.82(1), 420.82(7), 419.82(3).

(4D) ***$ZnBr_2$* – *2,6-bis(methylthiomethyl)pyridine*:** $ZnBr_2$ powder (32 mg, 0.142 mmol) was added to a clear yellow solution of **SNS** (42 mg, 0.213 mmol) in 8 mL of toluene. The reaction mixture was allowed to stir for 14 hours, gradually becoming opaque white. Solution was then held at -20^{o}C overnight, over which time a white precipitate formed. Solution was filtered, washed with 5 x 2 mL hexanes, and allowed to dry under vacuum. A pale stark white powder was isolated in 93% yield. white crystals suitable for X-ray analysis were grown by diffusion of saturated CH_2Cl_2 solution in hexanes, and storing at -20^{o}C for severaldays. Elemental analysis calculated (%) for [$C_9H_{13}Br_2ZnNS_2$]: C 25.46, H 3.09, N 3.30, found C 25.50, H 3.12, N 3.24. ^{1}H NMR ($CDCl_3$, 300MHz): δ 7.75 (t,1H) 7.32 (d, 2H), 3.79 (s, 4H, CH_2-py), 2.08 (s, 6H, CH_3). ^{13}C NMR ($CDCl_3$, 75 MHz). δ 150 (Ar-C), 128(Ar-CH), 124(Ar-CH), 42(Ar-CH_2-S), 15(S-CH_3). MS: 428.81(5), 427.81(8), 426.81(3), 425.81(6), 424.81(1), 423.81(7). 422.81(2), 421.81(9), 420.81(4).

(4E) ***$CoBr_2$*- *2,6-bis(ethylthiomethyl)pyridine***: $CoBr_2$ powder (30 mg, 0.137 mmol) was added to a clear yellow solution of **SNS2** (47 mg, 0.206 mmol) in 8 mL of toluene. The reaction mixture was allowed to stir for 14 hours, gradually becoming opaque blue. Solution was then held at -

20^oC overnight, over which time a dark blue precipitate formed. The solid was isolated by filtration, washed with 5 x 2 mL hexanes, and allowed to dry under vacuum. A bright blue powder was isolated in 97% yield. Large blue crystals suitable for X-ray analysis were grown by diffusion of saturated CH_2Cl_2 solution in hexanes, and storing at -20^oC for several days. Elemental analysis calculated (%) for $[C_{11}H_{17}Br_2CoNS_2]$: C 29.62, H 3.84, N 3.14, found C 29.71, H 3.87, N 3.17. ^1H NMR ($CDCl_3$, 300MHz): δ 7.43 (br t, 1H) 7.00 (br dd, 2H), 2.9 (br s, 4H, CH_2-py), 2.70 (br q, 4H, S-CH_2), 1.26 (br t, 6H, CH_3) . ^{13}C NMR ($CDCl_3$, 75 MHz). δ 149 (Ar-C), 129(Ar-CH), 120(Ar-CH), 42(Ar-CH_2-S), 26(S-CH_2), 14(S-CH_3). MS: 449.84(7), 448.85(5), 447.84(2), 446.85(4), 445.85(1), 444.85(6), 443.85(3).

(4F) ***$CuBr_2$ – 2,6-bis(ethylthiomethyl)pyridine***: $CuBr_2$ powder (32 mg, 0.143 mmol) was added to a clear yellow solution of **SNS2** (49 mg, 0.215 mmol) in 8 mL of toluene. The reaction mixture was allowed to stir for 14 hours, gradually becoming a green hue. Solution was then held at -20^oC overnight, over which time a bright green coloured precipitate formed. Solution was filtered, washed with 5 x 2 mL hexanes, and allowed to dry under vacuum. A bright green powder was isolated in 84% yield. Crystals suitable for X-ray analysis were grown by diffusion of saturated CH_2Cl_2 solution in hexanes, and storing at -20^oC for several days. Elemental analysis calculated (%) for $[C_{11}H_{17}Br_2CuNS_2]$: C 29.31, H 3.80, N 3.11, found C 29.35, H 3.82, N 3.15. ^1H NMR ($CDCl_3$, 300MHz): δ 7.53 (t, 1H) 6.92 (dd, 2H), 3.5 (s, 4H, CH_2-py), 2.2 (q, 4H, S-CH_2), 0.86 (t, 6H, CH_3) . ^{13}C NMR ($CDCl_3$, 75 MHz). δ 148 (Ar-C), 130(Ar-CH), 122(Ar-CH), 40(Ar-CH_2-S), 25(S-CH_2), 14(S-CH_3). MS: 454.85(8), 453.84(4), 452.85(6), 451.84(2), 450.85(5), 449.85(1), 448.85(7), 447.85(3)

Infrared spectra were collected from powder samples on a Cary 630 FT- IR. All experiments were conducted under laboratory atmosphere. Values are reported in cm^{-1} and are ranked in order of decreasing intensity. The rank in terms of relative intensity is provided in brackets (1 being the most intense).

4a: 3027(11), 3024(8), 3011(6), 2925(4), 1608(3), 1599(1), 1483(9), 1203(13), 1108(12), 1036(5), 1024(7), 960(14), 880(2), 643(10)

4b: 3109(6), 3022(5), 2954(8), 1743(2), 1622(1), 1517(7), 1443(9), 1214(3), 1116(10), 1098(12), 1035(4), 923(13), 687(11)

4A: 3122(5), 3012(3), 2987(10), 1673(4), 1621(1), 1543(6), 1445(12), 1358(2), 1245(11), 1154(7), 986(8), 644(9)

4B: 3201(7), 3014(2), 2965(8), 2875(3), 1634(10), 1588(1), 1421(6), 1358(5), 1154(12), 1128(4), 954(9), 732(11)

4C: 3102(4), 2987(2), 2895(7), 1643(9), 1601(1), 1588(3), 1526(10), 1498(6), 1301(5), 1140(11), 732(8), 685(12)

4D: 3115(7), 3012(3), 2987(9), 1643(4), 1621(2), 1576(10), 1534(5), 1487(1), 1458(13), 1209(6), 1154(12), 948(8), 745(11)

4E: 3045(4), 3014(10), 2784(5), 1689(13), 1645(6), 1590(9), 1543(2), 1504(8), 1497(1), 1445(3), 1287(7), 978(12), 845(11), 734(14)

4F: 3204(8), 3108(2), 2990(7), 2867(3), 1713(11), 1609(14), 1576(1), 1564(4), 1528(6), 1509(5), 1445(16), 1402(10), 1327(13), 1289(9), 998(12), 674(15)

[4.6] X-ray crystallographic information

Table 4.8: Summary of data collection and crystallographic parameters for **4A-F**.

Compound	**4A**	**4B**	**4C**	**4D**
Empirical formula	$C_9H_{13}Br_2FeNS_2$	$C_{18}H_{26}Br_4Co_2N_2S_4$	$C_9H_{13}Br_2CuNS_2$	$C_9H_{13}Br_2CZnNS_2$
Formula weight	414.99	869.73	422.68	849.03
Temperature (K)	200(2)	200(2)	200(2)	200(2)
λ(Å)	0.71073	0.71073	0.71073	0.71073
Crystal system	Triclinic	Triclinic	Monoclinic	monoclinic
Space group	P-1	P-1	P2(1)/c	C2/c
a (Å)	7.7977(2)	10.3494(4)	12.5690(2)	22.6533(7)
b (Å)	8.4575(3)	10.8403(4)	7.3812(2)	8.4765(2)
c (Å)	11.2743(4)	13.4415(5)	14.9067(3)	15.3060(4)
α (deg)	98.693(2)	70.202(2)	90.00	90.00
β (deg)	102.694(2)	77.559(2)	104.2270(10)	101.693(2)
γ (deg)	110.110(2)	85.166(2)	90.00	90.00
V ($Å^3$)	659.95(4)	1385.45(9)	1340.54(5)	2878.08
Z	2	2	4	4
ρ (calc) (Mg/m^3)	2.088	2.004	2.094	1.959
μ (mm^{-1})	7.481	7.277	7.870	7.520
Absorption correction	Semi-empirical from equivalents			
R1[a]	0.0247	0.0266	0.0323	0.0355
*w*R2[b]	0.0568	0.0653	0.0742	0.0801

[a] $R1 = \Sigma \left\| F_o \right| - \left| F_c \right\| / \Sigma \left| F_o \right|$. [b] $wR2 = \left(\Sigma\, w\left(\left| F_o \right| - \left| F_c \right| \right)^2 / \Sigma\, w \left| F_o \right|^2 \right)^{1/2}$

Table 4.8 continued

Compound	**4E**	**4F**
Empirical formula	$C_{11}H_{17}Br_2CoNS_2$	$C_{11}H_{17}Br_2CuNS_2$
Formula weight	445.12	450.74
Temperature (K)	200(2)	200(2)
λ (Å)	0.71073	0.71073
Crystal system	Monoclinic	Monoclinic
Space group	P2(1)/c	P2(1)/c
a (Å)	13.9730(9)	13.920(2)
b (Å)	7.7058(2)	7.6615(12)
c (Å)	15.9546(3)	15.808(2)
α (deg)	90.00	90.00
β (deg)	112.7630	112.632
γ (deg)	90.00	90.00
V (Å^3)	1584.08(6)	1556.07
Z	4	4
ρ (calc) (Mg/m^3)	1.866	1.924
μ (mm^{-1})	6.371	6.786
Absorption correction	Semi-empirical from equivalents	
R1[a]	0.0239	0.0484
*w*R2[b]	0.0606	0.1190

[a] $R1 = \Sigma \left\| F_o \right| - \left| F_c \right\| / \Sigma \left| F_o \right|$. [b] $wR2 = \left(\Sigma\, w \left(\left| F_o \right| - \left| F_c \right| \right)^2 / \Sigma\, w \left| F_o \right|^2 \right)^{1/2}$

Table 4.9: Selected bond lengths (A) for compounds **4A-4F.**

4A		**4B**		**4C**	
C(1)-C(6)	1.508(3)	C(1)-C(6)	1.500(3)	C(1)-C(6)	1.505(4)
C(5)-C(8)	1.501(4)	C(5)-C(8)	1.512(3)	C(5)-C(7)	1.500(4)
C(1)-N(1)	1.336(3)	C(1)-N(1)	1.352(3)	C(1)-N(1)	1.354(3)
C(5)-N(1)	1.353(3)	C(5)-N(1)	1.345(3)	C(5)-N(1)	1.352(4)
C(6)-S(1)	1.806(3)	C(6)-S(1)	1.806(3)	C(6)-S(1)	1.794(3)
C(8)-S(2)	1.803(3)	C(8)-S(2)	1.801(2)	C(7)-S(2)	1.802(3)
Fe(1)-N(1)	2.1811(19)	Co(1)-N(1)	2.065(2)	Cu(1)-N(1)	2.014(2)
Fe(1)-S(1)	2.5196(7)	Co(1)-S(1)	2.5028(6)	Cu(1)-S(1)	2.3380(9)
Fe(1)-S(2)	2.5691(7)	Co(1)-S(2)	2.4945(6)	Cu(1)-S(2)	2.3297(8)
Fe(1)-Br(1)	2.5669(4)	Co(1)-Br(1)	2.3987(4)	Cu(1)-Br(1)	2.3832(5)
Fe(1)-Br(2)	2.5720(4)	Co(1)-Br(2)	2.4100(4)	Cu(1)-Br(2)	2.6741(5)
Fe(1)-Br(1)[a]	2.7104(4)	--	--	--	--

Table 4.9 continued

4D		**4E**		**4F**	
C(1)-C(6)	1.503(5)	C(1)-C(6)	1.499(3)	C(1)-C(6)	1.518(15)
C(5)-C(7)	1.485(5)	C(5)-C(9)	1.503(3)	C(5)-C(9)	1.506(16)
C(1)-N(1)	1.339(4)	C(1)-N(1)	1.352(2)	C(1)-N(1)	1.329(13)
C(5)-N(1)	1.347(4)	C(5)-N(1)	1.345(3)	C(5)-N(1)	1.345(13)
C(6)-S(1)	1.794(4)	C(6)-S(1)	1.799(3)	C(6)-S(1)	1.789(10)
C(7)-S(2)	1.795(5)	C(9)-S(2)	1.792(2)	C(9)-S(2)	1.777(11)
Zn(1)-N(1)	2.092(3)	Co(1)-N(1)	2.1172(16)	Cu(1)-N(1)	2.016(9)
Zn(1)-S(1)	2.751(1)	Co(1)-S(1)	2.4502(6)	Cu(1)-S(1)	2.321(3)
Zn(1)-Br(1)	2.3689(6)	Co(1)-Br(1)	2.4212(4)	Cu(1)-Br(1)	2.5467(18)
Zn(1)-Br(2)	2.3635(7)	Co(1)-Br(2)	2.4349(4)	Cu(1)-Br(2)	2.4053(17)
--	--	--	--	--	--

Table 4.10: Selected bond angles for compounds **4A-4F.**

4A		**4B**		**4C**	
C(1)-N(1)-C(5)	118.9(2)	C(1)-N(1)-C(5)	118.7(2)	C(1)-N(1)-C(5)	118.8(2)
C(1)-C(6)-S(1)	115.69(18)	C(1)-C(6)-S(1)	113.24(16)	C(1)-C(6)-S(1)	114.4(2)
C(1)-N(1)-Fe(1)	119.53(15)	C(1)-N(1)-Co(1)	120.66(16)	C(1)-N(1)-Cu(1)	121.3(2)
C(5)-C(8)-S(2)	113.91(17)	C(5)-C(8)-S(2)	114.12(16)	C(5)-C(7)-S(2)	113.9(2)
C(5)-N(1)-Fe(1)	119.60(16)	C(5)-N(1)-Co(1)	120.46(14)	C(5)-N(1)-Cu(1)	119.51(18)

C(6)-C(1)-N(1)	119.3(2)	C(6)-C(1)-N(1)	117.2(2)	C(6)-C(1)-N(1)	116.4(3)
C(8)-C(5)-N(1)	117.3(2)	C(8)-C(5)-N(1)	117.5(2)	C(7)-C(5)-N(1)	117.3(2)
N(1)-Fe(1)-S(1)	79.11(5)	N(1)-Co(1)-S(1)	81.73(5)	N(1)-Cu(1)-S(1)	85.09(7)
N(1)-Fe(1)-S(2)	80.36(5)	N(1)-Co(1)-S(2)	81.56(5)	N(1)-Cu(1)-S(2)	84.42(7)
N(1)-Fe(1)-Br(1)	176.64(5)	N(1)-Co(1)-Br(1)	133.28(5)	N(1)-Cu(1)-Br(1)	159.74(7)
N(1)-Fe(1)-Br(2)	91.55(5)	N(1)-Co(1)-Br(2)	108.89(5)	N(1)-Cu(1)-Br(2)	94.07(6)
N(1)-Fe(1)-Br(1)[a]	90.87(5)	--	--	--	--
S(1)-Fe(1)-Br(1)	103.350(19)	S(1)-Co(1)-Br(1)	95.027(19)	S(1)-Cu(1)-Br(1)	92.87(3)
S(1)-Fe(1)-Br(1)[a]	91.852(19)	--	--	--	--
S(1)-Fe(1)-Br(2)	87.329(19)	S(1)-Co(1)-Br(2)	96.521(19)	S(1)-Cu(1)-Br(2)	103.85(3)
S(2)-Fe(1)-Br(1)	96.88(2)	S(2)-Co(1)-Br(1)	95.448(18)	S(2)-Cu(1)-Br(1)	93.42(2)
S(2)-Fe(1)-Br(1)[a]	81.070(19)	--	--	--	--
S(2)-Fe(1)-Br(2)	100.62(2)	S(2)-Co(1)-Br(2)	90.114(18)	S(2)-Cu(1)-Br(2)	87.10(2)
Br(1)-Fe(1)-Br(2)	90.849(13)				

Table 4.10 continued

4D		**4E**		**4F**	
C(1)-N(1)-C(5)	119.5(3)	C(1)-N(1)-C(5)	118.74(17)	C(1)-N(1)-C(5)	119.3(9)
C(1)-C(6)-S(1)	112.7(3)	C(1)-C(6)-S(1)	115.03(15)	C(1)-C(6)-S(1)	113.0(8)
C(1)-N(1)-Zn(1)	121.6(2)	C(1)-N(1)-Co(1)	120.75(14)	C(1)-N(1)-Cu(1)	120.7(7)
C(5)-C(7)-S(2)	113.9(3)	C(5)-C(9)-S(2)	114.67(16)	C(5)-C(9)-S(2)	114.9(8)
C(5)-N(1)-Zn(1)	119.0(2)	C(5)-N(1)-Co(1)	120.43(12)	C(5)-N(1)-Cu(1)	119.9(8)
C(6)-C(1)-N(1)	117.7(3)	C(6)-C(1)-N(1)	118.28(19)	C(6)-C(1)-N(1)	117.3(9)
C(7)-C(5)-N(1)	118.3(3)	C(4)-C(5)-N(1)	122.03(19)	C(4)-C(5)-N(1)	121.8(10)
N(1)-Zn(1)-S(1)	77.08(7)	N(1)-Co(1)-S(1)	82.17(5)	N(1)-Cu(1)-S(1)	85.0(3)
N(1)-Zn(1)-S(2)	80.22(8)	N(1)-Co(1)-S(2)	81.96(5)	N(1)-Cu(1)-S(2)	85.5(3)
N(1)-Zn(1)-Br(1)	122.58(7)	N(1)-Co(1)-Br(1)	98.38(5)	N(1)-Cu(1)-Br(1)	96.6(3)
N(1)-Zn(1)-Br(2)	116.22(7)	N(1)-Co(1)-Br(2)	149.05(5)	N(1)-Cu(1)-Br(2)	157.1(3)
S(1)-Zn(1)-Br(1)	95.53(3)	S(1)-Co(1)-Br(1)	101.167(2)	S(1)-Cu(1)-Br(1)	102.10(9)
S(1)-Zn(1)-Br(2)	89.47(3)	S(1)-Co(1)-Br(2)	91.771(18)	S(1)-Cu(1)-Br(2)	90.59(8)
S(2)-Zn(1)-Br(1)	96.34(3)	S(2)-Co(1)-Br(1)	101.446(2)	S(2)-Cu(1)-Br(1)	96.80(9)
S(2)-Zn(1)-Br(2)	100.95(3)	S(2)-Co(1)-Br(2)	91.316(17)	S(2)-Cu(1)-Br(2)	91.13(9)
Br(1)-Zn(1)-Br(2)	120.60(2)	Br(1)-Co(1)-Br(2)	112.570(1)	Br(1)-Cu(1)-Br(2)	106.30(6)

Chapter 5: Conclusion

This project expanded on previous work done by the Richeson group with the DIMPY ligand scaffold. Its use has been propagated due to its ease of synthesis, facile tuning of sterics on the N-aryl side arms, and known utility as a pincer-type ligand. Though it has been employed in the past, its chemistry with first row transition metals has not been extensively probed. Our goal was to obtain a greater understanding of the coordination of this ligand with first row transition metal bromides in order to, ultimately, be able to predict the electronic and structural properties of future complexes employing similar ligand scaffolds and first row transition metals.

We were successful in the synthesis of novel complexes of first row transition metal bromide-DIMPY complexes and able to obtain increased understanding of the electronic properties of these complexes by looking at the bonding both experimentally and computationally. Through this analysis, we were able to elucidate some trends in bond length and covalency across the first row of transition metals

Furthermore, in order to branch off from the DIMPY scaffold, we chose to employ a different but similar pincer-type ligand – the 2,6-bis(methylthiomethyl) pyridine, SNS1, and 2,6-bis(ethylthiomethyl) pyridine, SNS2, ligands as the former had been employed in previous work by the Richeson group and showed interesting magnetic behavior in terms of single molecule magnetic behavior. Their use is also facilitated by their ease of synthesis as well as their facile tuning by varying the sulfur side arms. In addition, the coordination chemistry of these S,N,S-type ligand scaffolds had not been extensively probed with transition metal bromides.

Again, we were successful in synthesizing novel complexes of first row transition metal bromides with the SNS1 and SNS2 ligands. Through experimental and computational analysis of the electronic properties, we were able to elucidate analogous metal-ligand bond length and covalency trends to those with the DIMPY scaffold. In addition, we were able to corroborate the experimental data with computational models.

Overall, the ligand-metal covalent interaction for the majority of these complexes was found to be quite weak. Consistent trends in the metal-ligand bond lengths of these types of complexes were able to be established and explained through computational analysis. Further computations remain to be done for the DIMPY complexes as the molecular orbital assignment has yet to be completed; however, computations completed on the $CoBr_2$-SNS and $CuBr_2$-SNS complexes indicate that these are more like charge transfer complexes with unsymmetrical sharing of electrons between the ligand and the metal center. Furthermore, increased covalency was shown in the $CuBr_2$-SNS complex as shown in the MO figures.

In summary, we were ultimately successful in our goal of investigating whether the N,N’,N and S,N,S ligand scaffolds could support novel electronic and/or magnetic properties with first-row transition metals; specifically transition metal bromides. We were also able to show that the different ligand scaffolds dictate the geometry of these 5 coordinate complexes. Fine tuning remains to be done to prevent dimerization in the case of the S,N,S ligands. In addition, we were able to elucidate some trends in metal-ligand bonding, analyze the magnetic and electronic properties of these complexes and take a closer look at the ligand-metal interactions. We were also successful in correlating the majority of these properties with computational models.

In conclusion, we were able to synthesize and characterize a wide array of novel compounds. I believe that this work has contributed to broadening the understanding of bonding interactions between first row transition metals and these two kinds of ligand scaffolds and that through a better understanding of the bonding interactions, one can fine tune these types of complexes so that they adopt properties necessary or advantageous for their desired use.